POLITECNICO DI TORINO

Corso di Laurea Magistrale in Ingegneria Energetica
e Nucleare

Tesi di Laurea Magistrale

"Computational methods for Loss-Of-Flow Accident (LOFA) Precursors identification in a simplified Superconducting Magnet Cryogenic Cooling Circuit for Nuclear Fusion Application"

Relatori

Prof. Pedroni Nicola

Prof. Di Maio Francesco

Correlatori

Dr. Bonifetto Roberto

Prof.ssa Savoldi Laura

Prof. Zanino Roberto

Prof. Zio Enrico

Candidato

Destino Vincenzo

a.a. 2018/2019

Ringraziamenti

Contents

Abstract

In nuclear fusion systems, such as the International Thermonuclear Experimental Reactor (ITER), plasma is magnetically confined with Superconductive Magnets (SMs), which must be kept at cryogenic temperature in order to preserve their superconductive properties by a Superconducting Magnet Cryogenic Cooling Circuit (SMCCC). Loss-Of-Flow Accidents (LOFA) in the SMCCC must be avoided, because they endanger the cooling ability of the SMCCC.

In this work, an approach to identify LOFA precursors (i.e., those component failures which lead to a LOFA) is developed, based on On-line Supervised Spectral Clustering (OSSC) with a Fuzzy C-Means (FCM) algorithm. The approach is applied to a simplified model of a cryogenic cooling circuit of a single module of the ITER Central Solenoid (CS), whose behaviour in normal and abnormal conditions is simulated by the validated deterministic 4C code. Results show that the approach elaborated timely identifies several LOFA precursors and components failed. In some cases, LOFA precursors are identified in scenarios with no LOFA, as well as components that have not actually failed. On one side, this conservatively increases the safety of the SMCCC (by overestimating the number of failed components to be inspected); on the other side, it might reduce its availability (due, e.g., to unnecessary inspection procedures).

For reducing the overestimation, the quality of the "maps" used for training the LOFA precursors identification approach is improved by training an adaptive meta-model to mimic the behaviour of the detailed, long-running 4C code, and using it to generate a large number of simulation runs for a deep exploration of the possible abnormal conditions of the system to be used for learning rules of precursors identification.

KEYWORDS: Nuclear Fusion, Superconducting Magnets, ITER Central Solenoid, Cryogenic Cooling Circuit, Loss-Of-Flow Accident (LOFA), Precursors identification, Spectral Clustering, Fuzzy C-Means, Meta-model, Adaptive Simulation.

List of Figures

V

List of Tables

List of Acronyms

AK-MCS	Adaptive Kriging - Monte Carlo Sampling
B	Burning
BV	By-pass Valve
C1	Control system 1
C2	Control system 2
CC	Correction Coil
CICC	Cable-In-Conduit Conductor
CP	Centrifugal Pump
CS	Central Solenoid
CSM	Central Solenoid Module
CV	Control Valve
D	Dwell
DOE	Design Of Experiment
FCM	Fuzzy C-Means
FM	First Magnetization
HX	Heat exchanger
IIS	Intermediate Inter-coil Structure
ITER	International Thermonuclear Experimental Reactor
LHe	Liquid Helium
LOFA	Loss-Of-Flow Accident
M	Last Magnetization
MC	Monte Carlo
MCS	Monte Carlo Sampling
MVL	Multiple Valued Logic
NC	Normally Closed
NO	Normally Open
OIS	Outer Inter-coil Structure
OSSC	On-line Supervised Spectral Clustering
PCR	Pre-Compression Rings
PF	Poloidal Field
POD	Proper Orthogonal Decomposition
QL	Quench Line
QT	Quench Tank
R	Rump Down
SC	Spectral Clustering
SHe	Supercritical Helium
SM	Superconductive Magnet
SMCCC	Superconducting Magnet Cryogenic Cooling Circuit
SV	Safety Valve
SVD	Single Value Decomposition
TF	Toroidal Field

List of Symbols

G_0	Nominal flow in the CSM
I/I_{cr}	Current to critical current in the CSM
$(I/I_{cr})_{lim}$	Limit value of I/I_{cr}
p_0	CP downstream pressure
p_{QT}	QT pressure
p_{lim}	Pressure limit in the CSM
p_{max}	Rupture pressure of the CSM
$p_{CSM,in}$	Inlet pressure in the CSM
T_{QT}	Temperature in the QT
T_{cs}	Current sharing temperature
T_{hs}	Hotspot temperature
T_{sat}	Saturated LHe temperature
ΔV	Electric potential of the CSM
ΔV_{lim}	Limit value of ΔV
m_{CP}	Failure magnitude of CP
m_{CV1}	Failure magnitude of CV1
m_{CV2}	Failure magnitude of CV2
m_{BV}	Failure magnitude of BV
m_{SV1}	Failure magnitude of SV1
m_{SV2}	Failure magnitude of SV2
τ_{CP}	Failure time of CP
τ_{CV1}	Failure time of CV1
τ_{CV2}	Failure time of CV2
τ_{BV}	Failure time of BV
τ_{SV1}	Failure time of SV1
τ_{SV2}	Failure time of SV2
t_{CP}	Failure time interval of CP
t_{CV1}	Failure time interval of CV1
t_{CV2}	Failure time interval of CV2
t_{BV}	Failure time interval of BV
t_{SV1}	Failure time interval of SV1
t_{SV2}	Failure time interval of SV2
ord_{CP}	Failure order of CP
ord_{CV1}	Failure order of CV1
ord_{CV2}	Failure order of CV2
ord_{BV}	Failure order of BV
ord_{SV1}	Failure order of SV1
ord_{SV2}	Failure order of SV2
t_{miss}	Mission time
τ_{val}	Validation time of Control systems
i, j	Accidental scenario
N_{train}	Number of training scenarios
N_{test}	Number of testing scenarios simulated with the real code (not in DOE)

k	Variable index
N_k	Number of variables monitored
m	Input index
M	Number of input indexes
$\boldsymbol{X}_i$	Input vector of the *i-th* scenario
X_{im}	*m-th* input element of the *i-th* scenario
$\boldsymbol{MVL_i}$	$\boldsymbol{X_i}$ input in Multiple Valued Logic
$y_i^k(t)$	*k-th* variable trend of *i-th* scenario
l, p	Time indexes
L	Total number of time points
c, ς	Cluster indexes
C	Number of clusters
Δt	Time step
$t_{LOFA,C1,i}$	Time of LOFA detection by C1 at *i-th* scenario
y_{il}^k	Value of $y_i^k(t)$ at *l-th* time
$\bar{\bar{Y}}^k$	Matrix containing each y_{il}^k at *i-th* row (only N_{train} scenarios)
$\bar{\bar{Y}}_{krig}^k$	Matrix containing each y_{il}^k at *i-th* row (only N_{krig} scenarios)
$y_{n,il}^k$	Normalization of y_{il}^k
δ_{ij}	Euclidean pointwise distance between an *i-th* scenario and a *j-th* scenario from $l = 1$ to $l = L$
$\delta_{l,ji}$	Euclidean pointwise distance between a *j-th* scenario and a *i-th* scenario from $p = 1$ to $p = l$
F	Coefficient for similarity calculation
α, β	Parameters for F calculation
$\bar{\bar{W}}$	Similarity matrix
$\bar{W}_i$	Generic *i-th* row of $\bar{\bar{W}}$
w_{ij}	Generic element of $\bar{\bar{W}}$ at *i-th* row and *j-th* column
$\bar{W}_{l,j}$	Similarity vector of a *j-th* scenario with training scenarios at *l-th* time
$w_{l,ji}$	Similarity between a *j-th* scenario and a *i-th* scenario at *l-th* time
d_i	Sum of all elements in $\bar{W}_i$
$d_{l,j}$	Sum of all elements in $\bar{W}_{l,j}$
$\bar{\bar{D}}$	Degree matrix
$\bar{\bar{L}}$	Laplacian Matrix
$\bar{\bar{L}}_{sym}$	Normalized Laplacian Matrix
λ_c	Generic *c-th* eigenvalue of $\bar{\bar{L}}_{sym}$
$\vec{u}_c$	Eigenvector of $\bar{\bar{L}}_{sym}$ associated to λ_c
$\vec{P}_c$	Generic *c-th* vector obtained from $\bar{\bar{D}}$ matrix and $\vec{u}_c$ vector
$\bar{\bar{U}}$	Matrix containing each $\vec{u}_c$ element
$\bar{U}_i$	Vector with the generic *i-th* row of $\bar{\bar{U}}$
u_{ic}	Generic *c-th* element of $\bar{U}_i$
$\bar{U}_{l,j}$	Vector with eigenspace coordinates related to $\bar{W}_{l,j}$
$u_{l,jc}$	Generic *c-th* element of $\bar{U}_{l,j}$
$\bar{\bar{T}}$	Normalization of $\bar{\bar{U}}$

$\overline{T}_i$	Vector with the generic i-th row of $\overline{\overline{T}}$
t_{ic}	Generic c-th element of $\overline{\overline{T}}$
$\overline{T}_{l,j}$	Normalization of $\overline{U}_{l,j}$
$t_{l,jc}$	Generic c-th element of $\overline{T}_{l,j}$
ρ	Fuzzy partition exponent
J_m	Objective function of FCM
$\overline{\mathcal{A}}_c$	Vector with eigenspace coordinates of the c-th centre
$\overline{\overline{\mathcal{A}}}$	Matrix containing at each c-th row $\overline{A}_c$
$\mathcal{A}_{ch}$	Generic h-th element of $\overline{A}_c$
M_{ci}	Membership of the i-th scenario to the c-th cluster
M_{lim}	Membership limit for clustering
$\overline{\overline{\mathcal{M}}}$	Matrix containing M_{ci} at c-th row and i-th column
$M_{l,cj}$	Membership of j-th scenario to c-th cluster at l-th time
$M_{l,c0}$	Membership of a scenario with no failures to c-th cluster at l-th time
$M_{rel,l,cj}$	Difference between $M_{l,cj}$ and $M_{l,c0}$
$V_{rel,l,cj}$	Difference quotient of $M_{rel,l,cj}$
q	Index of the current phase
$\overline{\overline{\mathcal{L}}}$	LOFA map
$\mathcal{L}_{cq}$	Generic element of $\overline{\overline{\mathcal{L}}}$ referring to the c-th cluster and q-th phase
Q	Number of current phases
e	Component index
$\overline{\overline{\mathcal{F}}}$	Map with prototypical failures
$\mathcal{F}_{ce}$	Generic element of $\overline{\overline{\mathcal{F}}}$ referring to c-th cluster and e-th component
E	Number of components
$V_{lim,LOFA,l}$	Limit for LOFA precursors identification at l-th time
V_{1st}	First highest $V_{rel,l,cj}$ at l-th time
V_{2nd}	Second highest $V_{rel,l,cj}$ at l-th time
c_{1st}	Cluster associated to V_{1st}
c_{2nd}	Cluster associated to V_{2nd}
$Flag_{LOFA}$	Flag for LOFA precursors identification
$t_{last,Fail,i}$	Time of last component failure before $t_{LOFA,C1,i}$
$t_{lim,i}$	Average between $t_{last,Fail,i}$ and $t_{LOFA,C1,i}$
$V_{lim,i}$	Second highest $V_{rel,l,ci}$ at $t_{lim,i}$
$M_{lim,FAIL,l}$	Limit for component precursors identification at l-th time
$Flag_{FAIL,e}$	Flag for e-th component failure
$Count_{FAIL,e}$	Number of $M_{rel,l,cj}$ that overcome $M_{lim,FAIL,l}$ at l-th time
$\mathcal{S}$	Proportional constant between l-th time and $M_{lim,FAIL,l}$
N_{iter}	Number of training attempts for each metamodel
N^*	Number of scenarios to be included in DOE
N_{MCS}	Number of scenarios generated with MC (for AK-MCS)
N_{krig}	Number of training and adaptive scenarios
$\mathcal{X}$	General input vector
$\overline{\mathcal{X}}$	Ensemble of all the N_{krig} input vectors

$\overline{\mathcal{X}}_{MCS}$	Ensemble of all the N_{MCS} input vectors
$\mathcal{X}^*$	One of the N^* scenarios
$\overline{\mathcal{X}}^*$	Ensemble of the N^* inputs
$\mathbf{MVL}^*$	$\mathcal{X}^*$ input in Multiple Valued Logic
$\mathcal{Y}$	General output vector associated to $\mathcal{X}$
$\mathcal{Y}_i$	Output vector of the i-th scenario
$\mathcal{Y}^k$	Vector with all the k-th output of DOE
$\mathcal{Y}_i^k$	k-th output element of the i-th scenario
$\overline{\overline{\mathcal{Y}}}$	Ensemble of all the N_{krig} output vectors
$\mathcal{Y}_{thr}$	Vector with threshold values
$\mathcal{Y}_{thr}^k$	Threshold value for $\mathcal{Y}_i^k$
$\mathcal{MM}^k$	Metamodel for the k-th output
$\hat{Y}^k(\mathcal{X})$	Prediction of $\mathcal{MM}^k(\mathcal{X})$
$\hat{Y}^k(\overline{\mathcal{X}})$	Prediction of $\mathcal{MM}^k(\overline{\mathcal{X}})$
$\mu_{\hat{Y}^k}(\mathcal{X})$	Mean Kriging value of $\hat{Y}^k(\mathcal{X})$
$\boldsymbol{\mu}_{\hat{Y}^k}(\overline{\mathcal{X}})$	Mean Kriging values of $\hat{Y}^k(\overline{\mathcal{X}})$
$\sigma_{\hat{Y}^k}^2(\mathcal{X})$	Kriging variance of $\hat{Y}^k(\mathcal{X})$
$\boldsymbol{\sigma}_{\hat{Y}^k}^2(\overline{\mathcal{X}})$	Kriging variance of $\hat{Y}^k(\overline{\mathcal{X}})$
$\boldsymbol{\beta}_k^T \boldsymbol{h}(\mathcal{X})$	Trend basis of $\mathcal{MM}^k$
$\boldsymbol{\beta}_k$	Regression coefficient
$\boldsymbol{h}(\mathcal{X})$	Basis function
σ_k^2	Variance of the Gaussian process
$\mathcal{Z}(\mathcal{X}, \omega)$	Zero unit mean variance
ω_k	Probability space
$\mathcal{R}(\mathcal{X}, \mathcal{X}'; \boldsymbol{\theta}^k)$	Correlation function
$\boldsymbol{\theta}^k$	Hyperparameters of $\mathcal{MM}^k$
θ_m^k	m-th element of $\boldsymbol{\theta}^k$
ξ	Ellipsoidal function
$S_{\mathbb{M}}^{(k)}$	Ensemble with scenarios of $\overline{\mathcal{X}}_{MCS}$ near the fault line
$S_{f+}^{(k)}$	Ensemble with scenarios of $\overline{\mathcal{X}}_{MCS}$ above the upper limit of the confidence interval of the fault line
$S_{f-}^{(k)}$	Ensemble with scenarios of $\overline{\mathcal{X}}_{MCS}$ above the lower limit of the confidence interval of the fault line
$\mathcal{U}^k(\mathcal{X})$	Learning function associated to the k-th variable
h	Orthogonal basis index
H_k	Last orthogonal basis index for the k-th variable
$\varphi_h^k(t)$	h-th Orthogonal basis of the k-th variable
a_{ih}^k	Coefficient associate to $\varphi_h^k(t)$ for the i-th scenario
$\overline{\overline{\Psi}}^k$	Matrix with left-singular vector in each column
$\overline{\overline{\Phi}}^k$	Matrix with right-singular vector in each column
$\overline{\overline{\Lambda}}^k$	Diagonal matrix containing Λ_i^k singular values
Λ_h^k	Singular value associated to the h-th base
Γ_h^k	Percentage of variability with POD with truncation at h-th element
φ_{lh}^k	Value reached by $\varphi_h^k(t)$ at l-th time

$\bar{\bar{A}}^k$	Matrix with coefficients of the N_{krig} scenarios related to the orthogonal basis of the *k-th* variable
$\boldsymbol{a}_h^k$	Ensemble of coefficients of the N_{krig} scenarios related to the *h-th* orthogonal base of the *k-th* variable
$\mathcal{MM}_h^k$	Metamodel for the *h-th* base coefficient related to the *k-th* output
$\hat{a}_h^k(\boldsymbol{X})$	Prediction of the coefficient of the *h-th* base for the *k-th* variable related to the $\boldsymbol{X}$ input
$\mu_{\hat{a}_h^k}(\boldsymbol{X})$	Mean Kriging value of $\hat{a}_h^k(\boldsymbol{X})$
$\sigma_{\hat{a}_h^k}(\boldsymbol{X})$	Kriging variance of $\hat{a}_h^k(\boldsymbol{X})$
$\tilde{y}_{jl}^k$	y_{jl}^k value approximated with POD-based Kriging
$G_{CSM,in}(t)$	Inlet flow in the CSM
$G_{CSM,out}(t)$	Outlet flow in the CSM
$G_{max}(t)$	Maximum flow in the CSM
$\tilde{t}_{LOFA,C1,j}$	Approximation of $t_{LOFA,C1,j}$ with POD-based Kriging
$\varphi_{G,lh}$	Value of the *h-th* base at *l-th* time for G_{max} output
g_{ih}	Coefficient of $\varphi_{G,lh}$ related to the *i-th* scenario
$\boldsymbol{g}_h$	Ensemble of each coefficient $g_{ih}(i = 1, \dots, N_{krig})$
$\mathcal{MM}_h^G$	Metamodel for the *h-th* base coefficient related to G_{max} output
$\hat{g}_h(\boldsymbol{X})$	Prediction of the coefficient of the *h-th* base for G_{max} variable related to the $\boldsymbol{X}$ input
$\mu_{\hat{g}_h}(\boldsymbol{X})$	Mean Kriging value of $\hat{g}_h(\boldsymbol{X})$
$\sigma_{\hat{g}_h}(\boldsymbol{X})$	Kriging variance of $\hat{g}_h(\boldsymbol{X})$
$\tilde{G}_{max,lj}$	Value of $G_{max}(t)$ at *l-th* time for the *j-th* scenario approximated with POD-based Kriging
$\sigma_{abs}^k(\boldsymbol{X}_j)$	Absolute error of the *k-th* variable of the *j-th* scenario employing singular values
a_{max}^k	Maximum order of magnitude of $\sigma_{abs}^k(\boldsymbol{X}_j)$
a_{min}^k	Minimum order of magnitude of $\sigma_{abs}^k(\boldsymbol{X}_j)$
$\sigma_{rel}^k(\boldsymbol{X}_j)$	Relative error of the *k-th* variable of the *j-th* scenario employing singular values
N_{POD}	Scenarios that satisfied $\sigma_{rel}^k < 10\%$ between the N_{MCS} scenarios
N_{data}	Number of training, adaptive and approximated scenarios included in the new dataset
$N_{data,c}$	Number of scenario in *c-th* cluster between the N_{data} ones
$\Theta(x)$	Heaviside function
$P_{LOFA,l}(c)$	Probability of LOFA occurrence at *l-th* time respect to the *c-th* cluster
$P_{FAIL,l}(e\mid c)$	Probability of failure of the *e-th* component at *l-th* time respect to the *c-th* cluster
$P_{LOFA,l,j}$	Probability of LOFA occurrence at *l-th* time in the *j-th* scenario
$P_{LOFA,lim}$	Limit value for $P_{LOFA,l,j}$
$P_{Cl,l}(c)$	Probability for the *c-th* cluster to be responsible of the failure
$P_{FAIL,l,j}(e)$	Probability of failure of the *e-th* component at *l-th* time for a *j-th* scenario
$P_{FAIL,lim}(e)$	Limit value for $P_{FAIL,l,j}(e)$

1 Introduction

Natural gas has been the leading source of electricity, covering the 27.4% of the world energy demand, since 2018 instead of coal, which contributes for 25.4%. All renewable source (hydro, solar, wind and others) and nuclear accounted for 24.6% and 17.5% of the world electricity, respectively. The falling of the share of coal in the last decades has been followed by an evident increase of the gas consumption and a growth of renewables technologies, in particular wind and solar ones (IEA, 2018a). However, if energy policies are not going to change, according to the "Current Policies Scenario" (i.e., future energy trend including legislation until mid-2018), the world energy demand will increase with a consequent rise of greenhouse emissions due to fossil fuels (IEA, 2018b).

Greenhouse gasses are the main drive of global warming that leads to an increase of global average temperatures of air and oceans, a propagation of snow and ice melting and a rise of the global average sea level. These changes strongly affect climates with dramatical consequences on environment and our society (IPCC, 2007). To mitigate these phenomena, an international treaty, known as Kyoto Protocol (COP-3), signed in 1997, has been ratified by 175 countries until today with the objective of reducing greenhouse emissions by at least a fixed quote (depending on the economy of the country) before 2020 with respect to the emissions of 1990. After the Paris climate conference (COP-21) at the end of 2015, a new global climate deal has been adopted by 195 countries with the aim of "holding the increase in the global average temperature to well below 2°C above pre-industrial levels and pursuing efforts to limit the temperature increase to 1.5 °C".

The European Union launched "Climate strategies & targets" in order to reduce progressively the amount of greenhouse leading to a climate-neutral economy by 2050 (EC, 2019). With the "2020 Package", whose targets were set in 2007 and enacted in legislation in 2009, a reduction of 20% in greenhouse gas emissions (from 1990 levels), the achievement of 20% of EU energy from renewables and a 20% of improvement in energy efficiency for the 2020 are promoted. These targets

are going to be revised in 2021 with the "2030 Package", set in 2014 but stepped up in 2018, leading to an abatement of 40% in greenhouse emissions, a share of 32% of renewable energy and 32.5% of improvement in energy efficiency for the 2030. These targets are going to increase after 2031 for the "2050 Package".

According to the "New Policies Scenarios" (i.e., future energy trend including actual policies intentions), and "Sustainable Development Scenario" (i.e., future energy trend including internationally agreed objectives on climate change, air quality and universal access to modern energy), electricity generation is undergoing to significant changes due to the increasing electrification in industry, transportation and buildings and heavy investments in new energy supply and low carbon technologies must be made (IEA, 2018b). Nuclear power has been one of the biggest sources of carbon-free electricity in the world reaching 1868 TWh (17,6%) in 2018 and $ 1.1 trillion of investment are going to be made to increase this capacity of 46% to 2040 (IEA, 2018a). Indeed, fission power plants are playing an important role in reducing CO_2 emission typical of fossil fuels (coal, gas, oils, …) for its better availability and capacity factor then renewables (OECD, 2012). Also, fusion power plants, that are still at research level, are attracting considerable investments to make it possible to gain energy from nuclear fusion reactions for electricity production in the future.

Studies are more addressed to the deuterium-tritium (D-T) reaction that consists in merging two isotopes of hydrogen producing an α-particle of 3.5 MeV and a neutron of 14.1 MeV. There are three main benefits coming from their use in power generation: fuel reserves, environmental impact and safety (Freidberg, 2007). Concerning fuel reserves, deuterium (whose nucleus contains one proton and one neutron) can be easily extracted from water in a cost-effective way, because there is 1 atom of deuterium every 6700 atoms of hydrogen. Tritium, that is a radioactive isotope with a half-life of about 12 years made by one proton and two neutrons, can be obtained by breeding lithium isotopes, because no natural tritium can be retrieved from earth. Natural lithium is composed by 7.4% of Li^6 (that reacting with a thermal neutron produces 4.8 MeV of energy, an α-particle and tritium), and by 92.6% of Li^7 (that reacting with a fast neutron and absorbing 2.5 MeV of energy produces an α-particle, a neutron and tritium): as a consequence, fuel reserves are

strongly connected with lithium reserves, which would provide 20000 years of clean energy (considering the actual world energy consumption). For what concerns environmental impact, D-T reactions do not produce greenhouse gasses, but helium, which is inert, and neutrons, which activates the blanket and structural materials, making them radioactive on the order of 100 years: however, this time is much shorter than the one of actinides and lanthanides in fission spent fuel on the order of million years (EC, 2004). For the last advantage, in a fusion reactor there is no risk of melt-down, because no chain reactions must be maintained like in a core of a fission reactor and the small amount of fuel, that must be constantly plugged in the core, makes the melt-down impossible (Freidberg, 2007).

Those benefits would have made fusion more attractive than fission, but fusion science is complex: D-T reactions require deuterium and tritium in plasma phase under extreme high temperatures (i.e., of the order of $150 \times 10^6 \ K$); also, plasma facing components and the blanket must withstand huge heat load and high energy neutrons. In addition, magnetic confinement fusion, that is considered more promising than the inertial one, need strong magnetic fields to confine plasma and an auxiliary heating system to increase plasma temperature. During the last half-century "fusion machines" of different size and shape, as pinch, mirror, stellarator or tokamak, have been designed and used for fusion experiments in different countries (Ikeda, 2010). Tokamaks, that stands for "TOroidalnaya KAmera MAgnitnaya Katushka" (i.e., "Toroidal Chamber and Magnetic Coil") have been playing the major role in nuclear fusion experiment. In this type of systems, the magnetic field necessary for plasma confinement is achieved by resorting to four basic magnet systems: toroidal field coils generate the toroidal magnetic field; an ohmic transformer induces the toroidal plasma current that leads to the poloidal magnetic field and, then, to an initial plasma heating; a field coil system generates the vertical magnetic field needed for toroidal force balance and shaping coils modify the cross section of the torus to non-circular shape, enhancing the MHD stability and lowering the impurity due to plasma wall interactions (Freidberg, 2007).

All tokamaks built until now do not have the goal of producing electricity, but the study of thermonuclear reactions. The first tokamak built was the T1 Soviet in Soviet Union in 1957 with a plasma chamber of 0.4 m^3 and a circular cross section. In following years, more technologies have been implemented increasing the level of sophistication and the size of the tokamaks: The ASDEX group in Garching marked an improvement of the energy confinement time in 1982 operating with a poloidal divertor. JET in Culham and TFTR in Princeton were the first tokamaks to study D-T reactions (before only D-D reactions had been studied). Neutral beam injection and radiofrequency heating were investigated as auxiliary heating systems; superconductive coils were implemented in magnet systems in order to produce higher magnetic fields driving higher current in them (exploiting the absence of ohmic heating) and so enhancing the confinement of plasma. The cooperation between countries was fundamental for addressing successfully the complexity of the physics and engineering of fusion systems: however, tokamaks capable of producing a power output considerably greater than the power input (necessary for plasma heating and plasma confinement) still do not exist (Ikeda, 2010).

Before being able to produce electricity on an industrial scale with these technologies, the feasibility of reaching a fusion energy gain factor (i.e., ratio between fusion power output and power input) of at least 10 must be demonstrated. In order to achieve this goal, the International Thermonuclear Experimental Reactor (ITER) is under construction at Cadarache in France with the cooperation of seven members (i.e., European Union, Russia, Japan, United States, Korea, India and China) and it is designed to produce 500 MW of power with an input of 50 MW. The next step will be the construction of DEMO (i.e., "DEMOnstrating fusion pawer reactor") with the objective of demonstrating the feasibility of producing electricity with thermonuclear fusion reactions. Its design will be aided by the work carried out for ITER, but also by the development of other new facilities, like the Divertor Tokamak Test (DTT), which has the task of exploring new power exhaust solutions able to withstand the heat load characterizing DEMO (Crisanti et al., 2017).

This thesis focuses on the safety analysis of a component (i.e., the cryogenic cooling circuit of one single module of the central solenoid magnet) of ITER.

ITER (International Thermonuclear Experimental Reactor) (ITER, 2018) will be the first reactor that will produce a net amount of energy exploiting fusion reactions between Deuterium and Tritium, under extreme high temperature and pressure conditions (i.e., plasma at the temperature of the order of 10^8 K). ITER is designed to respect the high safety standards of international nuclear safety guidelines following different goals: preventing and mitigating consequences of accidental scenarios, ensuring an extremely low environmental impact during operation condition and maintenance, reducing the amount of radioactive waste and improve their handling (Alzburtas et al., 2015; Taylor et al., 2014; Wu et al., 2016). Indeed, the correct management of tritium and activated materials must be guaranteed to prevent radiological contamination of worker and environment (Taylor et al., 2017; Taylor, 2016).

In ITER, plasma is magnetically confined in a torus chamber with a D-shape cross section by different Superconductive Magnets (SMs) (Bigot, 2018; Mitchell et al., 2008 & 2012): one Central Solenoid coil (CS), eighteen Toroidal Field coils (TFs), in Nb_3Sn, six Poloidal Field coils (PFs) and eighteen Correction Coils (CCs), made by NbTi. The CS, that is the object of this thesis, is constituted by six Central Solenoid Modules (CSMs). Each CSM must sustain high currents (~40kA) in order to generate high magnetic fields (several T) to confine the plasma and its superconductive properties must be guaranteed to nullify ohmic heating. These properties strongly depend on temperature of the strands of SMs, on the current density that passes through them, on the magnetic field, in which they are immersed, and on their thermal strain: if these parameters overcome a threshold value, quench (i.e., loosing of superconductive properties) may occur (Takahashi et al., 2006). For this reason, coils are cooled with Supercritical Helium (SHe) at 4.5 K with a pressure of 0.5-0.6 MPa (Mitchell et al., 2008) by a Superconducting Magnet Cryogenic Cooling Circuit (SMCCC) that is in charge of the heat extraction from the CSMs to pools of saturated Liquid Helium (LHe) (Hoa et al., 2012; Zanino et al., 2010 & 2013).

In this light, if not promptly detected, a Loss-Of-Flow Accident (LOFA) in the SMCCC may impair the CS cooling capability, possibly leading to rapid surge of the CS pressure and temperature due to the ohmic heating. If the pressure and the temperature overcome 25 MPa and 150 K, respectively, the CS could be lost (IAEA, 2002; ITER, 2006), as pointed out in numerous safety studies aimed at identifying the causes that may lead the SMCCC to work under abnormal scenarios (D'Amico et al., 2016; Wu et al., 2016; Savoldi et al., 2018; Bellaera et al., 2019). Safety of the CSMs, as well as for the other SMs, must be ensured to: (i) avoid severe damages to them because of their huge cost; and (ii) guarantee a high availability of ITER, because the replacement of such critical components is difficult, or even impossible, due to the complexity of the machine. For these reasons, multiple monitoring and detection systems have been designed to control ITER during operation (Mitchell et al., 2008 & 2012).

In this respect, a strategy is proposed in the present thesis to identify LOFA precursors (i.e., those component failures leading to a LOFA), because this scenario is considered one of the most threatening for the SMCCC and, therefore, it has to be analysed in order to undertake the proper prevention and mitigation strategies. Since it is a tricky point for an operator to promptly intervene in the presence of a large volume of monitored signals, its decision may be supported by an automatic data-driven approach that recognises the pattern of signals measured during plant operation, which may reveal the accident precursors (i.e., the failed components) (Baraldi et al., 2015a; Di Maio et al., 2016; Al-Dahidi et al., 2018). To this aim, an On-line Supervised Spectral Clustering (OSSC) method embedding the Fuzzy C-Means (FCM) algorithm is proposed as a *novel* strategy to identify LOFA precursors from signals of a developing (accident) scenario. Signals of abnormal, accident scenarios are simulated by the validated, deterministic 4C code, which is able to reproduce the overall system's response to failed components and estimate the effect of a LOFA in the SMCCC of a single module of the ITER Central Solenoid (CS) (Savoldi et al., 2010). A *limited-sized* set of 83 "exemplary" scenarios is used to "train" the proposed algorithm for LOFA precursor identification. The method is then tested to verify its robustness and validity on *new, unknown* scenarios. Results show that the approach elaborated timely recognises

several LOFA precursors and identifies most of the components failed. On the other hand, it detects LOFA precursors in scenarios with no LOFA and identifies as precursors some components that are not actually failed. On one side, this *conservatively increases* the *safety* of the SMCCC (by overestimating the number of failed components); on the other side, it *reduces* its *availability* (due, e.g., to unnecessary inspection procedures).

These limitations can be explained by the small dataset (i.e., the small number of exemplary accident scenarios) initially employed to train the LOFA precursors identification algorithm. In other words, the training set adopted only covers a very small portion of the entire state-space of the system analysed (i.e., of the spectrum of all possible system configurations). In fact, a complex system is typically composed by a large number of components. As a consequence, each accident scenario may be characterized by a (potentially large) sequence of *different events* (i.e., of different *component failures*). In addition, each component failure may be characterized by different *magnitudes* and *timings*. The combination of these properties makes the problem *high-dimensional*: a huge number of possible scenarios exist, but only few of them have been simulated because of the *very high computational cost* (requiring on average two days per simulation on an Intel Core i3-7100 3.90 GHz 3MB Cache) associated to the 4C code (Bellaera et al., 2018 & 2019; Savoldi et al, 2010).

In this light, the second part of the thesis is dedicated to the study and development of advanced computational methods able to intelligently *increase* the *number* of (accident) *training scenarios* at a *reduced* computational cost: the final objective is to improve the quality of the "maps" used for training the LOFA precursors identification approach and to consequently enhance its performance. This objective is achieved in two successive stages. In the first stage, a numerical "surrogate" model (also called "response surface" or "meta-model") is constructed that mimics the behaviour of the detailed, long-running 4C code, but with a reduced computational cost (e.g., of the order of few seconds) (Turati et al., 2018; Simpson et al., 2001). This allows a significantly larger number of simulation runs and, thus, a deeper exploration of the possible abnormal conditions of the system (to be used for learning the rules of LOFA precursors identification). Notice that numerous

safety assessments in the nuclear field exploit metamodels to efficiently explore failure scenarios and to evaluate the probabilities of rare failure events, because the computer codes typically adopted in this field require large computing times (Cadini et al., 2015; Wang et al., 2018). In more details, the metamodel is here built and *progressively refined*, within an *adaptive* framework, in proximity of the "critical" regions of our interest (i.e., the LOFA scenarios): in other words, we *preferentially* guide the exploration of the (large) system state-space towards such abnormal scenarios, making an *intelligent* use of the information and knowledge gained at previous steps and iterations of the search (Schöbi et al., 2017; Wang et al., 2007; Turati et al., 2017 & 2018). As a result, we obtain a surrogate metamodel that is very accurate in proximity of system failure (i.e., LOFA) configurations and less accurate in correspondence of ("less interesting") safe states. The algorithm employed and briefly described above is known in the literature as Adaptive Kriging – Monte Carlo Sampling (AK-MCS) (Echard et al., 2011).

In the second stage, making use of the information about system failures gained in the adaptive exploration phase described above, a Proper Orthogonal Decomposition (POD)-based Kriging metamodel is constructed (Marrel et al., 2014; Nanty et al., 2017). The main feature of this type of metamodel is to be able to reproduce quickly *time-varying* signals: in this way, new *transients* can be simulated without resorting to the detailed 4C code, thus enriching – at a negligible computational cost – the database of scenarios necessary for the improvement of the maps used in LOFA precursor identification. Results show that the performance of the algorithm is enhanced: the rate of LOFA detection is increased and the corresponding precursor identification is more accurate (in particular, the overestimation of the number of failed components is softened).

In summary, the main (methodological and applicative) contributions of this thesis are the following:

- study and development of an *original* approach to promptly *identify LOFA precursors* (i.e., those component failures leading to a LOFA), based on an On-line Supervised Spectral Clustering (OSSC) method embedding the Fuzzy C-Means (FCM) algorithm;

- implementation of different *metamodel-based approaches* (AK-MCS and POD-based Kriging) to improve the performance of the LOFA precursors identification algorithm proposed, at a *reduced computational cost* (i.e., by circumventing the burden typically associated to detailed, mechanistic simulation codes);

- first-time application of the algorithms mentioned above to a component of a nuclear fusion system (i.e., the SMCCC of a single ITER CSM).

The remainder of the thesis is organized as follows. In Chapter 2, a detailed description of the simplified SMCCC is provided accompanied by information of the SMs of ITER and of the deterministic code 4C (Savoldi et al., 2010) used to simulate one of the six CSMs. Then, the LOFA precursors identification algorithm is presented in Chapter 3, together with information on the dataset generated for its training and the results of its application to new, unknown test scenarios. Chapter 4 describes the use of metamodels to enhance the performance of the LOFA precursor identification algorithm of Chapter 3. In particular, the AK-MCS method is first presented and employed to efficiently and deeply explore the system failure region, thus gaining useful information about those system configurations leading to a LOFA. Then, the POD-based Kriging metamodels is described and used to "mimic" the behaviour of the 4C code with a reduced computation cost: this allows generating a large number of new time-varying signals (transients) to enrich the "maps" used for training the LOFA precursors identification approach. Lastly, the LOFA precursors identification algorithm of Chapter 2 is customized for the new dataset and tested on new scenarios. Finally, conclusions are drawn in Chapter 5.

2 Case studied

ITER (Figure 2.1) is one of the most innovative and challenging international scientific projects in the world today: it will be the largest tokamak with a D-shape cross section and a plasma volume of 840 m³, where D-T thermonuclear reactions are achieved under extreme conditions, reaching temperature of the order of 150 million °C, a plasma density of 10^{20} particle/cm³ (necessary to increase the frequency of collision between particles) and adequate confinement time (maintaining plasma in a defined volume). This prototype has different goals: (i) demonstrating the feasibility of producing 500 MW of output with a fusion energy gain factor of 10, (ii) testing technologies for fusion power plants (i.e., auxiliary heating and cryogenic systems, control, diagnostics and remote maintenance), (iii) achieving stable D-T reactions for long duration by exploiting internal heating from α-particles, (iv) demonstrating the feasibility of making tritium from mock-up in-vessel tritium breeding blankets and (v) demonstrating the safety characteristics of fusion plants (ITER, 2018).
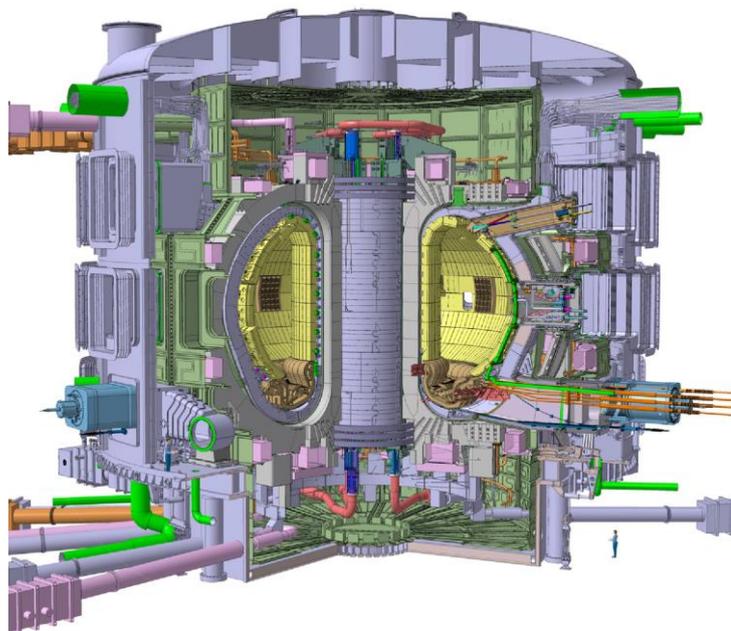
Figure 2.1 A detailed cutaway view of the future ITER tokamak [Source (ITER, 2018)]

2.1 The Superconductive Magnets

Plasma confinement is realized with a systems of SMs that generate magnetic fields of several Tesla: eighteen Toroidal Field coils (TFs), one Central Solenoid coil (CS), constituted by six Central Solenoid Modulus (CSMs), six Poloidal Field coils (PFs) and eighteen Correction Coils (CCs) (Figure 2.2). The TFs generate the toroidal magnetic field necessary for plasma stability, the CS, through an inductive flux, produces a toroidal current inside plasma, which in turn brings the poloidal magnetic field for plasma equilibrium, the PFs provide the magnetic field required for plasma vertical stability and for plasma pressure confinement and the CCs enhance plasma positioning correcting possible distortion in the magnetic field, for example, due to busbars and feeders (Mitchell et al., 2008; Koizumi, 2013).
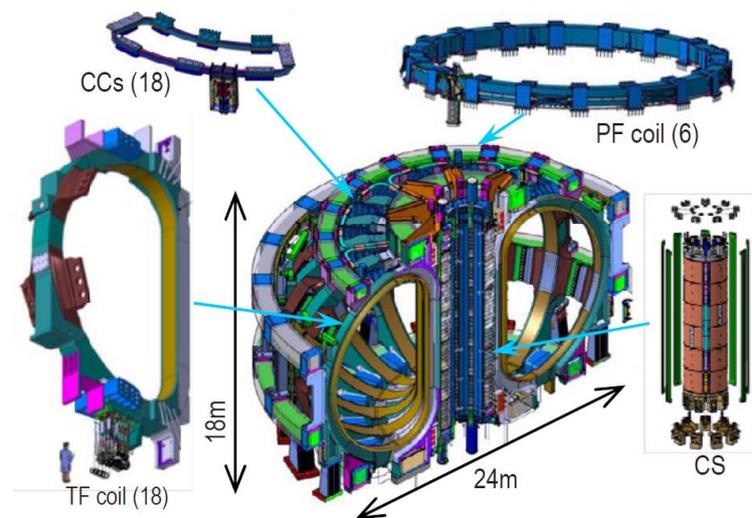
Figure 2.2 ITER Superconductive Magnets [Ref. (Koizumi, 2013)]

All SMs exhibit superconductive properties, such as a null electrical resistance and the expelling of magnetic flux fields, below a characteristic critical temperature: with the absence of ohmic heating huge electric currents can be run inside them generating magnetic field of the order of Tesla. However, the magnetic field that covers the SMs, the density of the current that flows through them and the strain which they undergo contribute to reduce their critical temperature, that depends also on the material from which they are made (Takahashi et al., 2006). Specifically, the TFs and the CS are made by Nb_3Sn, while the PFs and the CCs by NbTi: the cross

sections of each Cable-In-Conduit Conductor (CICC) that compose the SMs are shown in Figure 2.3 (a).

Each CICC is made by about 1000 strands wounded around a spiral tube like in Figure 2.3 (b), excepting for the ones of the CCs, made by about 300 strands without the presence of any spiral: 2/3 of the strands are manufactured with thousands of filaments with superconductive materials in a matrix of copper and the remaining 1/3 are pure copper strands. A stainless-steel jacket, that is squared for the CS and the PFs and circular for the TFs, cover all the strands.
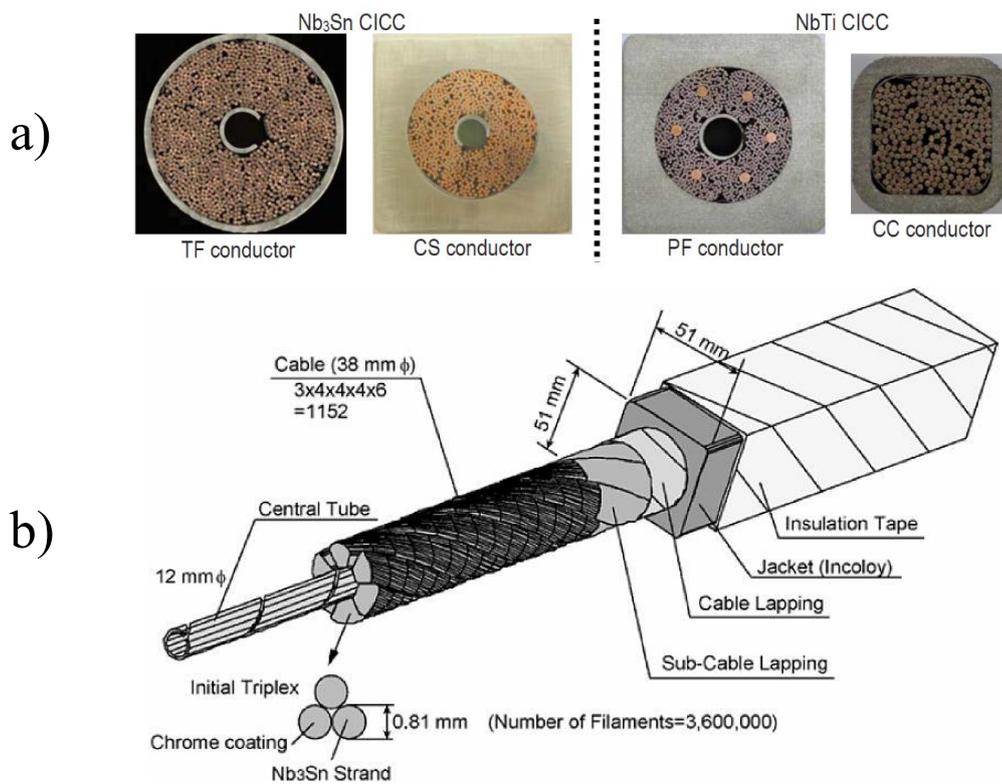
Figure 2.3 Cross section of the CICC of each SM (a) [Ref. (Koizumi, 2013)]; CICC of the CS (b) [from (Takahashi et al., 2006)]

The SMs must be maintained at cryogenic temperatures to preserve their superconductive properties and, so, they are cooled with Supercritical Helium (SHe) at 4.5 K and 0.42 MPa that is characterized by a proper heat capacity at this state: this is enabled by feeders that connect the Superconducting Magnet Cryogenic Cooling Circuit (SMCCC) with the SMs (Figure 2.4). This temperature is a good compromise for the operating points of all the SMs: the TFs and the CS operate in the range of 12-13 T, while the PFs and the CCs, made with cheaper

material, operate below 6 T. Several monitoring and protection systems, such as inherent features, detection/monitoring systems (active during operation condition) and testing systems (active at plasma interruption or at discharge of the SMs) are integrated into the devise, because magnets faults are difficult to be repaired and they reduce the availability of the machine. Indeed, huge mechanical stress and high energy handled by the SMs may impact neighbouring systems, such as tritium confinement barriers (Mitchell et al., 2012).
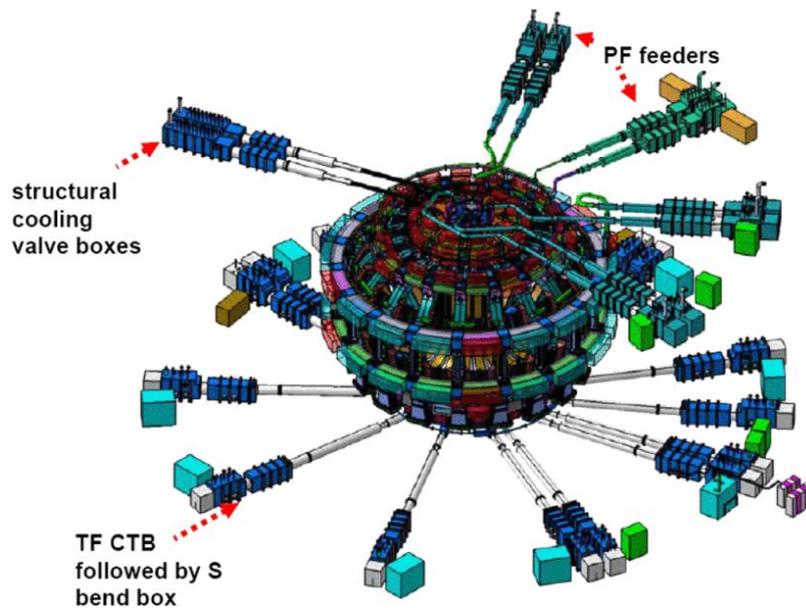
Figure 2.4 Overview of feeders [Ref. (Mitchell et al., 2008)]

The SMs work at different conditions: the eighteen TFs, fed by steady state current at 68 kA, produce a magnetic field with a total energy of 41 GJ and a peak of 11.8 T; the CS has a magnetic stored energy of 6.4 GJ with a magnetic field peak of 12.5 T, realized with pulsed current with peaks of 45-46 kA driven in its six modulus; the magnetic field generated by the PFs has a magnetic energy of 4 GJ and a field peak of 6 T, generated by varying current with peaks of 45 kA; smaller current with peaks of 10 kA is run in the CCs producing fields with lower magnetic energy. The interaction between magnetic fields and flowing currents generates strong Lorentz forces in the SMs and a mechanical support system is necessary to maintain these significant mechanical stresses. Each TFs is enclosed in a TF case in stainless steel: 4 Outer Inter-coil Structures (OIS) and 2 Intermediate Inter-coil Structures (IIS), that connect the curved region of the TF case with 3 Pre-Compression Rings (PCR),

link together the 18 TFs as shown in Figure 2.5 (left). This mechanical structure helps also to maintain the PFs and the CCs at their position. Instead, a precompression structure, made by ties (hold together by a centring system) located at the inner and outer diameter of the CS, keep the CS fixed. Gravity support systems are necessary to hold the weight of the stainless steel structures and the SMs with a total weight of about 6000 ton for the CS structure and 3400 ton for the TF structure (D'Amico et al., 2018; Mitchell et al., 2008).
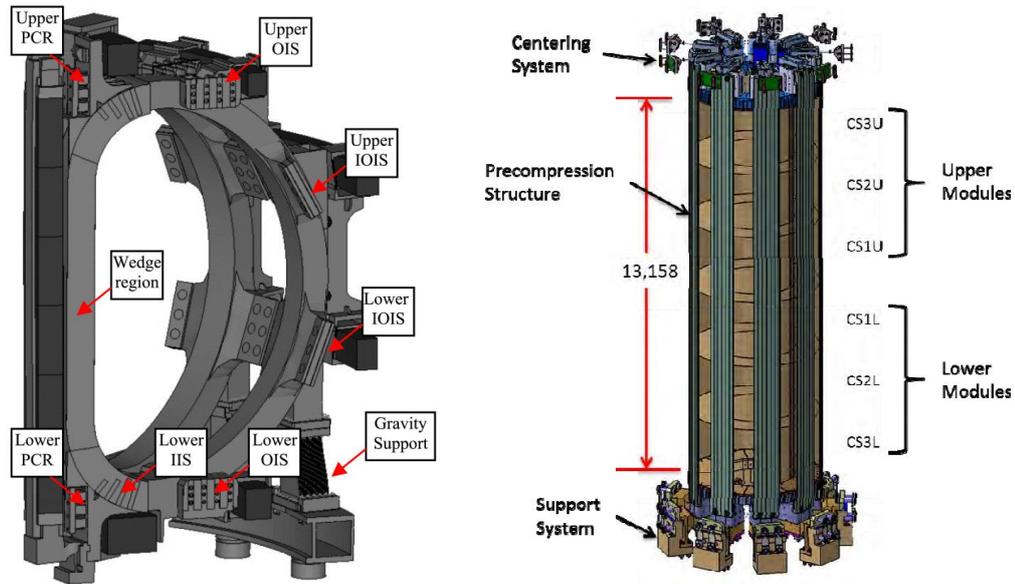
Figure 2.5 ITER Magnet system, overview of a 40 degree section. Toroidal field coil system is in light grey; poloidal field coils system and central solenoid system are in dark grey (left) [Ref. (D'Amico et al., 2018)]; Overview of the CS assembly (right) [Ref. (Everitt et al., 2013)]

The CS is the object of this thesis. In order to induce a toroidal plasma current of 15 MA for 300-500s, the CSMs that compose the CS have six independent profiles of current. After they are magnetized together for about 6 minutes reaching 40 kA, they will be discharged differently to initiate the plasma current: current drops to zero in the outer CSMs and changes direction in the inner ones. In order to maintain the plasma current at a fixed value for more than 500s, the current continues to increase in the inner CSMs reaching values of 46 kA. Afterward, all the CSMs are discharged. The magnetic flux variation inside the CSM (due to current variation in the CSMs) is necessary to maintain the electric potential to drive plasma current according to Faraday-Neumann law, but AC losses are proportional to current time-derivative (ITER, 2018). Particularly, we will focus more on the CS1U, because inner CSMs sustain higher AC losses than the outer ones, increasing more the inside

temperature of the coil, and their current sharing temperature is lower, because they are immersed in higher magnetic field.

Each CSM is composed by three hexa-pancakes (HPs), a single quad-pancake (QP) and other three HPs disposed in series by means of electric joints (Savoldi et al., 2014). The single pancake is built wrapping the single CICC fourteen times at the same height before passing above these windings and repeating the bending procedure for four or six times for the HP and the QP, respectively: the wrapping phase is started from the outer side of the CSM finishing at its outer part, so all the electric joints are located on the outer side of the CS connecting in series all the CICCs. From the wrapping procedure of seven CICCs there will be forty different channels at different heights from the bottom to the top of the CSM. At each channel there is a hole in the inner side of the solenoid connected with the feeder of the SMCCC and another one in the outer side. In this way, there are 40 separate hydraulic channels which are connected in parallel to the cryogenic system: the supercritical helium (SHe) is feed from the inner part to the outer one in each channel as shown in Figure 2.6.
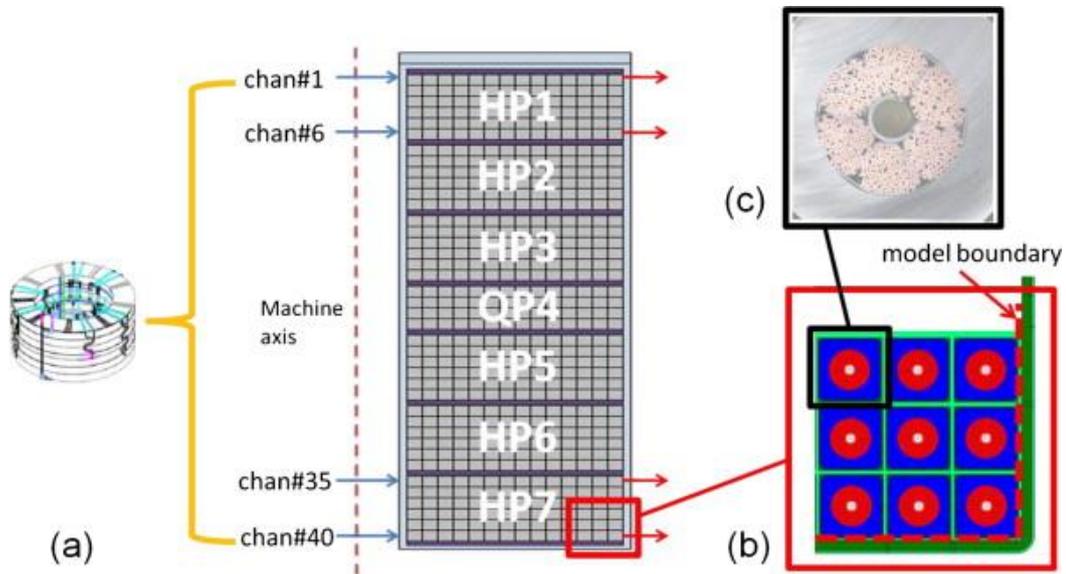
Figure 2.6 Cross section of an ITER CS module (a), with a zoom showing the insulation layer between adjacent turns (b) and down to a single CICC (c) [From (Savoldi et al,, 2018)]

The validated deterministic 4C code has been used to model both the SMCCC and the coil.

2.2 The 4C code

The Cryogenic Circuit Conductor and Coil code (4C code), designed at "Politecnico di Torino" (Savoldi et al., 2010), is a validated deterministic code embedding the Mithrandir code (Zanino et al., 1995) and the multi-conductor Mithrandir (M&M) code (Savoldi et al., 2000a).

The Mithrandir code allows to solve the 1-D thermal-hydraulic model for both the two fluid regions of the CICC separated by the spiral tube: indeed, the SHe that flows inside the central region has a different thermodynamic state (i.e., flow speed, pressure and temperature) than the one in the bundle, but the two channels communicate each other, so a set of Euler equations is employed to solve the thermodynamic state of the SHe of the two streams. Also, the jacket and the strands are included in the model embedding transversal heat transfer phenomena in the 1-D model, thermally coupling them with themselves by conduction and with the SHe convectively, enabling to evaluate their temperature: external heating and internal one, such us Joule effect and AC losses, are accounted, too. All coefficients and properties needed to solve the set of equations are gathered by a Computational thermal-Fluid Dynamics (CtFD) analysis in small portions of the CICC and then averaged over the cross-sections.

However, the Mithrandir code enables to solve separately the single channels of the CSM, but the M&M code overcomes this limit implementing heat conduction phenomena in each radial section of the CSM between the 40 channels. This code has shown comparable results respect to real experiments in estimation of current sharing temperature (i.e., temperature when current starts flowing in copper strands) and other variables in the CSM with shots of current of different intensity as input (Savoldi et al., 2000a & 2000b).

Instead, in 4C code, differently from the Mithrandir and the M&M codes, a 1-D compressible fluid model (for pipes and heat exchangers) based on Dymola and a 0-D model for the mass and the energy balance in relevant points of the cooling loop (such as valves, tanks, pump, ...) are also integrated (Savoldi et al., 2010). This code has been validated several times: for instance, a study on the safety discharge

16

of a TF coil at 25 kA and on the HELIOS loop under pulsed load operation were performed showing results comparable to the experimental data (Zanino et al., 2011 & 2013).

In this thesis, the 4C code is employed to simulate the closed loop of the CS1U coupled with a simplified version of the SMCCC under fault conditions, paying particular attention to the effect of Loss-Of-Flow Accident (LOFA) possibly caused by component failures. Only one CSM is here considered because of the high computational cost associated to the 4C code (about two days per scenario simulation).

2.3 The simplified Superconducting Magnet Cryogenic Cooling Circuit

A simplified version of the SMCCC, that cools only one CSM (the CS1U), is here proposed. Figure 2.7 sketches the simplified scheme of the circuit employed also in (Bellaera et al., 2019): the Centrifugal Pump (CP) keeps the coolant in motion in the two cryolines, guaranteeing a nominal flow $G_0 = 0.32$ kg/s and a downstream pressure $p_0 = 0.42$ MPa at nominal operational conditions (Froio et al., 2016; Bellaera et al., 2019); the heat exchanger HX2 removes the heat produced in the CSM, while the HX1 cools the SHe after the compression in the CP with Liquid Helium (LHe) at saturated condition ($T_{sat} = 4.5$ K); Control Valves (CV1 and CV2) are Normally Open (NO) during nominal operational condition, while the two Safety Valves (SV1 and SV2) and the By-pass Valve (BV) are Normally Closed (NC); the by-pass line, where the BV is located, connect the downstream of HX1 with the upstream of CP; two Quench Lines (QLs), where the SVs are located, allow the communication of the input and the output of the CSM with the Quench Tank (QT) for the safety discharge of the coolant in case of quench; controllers C1 and C2 receive signals from flow meters and pressure detectors, respectively. In each scenario, the simulation has been performed during the mission time $t_{miss} = 3600s$.

17
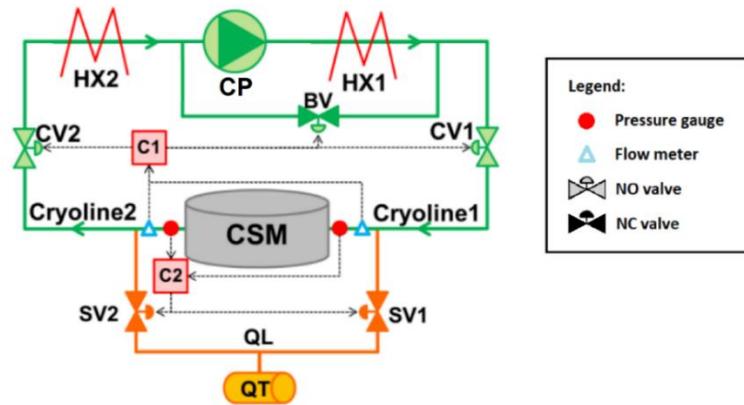
Figure 2.7 Simplified SMCCC [adapted from (Bellaera et al., 2018)]

2.3.1 Control systems

The CSM, as for each SM, must work at cryogenic condition in order to maintain its superconductive properties. Indeed, superconductivity is preserved, if three parameters, which are the magnetic field, the temperature and the current, are below a certain limit. In addition, presence of strain due to mechanical pressure, temperature gradients and Lorentz forces, contribute to reduce these limits.

A critical surface in a 3-D space with respect to these parameters is shown in Figure 2.8: it is derived from critical current vs. strain, magnetic field and temperature correlation described in (Bottura et al., 2009) setting a total strain of the strands of -0.49% and scaling parameters like in (Martovetsky et al., 2017). If operation conditions fall above this surface (i.e., at least one parameter above the limit), superconductivity will be lost.
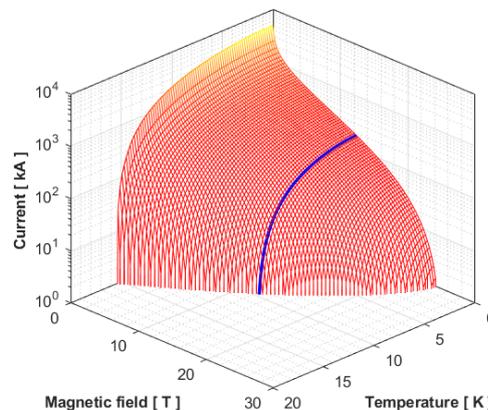
Figure 2.8 Critical surface of the CSM (red) and critical current of the CSM at B=12.5 T (blue)

An example of a scenario where superconductivity is lost is reported in Figure 2.9. Initially, during operation condition (I_{op}, T_{op}) all the current flows through the Nb3Sn strands, because the operative current I_{op} is below the critical curve at operative temperature T_{op}, and the same happens until the current sharing temperature (T_{cs}) is reached. Once this value is overcome, only a portion of I_{op}, matching the critical current at the reached temperature, flows inside the superconductive strands (I_{SM}) and the remaining part starts to run through the cooper matrix (I_{Cu}). Above critical temperature (T_{cr}), quench is occurred and all the current passes through the copper strands, that have an electric resistance lower than the ones made by Nb3Sn without superconductivity.
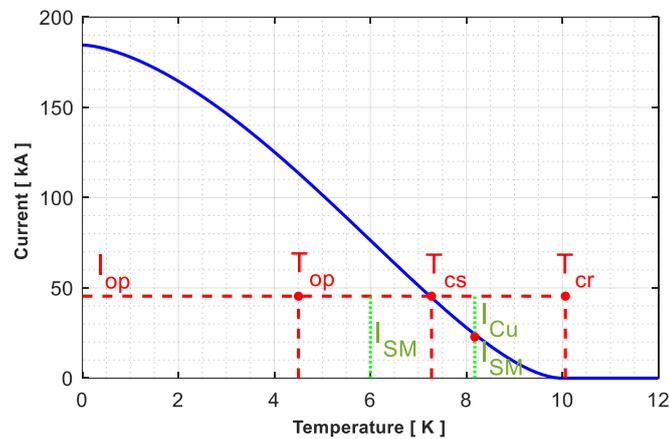
Figure 2.9 Critical current of the CSM (setting a total strain of -0.49% and a magnetic field of 12.5 T) (blue); possible operative points (red)

Temperature inside the CSM must not exceed T_{cs} and not T_{cr}, because ohmic heating consequent to the electric current inside copper starts at this point accelerating more rapidly the temperature raising.

A rapid increase of the temperature may lead to an excessive thermal stress inside the CSM, melting in a located region or a huge pressure increase. In the first two cases, the CSM strands may be damaged degrading the maximum current they can carry and leading to possible replacement of the component that is expensive and difficult to be substituted. In the last case, the integrity of joints in the CSM is at risk. This situation may lead to possible cascade events, especially if quench is not promptly detected, leading to theoretical potential damaging of neighbouring components: for instance, SHe may be sprayed into the vacuum vessel or the tritium

19

breeding system may be damage by impact or by heating (D'Amico et al., 2016 & 2018; Mitchell et al., 2012).

At operation condition, AC losses, proportional to the time derivative of the current, may increase the temperature inside the CSM and, then, the chance of quench occurrence, if not enough SHe is provided into the CSM to extract the heat. In case of a LOFA, there is a complete stagnation of the coolant (i.e., mass flow rate about at 0% of the nominal value) in the CSM and its integrity is in danger. For this reason, the mass flow rate of SHe at the inlet and at the outlet of the CSM is monitored by two mass flow meters and LOFA is detected conservatively, if both sensors measure a flow below 10% of the nominal value (equal to 0.032 kg/s) for more than the validation time ($\tau_{val} = 1s$) as performed in (Savoldi et al., 2018). In this case, the controller C1 closes CV1 and CV2 and opens BV to prevent the CP failure and dumps the current inside the CSM in 30s independently from the value reached by the current (ITER, 2014), so that SHe can only flow through the by-pass line, isolating the CSM and reducing the inventory of bi-phase helium at CP upstream. In this way, the CP is maintained in a fail-safe condition operating with SHe cooled by the HX1. For the duration of the ramp down of the current, AC losses are generated for current variation and the heat deposition rise the temperature, because no coolant is provided for the closure of the CVs. A fast temperature increase may involve in an expansion of the SHe with a consequent pressure rise. For this reason, the controller C2, that acts like a PID controller (with proportional gain = $1\cdot10^{-7}$ Pa^{-1}, integration time = 0.2 s, derivation time = 1 s) connected to pressures gauges at the input and at the output of the CSM, opens the two SVs when the pressure in the CSM overcomes $p_{lim} = 1.8$ MPa, sending SHe in the Quench Tank (QT), at pressure $p_{QT} = 0.35$ MPa and temperature $T_{QT} = 300$ K (Bellaera et al., 2019), preserving the integrity of the CSM.

2.3.2 Critical variables

In this thesis, different variables are monitored to verify the integrity of the CSM. For each *i-th* simulation, $N_k = 3$ variables $y_i^k(t)$ $[k = 1,2,...,N_k]$ are monitored at time *t*: the pressure $p_{CSM,in}$ at the inlet of the CSM ($k = 1$), that must not exceed

$p_{lim} = 1.8\,MPa$ (set point at which C2 opens the SVs for the integrity of joints and headers adjacent to the CSM during quench); the hotspot temperature T_{hs} in the CSM ($k = 2$), that must not exceed the current sharing temperature $T_{cs} = 7.3\,K$; the ratio I/I_{cr} between the current flowing in the conductors that wraps the CSM and the critical one ($k = 3$), that must not exceed $(I/I_{cr})_{lim} = 0.5$ (that indicates how the electric current is near to the maximum current capacity of the CSM at certain magnetic field, temperature and mechanical stress).

2.3.3 The simulator

This circuit is simulated by means of the 4C code employing the Modelica scheme of the simplified SMCCC shown in Figure 2.10, also adapted from (Bellaera et al., 2018 & 2019). Each component used in this scheme is described in (Zanino et al., 2012).
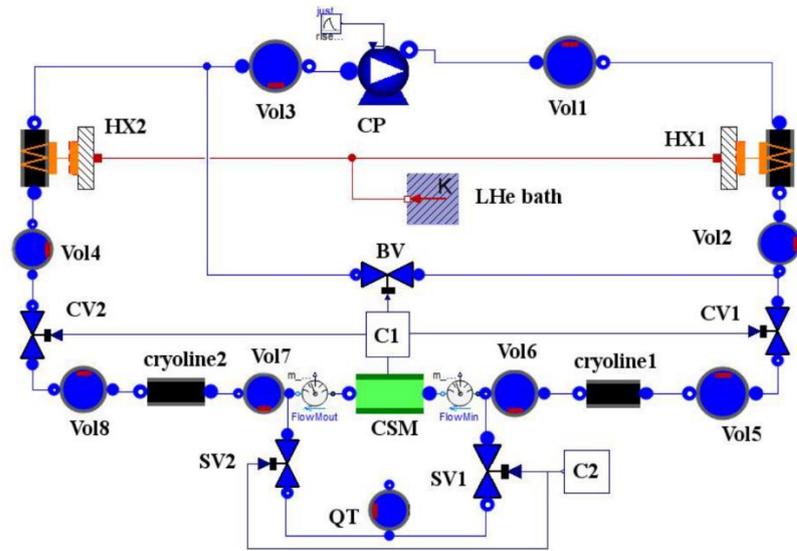
Figure 2.10 Modelica scheme of the Simplified SMCCC [adapted from (Bellaera et al., 2018)]

Thermodynamic state of SHe along pipes (HXs, Cryoline 1, Cryoline 2) is solved with a set of 1-D mass, momentum and energy balance equations with a finite-volume discretization: pipe characteristics needed to evaluate the pressure drop are shown in Table 2.1.

Table 2.1 Pipes characteristics

	diameter	Friction multiplier	length
Cryoline 1	46 mm	10^{-5}	28 m
Cryoline 2	46 mm	10^{-5}	24 m
1 of the 11 pipes of HX	20 mm	$1.5 \cdot 10^{2}$	31 m

Each HX is modelled as an ensemble of 11 parallel pipes immersed in a "LHe bath" with the hypothesis of perfect phase separation and thermodynamic equilibrium between liquid and gas helium: for this assumption, the pipe wall temperature of HXs is assumed constant at 4.5 K and it absorbs heat convectively from the SHe through a wet perimeter of 10^{5} m.

The additional presence of SHe inside the circuit between components is accounted with 9 volumes, where physical quantities are evaluated with a set of 0-D mass and energy balance equations. Also the QT is modelled as a volume, but with higher size and temperature. All the information about these values are listed in Table 2.2.

Table 2.2 Volumes characteristics at initial condition

	Volume	Pressure	Temperature
Vol1	10^{-1} m^3	0.42 MPa	4.5 K
Vol2	10^{-4} m^3	0.42 MPa	4.5 K
Vol3	10^{-1} m^3	0.345 MPa	4.5 K
Vol4	10^{-4} m^3	0.345 MPa	4.5 K
Vol5	10^{-4} m^3	0.42 MPa	4.5 K
Vol6	10^{-3} m^3	0.42 MPa	4.5 K
Vol7	10^{-3} m^3	0.345 MPa	4.5 K
Vol8	10^{-4} m^3	0.345 MPa	4.5 K
QT	10 m^3	0.35 MPa	300 K

The CP operation is simulated with the pump characteristic in (Zanino et al., 2013), providing a nominal flow $G_0 = 0.32$ kg/s inside the CSM. Its length and flow area are set equal to 0.2 m and $3.46 \cdot 10^{-3}$ m^2, respectively. Its failure is modelled varying the mass flow rate provided by the CP.

When the coolant passes through a valve, it undergoes an isenthalpic transformation and pressure drop is estimated from the flow, employing ISA S75 (IEC 60534 mod)

norms. It is considered a length of 0.2 m for all the valves and a flow area of $3.46 \cdot 10^{-3}$ m^2 for the CVs and the BV and of $3.46 \cdot 10^{-4}$ m^2 for the SVs. They are also characterized by a state, that corresponds to the mass flow rate ratio between the output and the input: 0 is the value corresponding to a close valve and 1 to an open valve. Controllers C1 and C2 act on these values: states of CVs and BV will be altered to 0 and 1, respectively, by the C1 when LOFA is detected; the SVs are controlled, instead, by the PID controller C2 that changes their state from 0 to 1, if p_{lim} is overcome.

Failures of the valves are modelled acting on their state after the failure occurrence: the state of the fault valves cannot be changed by C1 and C2 once the event is occurred. If a NO valve remains stuck opened or if a NC valve completely opens, its state will be 1, otherwise, if a NO valve completely closes or if a NC valve remains stuck closed, its state will be 0. Instead, if a NO valve closes with a reduction of the flow section area of 50% or if a NC valve opens with the flow section area at 50%, its state will change to 0.18, because, it corresponds to the mass flow rate ratio between the output and the input of the valve with the hypothesis of an equal-percentage flow characteristic (i.e., the most common valve characteristic) (Fisher, 2017; Bellaera et al., 2018).

For what concern the CSM, the flowing current, whose pulse is showed in Figure 2.11 between the two red points, is fed to the simulator as a time-varying parameter. The single pulse of current follows $Q = 5$ phases (Savoldi et al., 2014).

1) First Magnetization phase (FM): in the first 130s the current varies from 40 kA to -40 kA in 80s leading to large AC losses and Eddy currents.
2) Burning Phase (B): the current decreases to -45.5 kA for 386s.
3) Rump Down phase (R): the current reaches 0 kA at 975s.
4) Dwell phase (D): no current flows in the CSM until 1490s (to cool down the CSM after the heat load of the previous phases).
5) Last Magnetization phase (M): current returns to the initial value of 40 kA and, after a plateau of 10s, the pulse starts again for other 1800s.
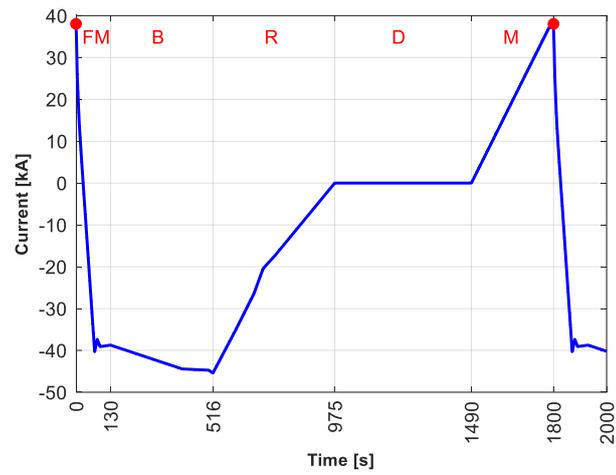
Figure 2.11 Single pulse of current in the ITER CSM

This electric current contributes to the variation of magnetic field and strain inside the CSM, that are important for physical properties employed in 4C to compute all the output at every time step.

3   LOFA precursors identification algorithm

In this Chapter, a new strategy to identify LOFA precursors (i.e., those component failures leading to a LOFA) is proposed. Indeed, LOFA may lead to abnormal scenarios and proper prevention and mitigation strategies must be timely undertaken. The proposed method consists on an On-line Supervised Spectral Clustering (OSSC) method embedding the Fuzzy C-Means (FCM) algorithm that identify LOFA precursors from signal of a developing scenario: it recognises the pattern of signals measured during plant operation, which may reveal the accident precursors (i.e., the failed components) with a data-driven approach. In this way, operator decision may be supported for prompt intervention in the presence of a large volume of monitored signals (Baraldi et al., 2015a; Di Maio et al., 2016; Al-Dahidi et al., 2018).

The dataset, generated with rules submitted in Section 3.1 and employed in LOFA precursors identification algorithm, is presented in Section 3.2, while the OSSC is described in Section 3.3. Afterward, the devised algorithm is tested on new $N_{test} = 38$ scenarios not included in the dataset. All the signals needed and presented in Section 2.3.2 were simulated with the 4C code able to reproduce the system response of the SMCCC and the SMs under abnormal scenarios (Savoldi et al., 2010).

3.1   Accidental scenario generation

In the case studied, only failures of CP, CV1, CV2, BV, SV1 and SV2 may occur in a range between 0s and 1800s (time length of a single pulse) and control systems are assumed to work correctly as performed in (Bellaera et al., 2019). These failures may lead any of the limits for $p_{CSM,in}$, T_{hs} and I/I_{cr} to be overcome. For example (Bellaera et al., 2019):

- The CP may decrease the rotational speed (leading to the reducing of the mass flow rate) at: i) 75%, ii) 50%, iii) 25% or iv) 0% of the nominal value.

- NO valves (CV1 and CV2) may fail in three different ways: i) stuck opened at nominal position; ii) partially closed with a flow area at 50 % of the nominal one; iii) completely closed.

- NC valves (BV, SV1 and SV2) may fail in three different ways: i) stuck closed at nominal position; ii) partially opened with a flow area at 50 % of the nominal one; iii) completely opened.

Each accidental *i-th* scenario is characterized by a sequence of events described by a vector of $M = 12$ elements $\boldsymbol{X}_i = [m_{CP}, \tau_{CP}, m_{CV1}, \tau_{CV1}, m_{CV2}, \tau_{CV2}, m_{BV}, \tau_{BV}, m_{SV1}, \tau_{SV1}, m_{SV2}, \tau_{SV2}]$, built with a Monte Carlo approach: for each component the magnitude (m) of the failure and the time (τ) at which the failure occurs are listed.

The *magnitude (m)* is assumed as follows:

- The magnitude of the CP can be a value between 0 and 4. If the component is not failed, $m_{CP} = 0$. Instead, if m_{CP} is equal to 1, 2, 3 or 4, these values correspond respectively to a reduction of the mass flow rate of 75%, 50%, 25% or 0% of the nominal value due to a decrease of its rotational speed.

- The magnitude of NO valves (CV1 and CV2) can assume a value between 0 and 3. If the component works correctly, $m = 0$. Instead, if m is equal to 1, 2 or 3, the considered valve remains respectively stuck opened, partially closed with a reduction of the flow section area of 50% or completely closed.

- For the magnitude of NC valves (BV, SV1 and SV2) there could be four possible values, too. If the component is not failed, $m = 0$. Otherwise, if m is equal to 1, 2 or 3, the considered valve remains respectively stuck closed, partially opened with the flow section area at 50% of the one completely opened or completely opened.

The *failure time (τ)* is a discrete value between 0s and 1800s. If the component works correctly, τ is null.

For instance, if the input vector is equal to $\boldsymbol{X}_i = [2, 60, 2, 1785, 1, 689, 0, 0, 1, 856, 3, 1405]$ the scenario to be simulated with 4C entails the failure of the CP at 60s with the flow at 50% of the nominal value, the valves CV2 and SV1 stuck at their

nominal position at 689s and 856s respectively, the complete opening of SV2 at 1405s and the partial closing of CV1 at 1785s, whereas the BV works correctly for all the transient.

The entire sequence of event of the $\boldsymbol{X}_i$ input may be visualized better resorting to Multiple Valued Logic (MVL) approach (Garribba et al., 1985), where the *failure order (ord)* and the *failure time interval (t)* replace the *failure time (τ)*.

- The *time (t)* is discretized in 6 time intervals of 300s numbered 1 to 6. These values correspond respectively to [0s, 300s], [301s, 600s], [601s, 900s], [901s, 1200s], [1201s, 1500s], [1501s, 1800s]. If t is null, it means the component works correctly.

- The *order (ord)* can assume values between 1 and 6: if a component fails with $ord = 1$, it means that it is the first event that occurs. Otherwise, if $ord = 6$, other 5 components failed before. If a component is not failed, its *order* is equal to "NaN". This value is necessary to store the order of the failures of two or more components that happen at the same time interval: in fact, this number is never redundant.

In this way, a $\boldsymbol{X}_i$ input can be associated to a $\boldsymbol{MVL}_i = [m_{CP}, t_{CP}, ord_{CP}, m_{CV1}, t_{CV1}, ord_{CV1}, m_{CV2}, t_{CV2}, ord_{CV2}, m_{BV}, t_{BV}, ord_{BV}, m_{SV1}, t_{SV1}, ord_{SV1}, m_{SV2}, t_{SV2}, ord_{SV2}]$. For instance, if $\boldsymbol{X}_i$ is the same of the previous example, the corresponding $\boldsymbol{MVL}_i$ will be $[2, 1, 1, 2, 6, 5, 1, 3, 2, 0, 0, NaN, 1, 3, 3, 3, 5, 4]$, because in that scenario the failure of the CP is in the 1st time interval [0s, 300s] with the flow at 50% of the nominal value, the valves CV2 and SV1 stuck at their nominal position during the 3rd time interval [601s, 900s], the complete opening of SV2 during [1201s, 1500s] and the partial closing of CV1 during the last time interval [1501s, 1800s], whereas the BV works correctly for all the transient.

Resorting to MVL and employing these settings, 10^8 possible accidental scenarios can be generating (Bellaera et al., 2019).

3.2 Initial Dataset description

Among all the 10^8 possible scenarios, $N_{train} = 83$ randomly selected scenarios have been simulated and clustered in $C = 9$ groups with the aim of identifying "classes" of abnormal transients in the CSM (Bellaera et al., 2019).

Figure 3.1, Figure 3.2 and Figure 3.3 show the behaviour of $p_{CSM,in}$, T_{hs} and I/I_{cr} (dotted lines) for the N_{train} transients, grouped in clusters: for each cluster the prototypical transient (i.e., the transient belonging to a cluster with the largest value of membership, which can be taken as most characteristic of the cluster (Baraldi et al., 2015b) is also plotted (continuous line).
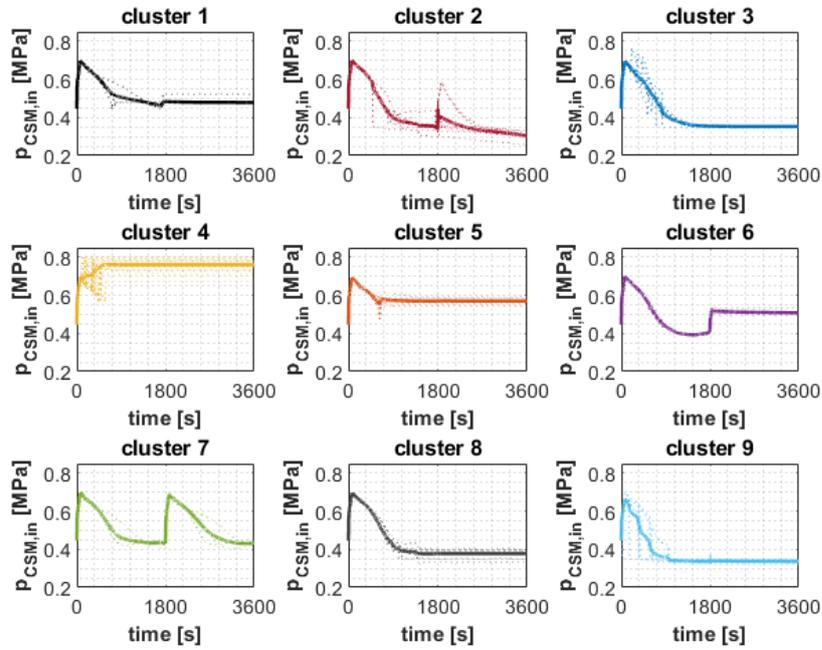
Figure 3.1 Prototypical behaviour of $p_{CSM,in}$ for each cluster
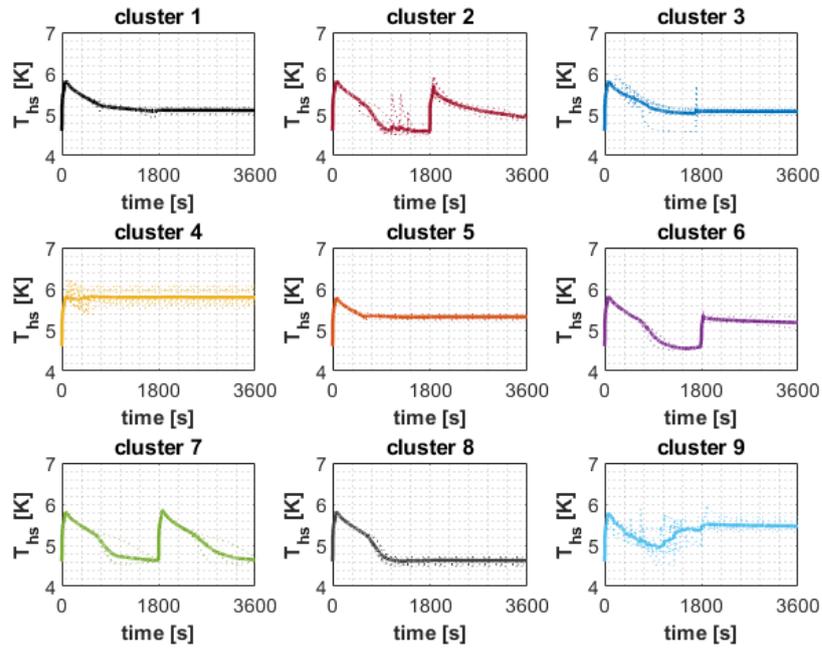
Figure 3.2 Prototypical behaviour of T_{hs} for each cluster
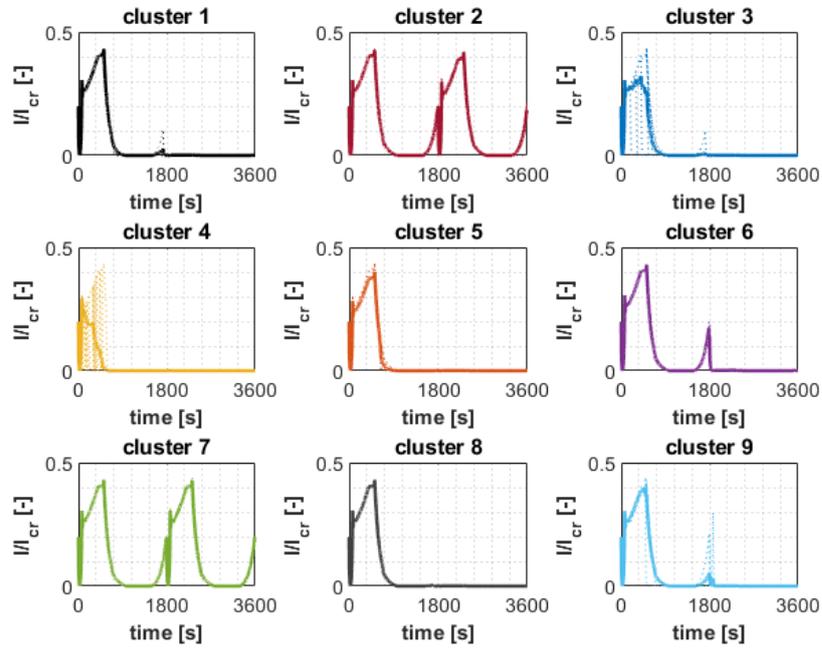
Figure 3.3 Prototypical behaviour of I/I_{cr} for each cluster

It is worth pointing out that scenarios of cluster 4 show the largest values of $p_{CSM,in}$ and T_{hs} (without overcoming the threshold limits p_{lim} and T_{cs}, respectively),

whereas scenarios of cluster 2, 3, 8 and 9 show $p_{CSM,in}$ lower than p_0 and none of the scenarios exceed $(I/I_{cr})_{lim}$.

Figure 3.4 (left) collects each $t_{LOFA,C1,i}$ $(i = 1, \dots , N_{train})$, which is the time when control system C1 detects a LOFA in the *i-th* scenario, for all the N_{train} scenarios according to their belonging cluster. This event may occur during one of the $Q = 5$ phases of a single pulse of current (Savoldi et al., 2014), represented in Figure 2.11. Instead, a matrix $\bar{\bar{\mathcal{L}}}[C, Q]$ containing information of LOFA occurrence for each *c-th* cluster $(c = 1, \dots , C)$ at each *q-th* time interval $(q = 1, \dots , Q)$ is built in Figure 3.4 (right). The generic element $\mathcal{L}_{cq} = 1$, if there is at least one $t_{LOFA,C1,i}$ at the *c-th* cluster during the *q-th* phase, otherwise $\mathcal{L}_{cq} = 0$. Figure 3.4(right) shows the map with points where $\mathcal{L}_{cq} = 1$.
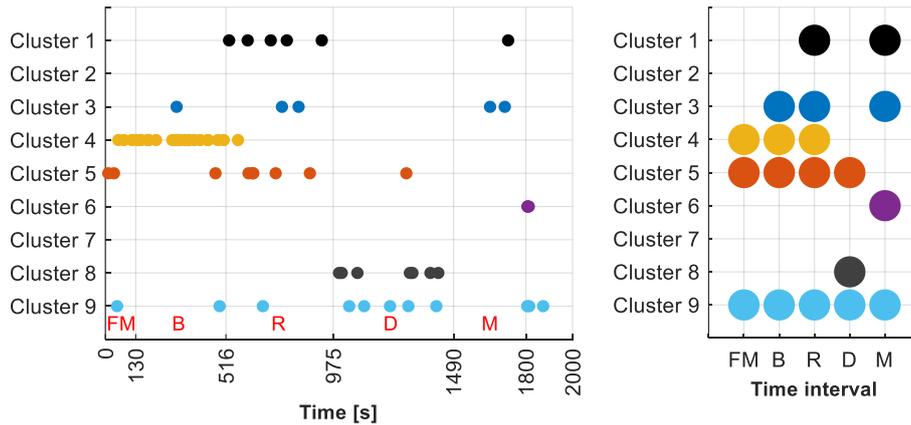
Figure 3.4 Exact times when LOFA occurs in the 83 (clustered) training scenarios (left); map of LOFA occurrence in each pulse phase for each cluster (right)

It can be seen that in the scenarios of cluster 4, LOFA occurs mostly during the early phase of the pulse of current (FM, B, R phases), where AC losses in the CSM are significative, making $p_{CSM,in}$ and T_{hs} reach the largest values, as pointed out before. On the other hand, no LOFAs occur in scenarios of clusters 2 and 7, despite that the prototypical component failures (i.e., the list of the components failures that occurs in the majority of transients belonging to each cluster) differ between clusters 2 and 7 (only CP failure for cluster 7 vs CP, CV, BV and SV for cluster 2), as it can be seen in Figure 3.5.
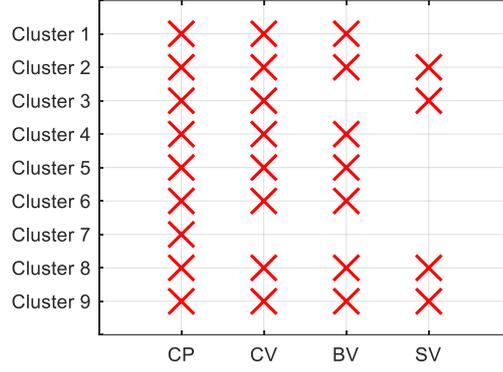
Figure 3.5 Map of prototypical failures

A matrix $\bar{\bar{\mathcal{F}}}[C, E = 4]$ is built from Figure 3.5 and each generic element $\mathcal{F}_{ce}$ is referred to the *c-th* cluster for the *e-th* component ($e = 1, \dots, E$): the generic element $\mathcal{F}_{ce} = 1$, if the *e-th* component is a prototypical failure of the *c-th* cluster, otherwise $\mathcal{F}_{ce} = 0$.

It is important to notice that failure of the CP is present in all clusters and failures of the CV and the BV in most of them (except clusters 3 and 7). This highlights the challenging identification of the component failures leading to LOFA (i.e., the LOFA precursors) by mining out information only from Figure 3.5. In what follows, we show an approach for an extensive and automatic LOFA precursors identification, to be applied on-line for promptly characterizing new scenarios evolutions, not included within the $N_{train} = 83$ transients used for training (i.e., building) the hereafter described approach.

3.3 The On-line Supervised Spectral Clustering

An On-line Supervised Spectral Clustering (OSSC) method, trained with the available $N_{train} = 83$ scenarios described in Section 3.2, is proposed for identifying the LOFA components failures responsible for the LOFA triggering, for any *j-th* scenario $y_j^k(t)$ of the remaining $10^8 - 83$ scenarios. As well as each $y_i^k(t)$ for $i = 1, 2, \dots, N_{train}$, $y_j^k(t)$ consists in $N_k = 3$ trajectories, $k = 1, 2, 3$ ($p_{CSM,in}$, T_{hs} and I/I_{cr}, respectively) and $j = 1, 2, \dots, N_{test}$, but, contrarily to $y_i^k(t)$, it results

from the simulation of the cooling circuit behaviour under MVL conditions that were not considered among the set of N_{train} scenarios.

The OSSC proceeds as follows (further details are reported in Appendix A), for each *j-th* scenario (the flowchart is sketched in Figure 3.10):

Step 1: The *k-th* trajectory $y_j^k(t)$ is recorded every $\Delta t = 0.01s$ time step from 0s to 3600s, corresponding to the length of two consecutive current pulses, so $L = 360001$ points for each *k-th* variable are saved and any y_{jl}^k $(l = 1,2,...,L)$ corresponds to the value of the *k-th* variable of the *j-th* scenario at the *l-th* time. Each $y_j^k(t)$ trajectory has the same discretization of $y_i^k(t)$ trajectory and $\bar{\bar{Y}}^k[N_{train}, L]$ matrix at *i-th* row and *l-th* column contains the value y_{il}^k of the *k-th* variable of the *i-th* training scenario at the *l-th* time point.

Step 2: Each y_{il}^k $(i = 1,2,...,N_{train}; l = 1,2,...,L)$ and each y_{jl}^k $(l = 1,2,...,L)$ are normalized as in Eq.(3.1) and in Eq.(A.1) (Appendix A):

$$y_{n,jl}^k = 0.2 + 0.6 \cdot \frac{y_{jl}^k - min(\bar{\bar{Y}}^k)}{max(\bar{\bar{Y}}^k) - min(\bar{\bar{Y}}^k)}, \quad k = 1,...,N_k \qquad (3.1)$$

It is worth mentioning that, if y_{jl}^k overcomes the maximum (or the minimum) value in $\bar{\bar{Y}}^k$, $y_{n,jl}^k$ may not lie in 0.2-0.8.

Step 3: The Euclidean pointwise distance $\delta_{l,ji}$ between the *j-th* scenario and the *i-th* training scenario $(i = 1,2,...,N_{train})$, at *l-th* time is calculated as in Eq.(3.2):

$$\delta_{l,ji} = \sum_{k=1}^{Z} \sum_{p=1}^{l} |y_{n,jp}^k - y_{n,ip}^k|, \quad i = 1,2,...,N_{train} \quad and \quad l = 1,2,...,L \quad (3.2)$$

Step 4: The similarity vector $\bar{W}_{l,j}[1, N_{train}]$ is built at each *l-th* time step, whose generic element $w_{l,ji}$ is given in Eq.(3.3):

$$w_{l,ji} = e^{-F \cdot \delta_{l,ji}^2} \quad with \ F = 1.7 \cdot 10^{-9} \ \text{(Bellaera et al., 2019)} \qquad (3.3)$$

The higher $w_{l,ji}$, the higher the similarity between the *j-th* testing scenario and the *i-th* training scenario until the *l-th* time step.

Step 5: The row vector $\bar{U}_{l,j}[1,C]$ is calculated projecting $\bar{W}_{l,j}$ in the eigenspace employing Eq.(B.8) (see Appendix B for proof). Afterward, it is normalized determining $\bar{T}_{l,j}[1,C]$, whose generic element $t_{l,jc}$ is given by Eq.(3.4):

$$t_{l,jc} = \frac{u_{j,jc}}{\sqrt{\sum_{c=1}^{C} u_{j,jc}^2}}, \quad c = 1,2,\ldots,C \tag{3.4}$$

Step 6: Each $M_{l,cj}$ membership of the *j-th* scenario at the *l-th* time step to the *c-th* cluster is calculated as in Eq.(3.5) (which is obtained from Eq.(A.8) of the FMC algorithm):

$$M_{l,cj} = \left[\sum_{\varsigma=1}^{C} \left(\frac{\|\bar{T}_{l,j} - \bar{\mathcal{A}}_c\|}{\|\bar{T}_{l,j} - \bar{\mathcal{A}}_\varsigma\|} \right)^{\frac{2}{\rho-1}} \right]^{-1}, \quad c = 1,2,3,\ldots,C \tag{3.5}$$

where $\bar{\mathcal{A}}_c[1,C]$ $(c = 1,2,\ldots,C)$ contains the eigenspace coordinates of the prototypical transient of the *c-th* cluster and $\rho = 2$ is the fuzzy partition exponent (Bezdec, 1981). The membership $M_{l,cj}$ measures the "degree" with which the *j-th* (test) scenario at the *l-th* time step "belongs" to the *c-th* cluster. Figure 3.6 and Figure 3.7 show the membership trends for a scenario with no failures (hereafter referred to as $j = 0$) and for a scenario with the complete closure of the CV1 at 623s, respectively: these two scenarios belong to cluster 7 and cluster 5, respectively, because $M_{l,7j}$ in Figure 3.7 and $M_{l,5j}$ in Figure 3.6 rapidly rise and reach values close to 1, whereas the other memberships gradually drop to 0.
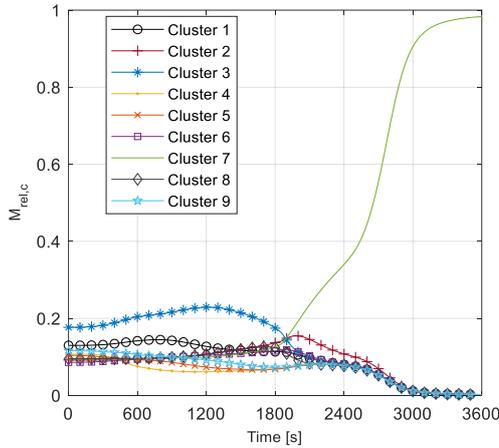
Figure 3.6 Membership trends for a scenario at nominal conditions with no failures
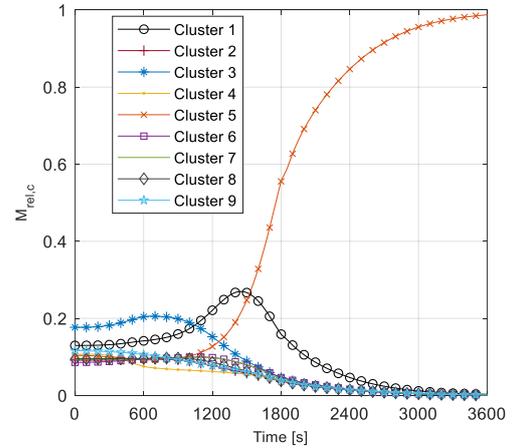
Figure 3.7 Membership trends for a scenario "complete closure of CV1 at 623s" (and $t_{LOFA,C1,j} = 627.14s$)

Step 7: Calculate the pointwise difference between $M_{l,cj}$ and $M_{l,c0}$ resulting in $M_{rel,l,cj}$ (shown by way of example in Figure 3.8 for the scenario "complete closure of CV1 at 623s") as in Eq.(3.6):

$$M_{rel,l,cj} = M_{l,cj} - M_{l,c0} \ , \qquad c = 1,2,\dots,C \qquad (3.6)$$

The difference (3.6) serves the purpose of "removing" from the membership trend of the *j-th* test transient to cluster *c* the "background" contribution of a "standard" scenario at nominal condition with no failures.

Step 8: Calculate $V_{rel,l,cj}$ with Eq.(3.7), i.e., a discrete estimator of the derivative of the membership $M_{l,cj}$ with respect to the *l-th* time (shown in Figure 3.9 for the scenario "complete closure of CV1 at 623s"):

$$V_{rel,l,cj} = \begin{cases} 0 & if \ l = 1 \\ \dfrac{M_{rel,l,cj} - M_{rel,(l-1),cj}}{\Delta t} & if \ l \neq 1 \end{cases} , \qquad c = 1,2,\dots,C \qquad (3.7)$$

It is evident from Figure 3.8 and Figure 3.9 that $M_{rel,l,cj}$ and $V_{rel,l,cj}$ start differing from "0" at 623s after the closure of CV1, because its failure deviates the system from its nominal behaviour (i.e., from the scenario with no failures): in particular, the failure of CV1 generates an accidental scenario with an initial affinity to cluster 1 and 5, as testified by the simultaneous increase in the values of $M_{rel,l,1j}$, $M_{rel,l,5j}$, $V_{rel,l,1j}$ and $V_{rel,l,5j}$; however, the increase in $M_{rel,l,5j}$ and $V_{rel,l,5j}$ becomes dominant at about 1450s, correctly and clearly showing that the scenario belongs to cluster 5.
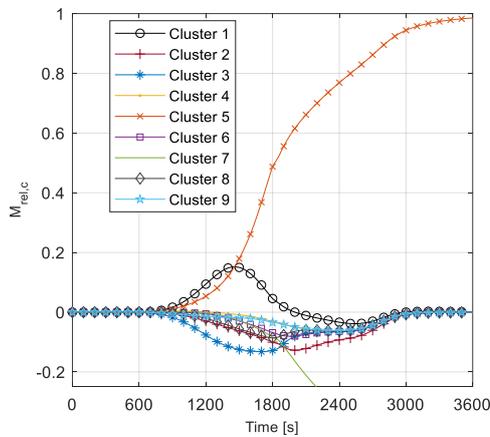
Figure 3.8 $M_{rel,l,cj}$ trends for scenario "complete closure of CV1 at 623s"
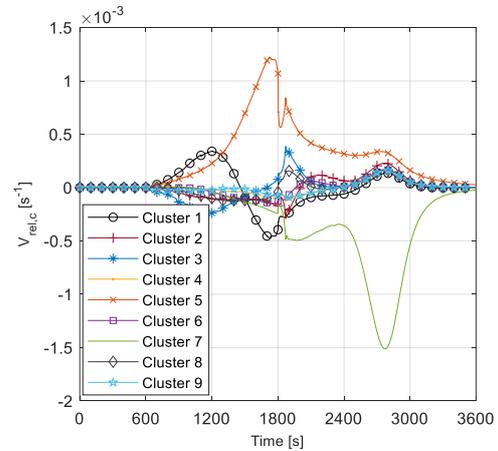
Figure 3.9 $V_{rel,l,cj}$ trends for scenario "complete closure of CV1 at 623s"
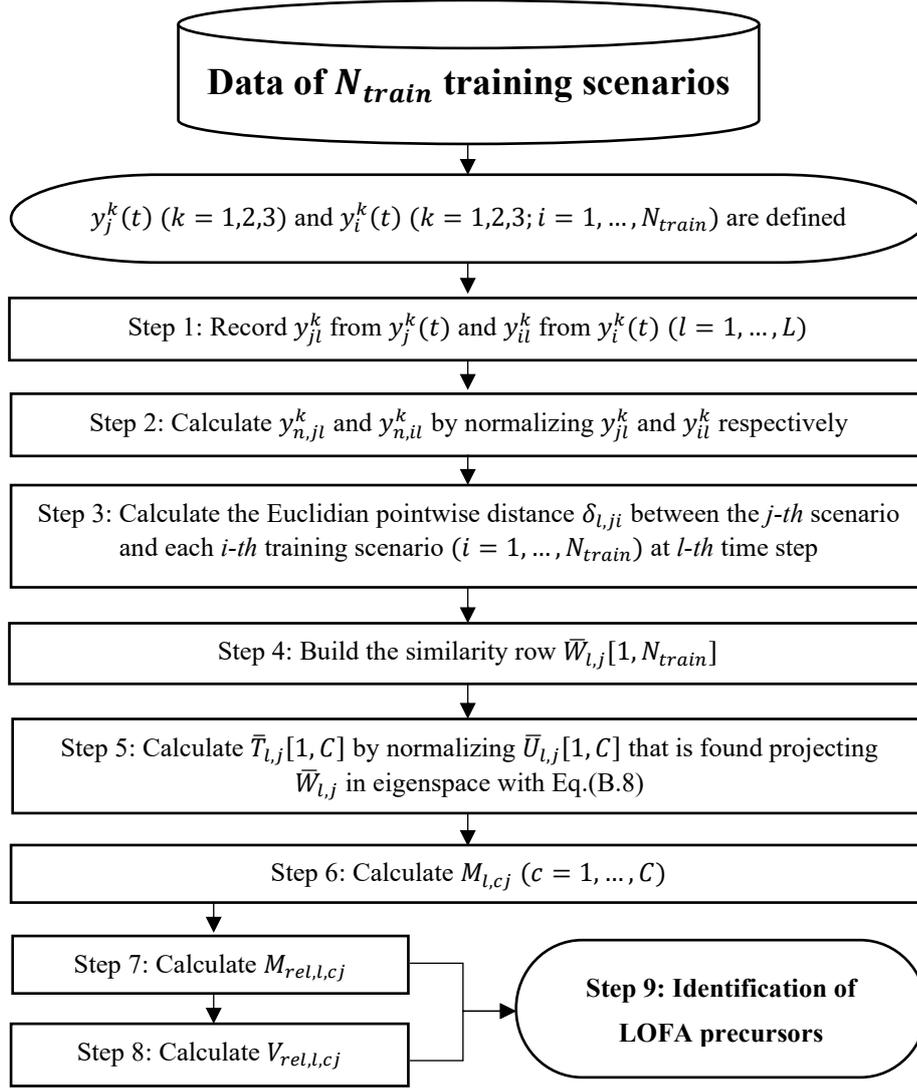
Figure 3.10 Flow chart of the OSSC procedure

Step 9: Identify LOFA precursors as follows.

Step 9a: Compare $V_{rel,l,cj}$ $[c = 1, ..., C]$ with $V_{lim,LOFA,l}$, following the pseudo code in Figure 3.11. In extreme synthesis, if at least two values of $V_{rel,l,cj}$ overcome the threshold $V_{lim,LOFA,l}$ (see Figure 3.12 below) at time l, and if a LOFA can occur in the corresponding clusters (according to the map of Figure 3.4(right)), the algorithm identifies the LOFA precursors.

```
At l-th time
        Calculate $V_{1st} = \max_{c}(V_{rel,l,cj})$;
        Calculate $c_{1st} = \arg\left(\max_{c}(V_{rel,l,cj})\right)$;
        Calculate $V_{2nd} = \max_{c \neq c_{1st}}(V_{rel,l,cj})$;
        Calculate $c_{2nd} = \arg\left(\max_{c \neq c_{1st}}(V_{rel,l,cj})\right)$;
        $Flag_{LOFA} = 0$;
        If $(V_{1st} > V_{lim,LOFA,l} \ \& \ V_{2nd} > V_{lim,LOFA,l})$
                Find q-th current phase that corresponds to l-th time
                $Flag_{LOFA} = \mathcal{L}_{c_{1st}q} * \mathcal{L}_{c_{2nd}q}$; % $\mathcal{L}_{cq} = \{0,1\}$ (see Figure 3.4 (right))
        End
        If $Flag_{LOFA} = 1$
                LOFA precursor is identified;
        Else
                LOFA precursor does not exist;
        End
```

Figure 3.11 Pseudo code for $V_{rel,l,cj}$ and $V_{lim,LOFA,l}$

The trend of $V_{lim,LOFA,l}$ is assumed to be a monotonic increasing piecewise function that is calculated relying on the information stored in the N_{train} scenarios, following the pseudo-code of Figure 3.12. The trend of $V_{lim,LOFA,l}$ is initially defined using a discrete set of points obtained from the N_{train} scenarios and joined together to build a stepwise function monotonically increasing.

```
For each i-th scenario ($i = 1, ..., N_{train}$)
        If LOFA occurs
                $t_{lim,i} = \text{round}\left((t_{last,Fail,i} + t_{LOFA,C1,i})/2\right)$;
        Else
                $t_{lim,i} = NaN$;
        End
End
$V_{lim,LOFA,l}$ DEFINITION:
Define $V_{lim,LOFA,1} = 0$;
For $l = 2:1:L$
        Find i such that l-th time $= t_{lim,i}$ ($i = 1, ..., N_{train}$)
        If i exists
                Calculate $c_{1st} = \arg\left(\max_{c}(V_{rel,l,ci})\right)$;
                Calculate $V_{lim,i} = \max_{c \neq c_{1st}}(V_{rel,l,ci})$;
                $V_{lim,LOFA,l} = V_{lim,i}$;
        Else
                $V_{lim,LOFA,l} = V_{lim,LOFA,(l-1)}$;
        End
End
$V_{lim,LOFA,l}$ REVISION:
For $p = L:-1:1$
        For $l = 1:1:(p-1)$
                If $V_{lim,LOFA,l} > V_{lim,LOFA,p}$
                        $V_{lim,LOFA,l} = V_{lim,LOFA,p}$;
                End
        End
End
```

Figure 3.12 $V_{lim,LOFA,l}$ calculation procedure

where $t_{last,Fail,i}$ is the time when the last failure before $t_{LOFA,C1,i}$ occurs. Figure 3.13 reports results of each step of procedure in Figure 3.12.
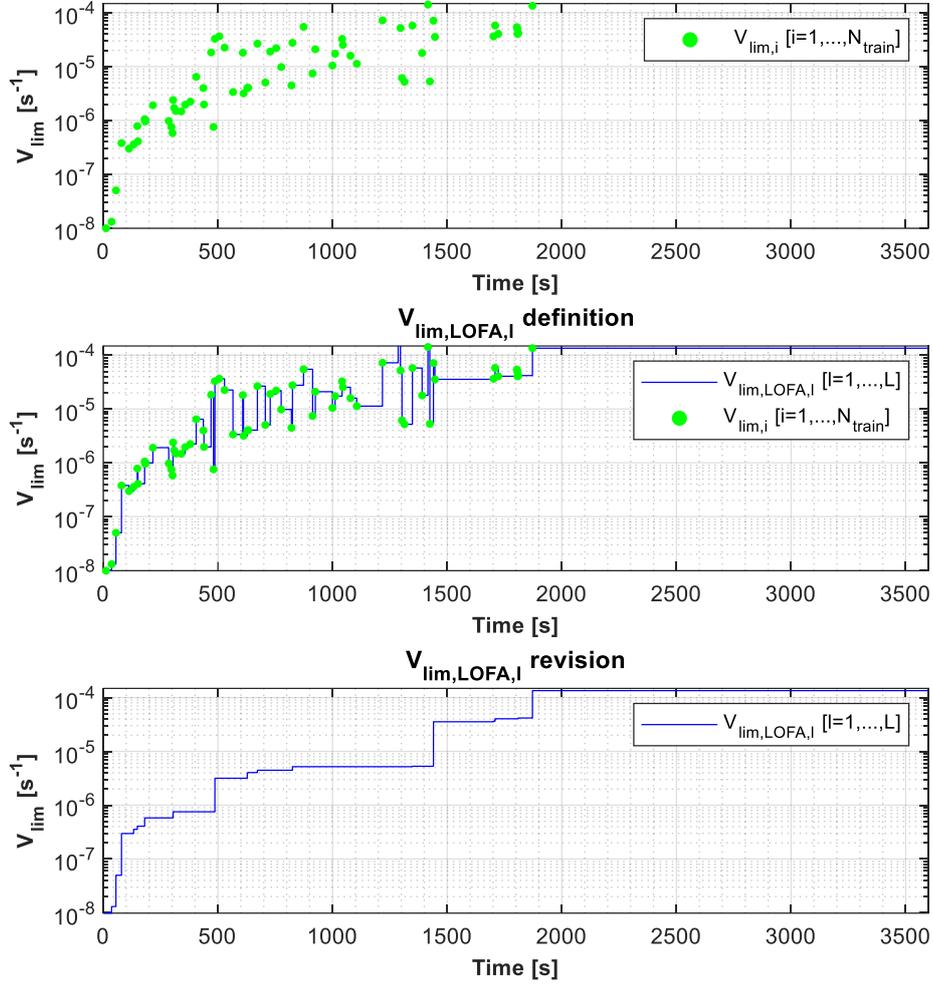
Figure 3.13 $V_{lim,LOFA,l}$ calculation results

Step 9b: Compare $M_{rel,l,cj}$ $(c = 1, ..., C)$ to the threshold $M_{lim,FAIL,l}$ (3.8), following the pseudo code in Figure 3.14. In extreme synthesis, if all the values of $M_{rel,l,cj}$ that exceeds $M_{lim,FAIL,l}$ at *l-th* time step presents the *e-th* component as prototypical failure, according to the map of Figure 3.5, the algorithm identifies the failure of the *e-th* component as a LOFA precursor.

```
At l-th time considering an e-th component
        Flag_{FAIL,e} = 1;
        Count_{FAIL,e} = 0;
        For c = 1:1:C
                If M_{rel,l,cj} > M_{lim,FAIL,l}
                        Flag_{FAIL,e} = Flag_{FAIL,e} * F_{ce};   % F_{ce} = {0,1}  (see Figure 3.5)
                        Count_{FAIL,e} = Count_{FAIL,e} + 1;
                End
        End
        If Flag_{FAIL,e} = 1 & Count_{FAIL,e} ≠ 0;
                e-th component is failed
        Else
                e-th component is not failed;
        End
```

Figure 3.14 Pseudo code for $M_{rel,l,cj}$ and $M_{lim,FAIL,l}$

$M_{lim,FAIL,l}$ is calculated as in Eq.(3.8):

$$M_{lim,FAIL.l} = S \cdot (l^{th}\ time) \quad with\ S = 5.56 \times 10^{-8}\ s^{-1} \tag{3.8}$$

It is worth mentioning that $M_{lim,FAIL,l}$ is assumed to be linearly dependent on time, because in δ_{ij} (A.2) linearly increases from $t = 0s$ to $t = t_{miss} = 3600s$ and it is used to calculate $M_{rel,l,cj}$. S is the value that maximises the number of training scenarios whose components failures are correctly identified as LOFA precursors, minimising at the same time the time delay between components failures and precursors identification.

3.4 Results

The proposed procedure is tested with respect to LOFA precursors identification for the SMCCC of Section 2, for which $N_{test} = 38$ scenarios, different from the $N_{train} = 83$ scenarios used to build the OSSC method of Section 3.3, have been simulated resorting to the 4C code.

As an example, we show the results with respect to the scenario "complete closure of CV1 at 623s", whose memberships are plotted in Figure 3.7 above. In Figure

3.15 a zoom of the values of each $M_{rel,l,cj}$ and $V_{rel,l,cj}$ ($c = 1, \ldots, C$) in the interval [600s,650s] (i.e., when CV1 incidentally fails at 623s) is shown.
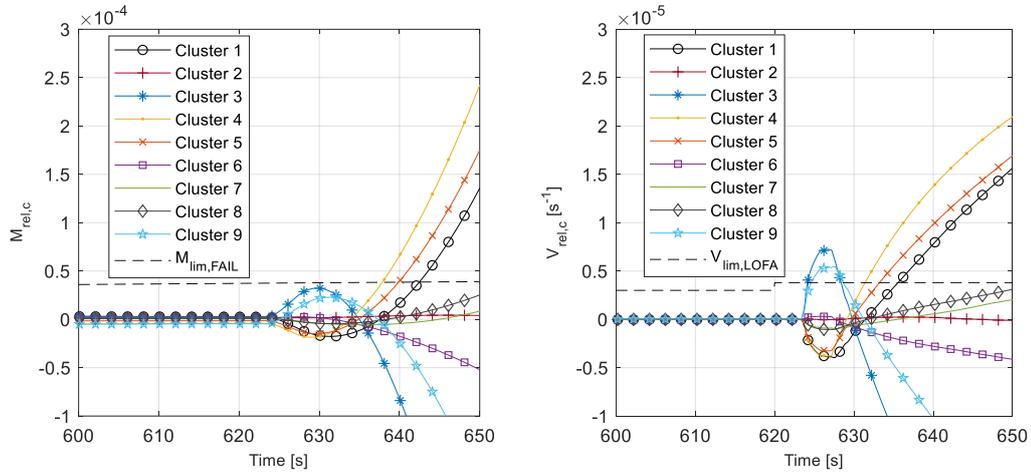
Figure 3.15 Zoom of $M_{rel,l,cj}$ (left) and $V_{rel,l,cj}$ (right) trends in the interval [600s-650s] for scenario "complete closure of CV1 at 623s"

It can be seen that $V_{rel,l,3j}$ and $V_{rel,l,9j}$ overcome $V_{lim,LOFA,l}$ at 625s (that is therefore taken as LOFA detection time and plotted with a cross in Figure 3.16) in the R phase. During this phase of the current pulse, as suggested in Figure 3.4, the component failures of the prototypical scenarios of clusters 3 and 9 might be responsible for the LOFA detection during this phase. However, no component is identified as "failed" by the algorithm at that time, because no values of $M_{rel,l,cj}$ have overcome $M_{lim,FAIL,l}$. On the other hand, $M_{lim,FAIL,l}$ is reached by $M_{rel,l,4j}$ at 637s, suggesting that component failures of the prototypical transient of cluster 4 (i.e., CP, CV and BV) are responsible (shadowed lines in Figure 3.16). This is also confirmed when $M_{rel,l,5j}$ and $M_{rel,l,1j}$ overcome $M_{lim,FAIL,l}$ (at 640s and 643s, respectively), since prototypical component failures of clusters 5 and 1 are still CP, CV and BV. In practice, the responsible component failures, i.e., the LOFA precursor CV, has been timely and correctly identified.
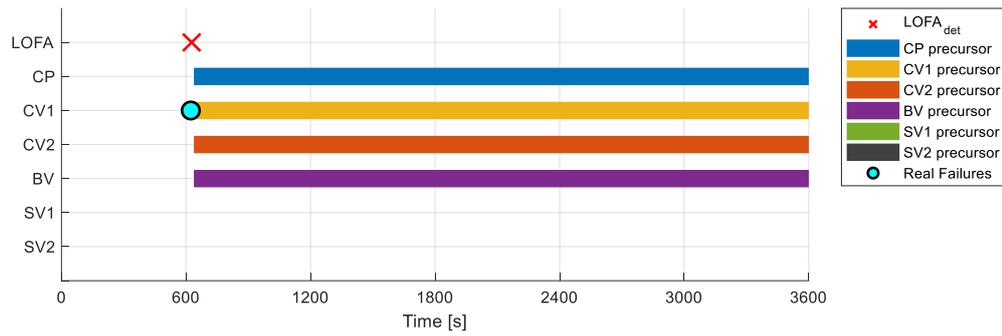
Figure 3.16 LOFA precursors identification for scenario "complete closure of CV1 at 623s"

In summary, in the present case the LOFA is detected 2s earlier than the actual $t_{LOFA,C1,j}$ whereas the LOFA precursor is identified 10s later than the real misfunctioning with high uncertainty on the failed component, because only a CV is actually failed, whereas CP and BV works correctly. In other words, the number of failed components is slightly overestimated.

In Table 3.1, the results of the extensive analysis on the $N_{test} = 38$ scenarios are summarized.

Table 3.1 Results on $N_{test} = 38$ scenarios

Scenarios with LOFA	*32*
LOFA predicted in advance	26
LOFA not predicted in advance	6
Scenarios with NO LOFA	*6*
Correct identification NO LOFA	2
False positive LOFA	4

Among these, 32 scenario entail a LOFA to occur, whereas 6 do not. For the former ones, LOFA is detected before $t_{LOFA,C1,j}$ in 26 scenarios and later in the other 6; however, in these last 6 scenarios the LOFA often occurs during the D phase, when no heat is produced by the CSM, and the CSM is not endangered. On the other hand, for the latter, in 2 scenarios no LOFA precursors are discovered, while in the other 4 LOFA is detected even though it does not occur (namely, "false positives"). Generally, LOFA is predicted in advance in most scenarios with a presence of

LOFA precursors, but there is a significant number of false positives in scenarios without LOFA precursors.

In Table 3.2, the results for the precursor identification of the 32 scenarios with LOFA are presented with respect to

- Correct precursor identification: the component is failed and correctly identified as precursor.
- False negative: the component is failed, but not identified as precursor.
- Correct identification of normal operation: the component is not failed along the scenario.
- False positive: the component is not failed, but wrongly identified as precursor.

Table 3.2 Results of the precursor identification approach for $N_{test} = 38$ scenarios

	Correct precursor identification	*False negative*	*Correct identification of normal operation*	*False positive*
CP	22	1	0	9
CV1	16	0	0	16
CV2	15	0	0	17
BV	12	4	1	15
SV1	1	1	17	13
SV2	4	0	18	10

It can be seen that most of the precursors are identified correctly by the OSSC algorithm, despite the large number of false positives, that, however, do not endanger the SMCCC, because conservatively overestimating the number of failed components.

4 Development of Kriging metamodels for improving the LOFA precursors identification algorithm

The dataset for LOFA precursors identification needs to be enriched with more simulations (i.e., with a larger number of exemplary *transients*), in order to generate more detailed maps (to be employed by the algorithm) and to possibly reduce the number of false positives found in Section 3.4. The information contained in these maps has to be "classified" according to the $C = 9$ clusters described in Section 3.2: in other words, new scenarios (i.e., new time-varying signals/outputs $y_i^k(t)$) must be assigned to one of the $C = 9$ clusters by means of the Supervised method of Appendix B (which employs Spectral Clustering, described in Appendix A). On the other hand, the generation of new scenarios by standard random sampling and their simulation by the long-running 4C code may entail prohibitive computational costs.

For this reason, Kriging metamodels are here employed as "surrogate" models able to mimic – at a *reduced computational cost* – the behaviour of the original, detailed 4C code (in other words, able to *quickly* reproduce/approximate the nonlinear relationship between the code inputs $\boldsymbol{X}$ and the code outputs $\boldsymbol{Y}$, described in Section 3.1). A generic metamodel $\mathcal{MM}$ is built using a so-called Design Of Experiment (DOE) (or *training set*), i.e., a set of examples/realizations $(\boldsymbol{X}_i, \boldsymbol{Y}_i)$ ($i = 1, \ldots, N_{krig}$) of the input-output relationship underlying the original 4C code. The procedure for constructing a metamodel that optimally interpolates/fits the training data is not reported here for brevity: the interested reader is referred to Appendix C for details. The choice of Kriging metamodels has been made for the following reasons: (i) their proven ability to approximate and reproduce *complex nonlinear functions* (also characterized by sudden, abrupt changes in their trend); (ii) their capability of providing an estimate of the *uncertainty* associated to their predictions on new, unknown inputs (Wang et al., 2007; Simpson et al., 2001).

The use of Kriging metamodels can be described in three steps. In the first, the Adaptive Kriging – Monte Carlo Sampling (AK-MCS) algorithm (Turati et al.,

2017 & 2018a) is employed to intelligently and adaptively enrich our training dataset with "interesting" scenarios in proximity of the system failure region (i.e., in proximity of system LOFA configurations), while reducing the number of calls to the original 4C code and the related computational burden (see Section 4.1). In the second step, the dataset thereby generated (constituted by $N_{krig} > N_{train} = 83$ scenarios and enriched in proximity of the failure configurations) is used to construct a Proper Orthogonal Decomposition (POD)-based Kriging metamodel. The main feature of this metamodel is that it is able to simulate *transients* (i.e., *time-varying signals*): thus, it is here employed for approximate/reproduce the behaviour of the 4C code outputs $y_i^k(t)$ for *new* inputs configurations (i.e., accident scenarios), without employing the original, long-running 4C code. In this way, we can generate a very large amount ($N_{data} \gg N_{train} = 83$) of new scenarios, with a sharp decrease in the computational cost with respect to the 4C code. These new "approximate" (metamodel-based) transients are added to the LOFA precursor identification algorithm of Chapter 3, in order to refine the maps of Figure 3.4 and Figure 3.5 (Section 4.2) . Finally, the LOFA precursor identification algorithm is modified to include these new maps (Section 4.3) and the results of its application to N_{test} scenarios are shown (Section 4.4).

4.1 The AK-MCS algorithm

In this part, the AK-MCS algorithm (Turati et al., 2017 & 2018) is tailored to explore the state-space of the component failures of the SMCCC: in extreme synthesis, the idea is to intelligently drive/push the exploration towards the system configurations of our interest (in this case, the failure configurations leading to a LOFA): this allows enriching the number of examples of system behaviour in these regions, while intelligently allocating the computational resources (i.e., the number of "heavy" simulations) This algorithm is applied to each *k-th* output (i.e., safety-critical) variable of interest and a proper DOE must be accordingly defined.

In particular, with reference to the system safety criteria described in Section 2.3, we are looking for the maximum value of each $y_i^k(t)$ ($k = 1, ..., N_k$) along the

transient (i.e., over time): thus, for each input configuration $\boldsymbol{X}_i$ the recorded output is $\boldsymbol{Y}_i = [(y_i^1(t))_{max}, (y_i^2(t))_{max}, (y_i^3(t))_{max}] = [\mathcal{Y}_i^1, \mathcal{Y}_i^2, \mathcal{Y}_i^3]$. These output values need to be compared with the safety thresholds $\boldsymbol{Y}_{thr} = [\mathcal{Y}_{thr}^1, \mathcal{Y}_{thr}^2, \mathcal{Y}_{thr}^3] = [p_{lim} = 1.8\ MPa, T_{cs} = 7.3\ K, (I/I_{cr})_{lim} = 0.5]$ to understand whether that scenario leads to system failure or to a "safe" state. The DOE (employed for the construction of the Kriging metamodel) includes all the inputs $\bar{\boldsymbol{X}} = \{\boldsymbol{X}_1, \boldsymbol{X}_2, \dots, \boldsymbol{X}_{N_{krig}}\}$ and the corresponding outputs $\bar{\boldsymbol{Y}} = \{\boldsymbol{Y}_1, \boldsymbol{Y}_2, \dots, \boldsymbol{Y}_{N_{krig}}\}$. However, more scenarios should be included in the DOE to improve the accuracy of the meta-models that we need to build. To this aim, an AK-MCS procedure is adopted, exploiting an adaptive procedure shown in the flow chart of Figure 4.1 (Turati et al., 2018).
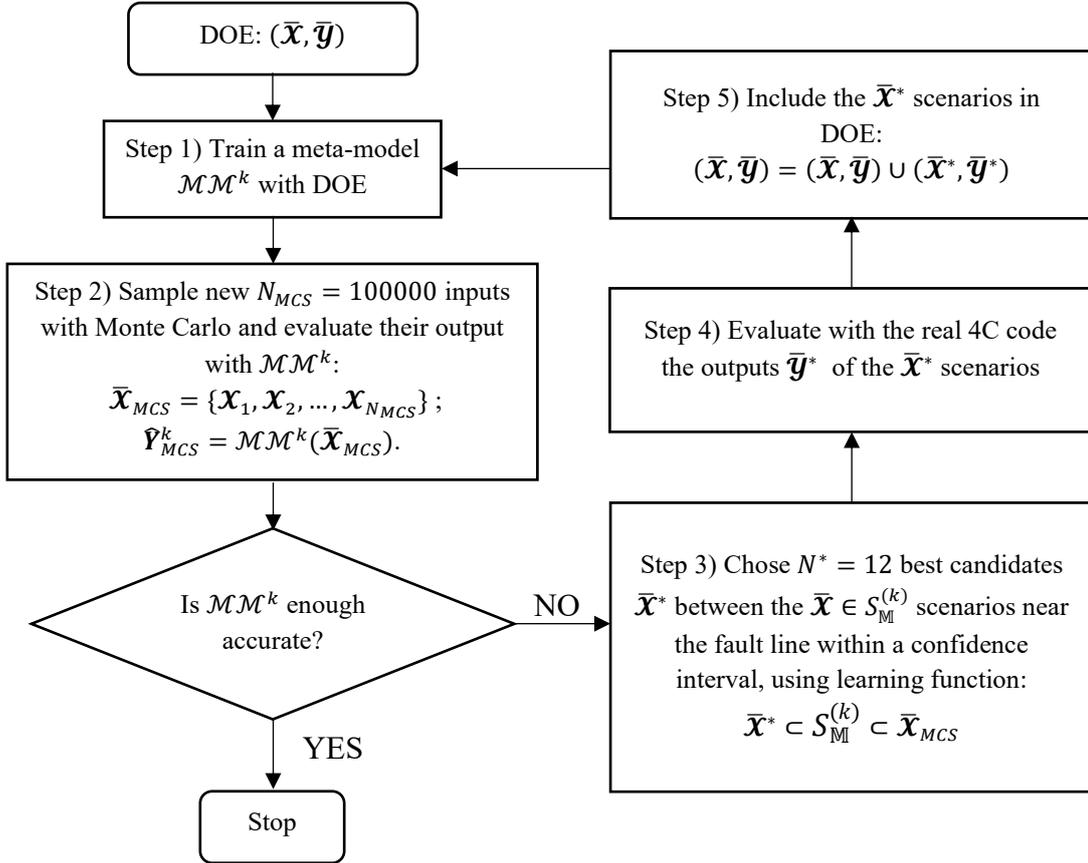
Figure 4.1 Flowchart of a sequential adaptive training strategy (AK-MCS)

Step 1) Each $\mathcal{MM}^k$ meta-model is trained with the DOE, resorting to UQLab Toolbox of Matlab, and the meta-model adopted is the Kriging one, described in Appendix C (Lataniotis et al., 2015). Considering a generic input $\boldsymbol{X}$ (in this case, a

randomly sampled combination of components failure times and magnitudes), the properly trained "surrogate" model will let us to predict – in a negligible computational time - the corresponding *k-th* element of the output $\hat{Y}_{MCS}^k = \mathcal{MM}^k(\boldsymbol{X})$. The parameters of these metamodels are "tuned" according to the guidelines given in (Turati et al., 2017) (see also Appendix C for details). In particular, ordinary Kriging metamodels are developed, which means that the trend basis $\boldsymbol{\beta}_k{}^T \boldsymbol{\hbar}(\boldsymbol{X})$ is considered constant $\left[\boldsymbol{\beta}_k{}^T \boldsymbol{\hbar}(\boldsymbol{X}) = \beta_{k,1} \hbar_1(\boldsymbol{X}) = \beta_{k,0},\right.$ with $\hbar_1(\boldsymbol{X}) = 1\right]$. The correlation function $\mathcal{R}(\boldsymbol{X}, \boldsymbol{X}'; \boldsymbol{\theta}^k)$ used in the model is "ellipsoidal" and "anisotropic" like in Eq.(4.1):

$$\mathcal{R}(\boldsymbol{X}, \boldsymbol{X}'; \boldsymbol{\theta}^k) = \mathcal{R}(\xi^k) \tag{4.1}$$

$$with \quad \xi(\boldsymbol{X}, \boldsymbol{X}'; \boldsymbol{\theta}^k) = \sqrt{\sum_{m=1}^{M} \left(\frac{\mathcal{X}_m - \mathcal{X}'_m}{\theta_m^k}\right)^2} \tag{4.2}$$

where ξ is an ellipsoidal function.

Precisely, a "3/2 Matérn" correlation function (4.3) is used in the Gaussian Process:

$$\mathcal{R}(\xi) = \left(1 + \xi\sqrt{3}\right)e^{-\xi\sqrt{3}} \tag{4.3}$$

A Kriging optimization method is needed to calculate the hyperparameters $\boldsymbol{\theta}^k$ necessary for the definition of σ_k^2. For this purpose, the K-fold cross validation embedding the Hybrid Genetic Algorithm (HGA) is adopted to find the minimum value of the optimization function (4.4):

$$\boldsymbol{\theta}^k = \arg\min_{\mathcal{D}_\theta} \sum_{i=1}^{N_{krig}} \left(\mathcal{MM}^k(\boldsymbol{X}_i) - \mu_{\hat{Y}^k,(-i)}(\boldsymbol{X}_i)\right)^2 \tag{4.4}$$

where $\mu_{\hat{Y}^k,(-i)}(\boldsymbol{X}_i)$ is the mean value at the point $\boldsymbol{X}_i$ of the Kriging predictor built with all the DOE excepting for the couple $(\boldsymbol{X}_i, \boldsymbol{Y}_i)$.

Once the HGA find the optimum value of each θ_m^k ($m = 1,2, \dots, M$) in the range $[0.001,10]$, the variance σ_k^2 is defined as in Eq.(4.5):

$$\sigma_k^2 = \frac{1}{N_{krig}} \sum_{i=1}^{N_{krig}} \frac{\left(\mathcal{MM}^k(\boldsymbol{X}_i) - \mu_{\hat{Y}^k,(-i)}(\boldsymbol{X}_i)\right)^2}{\sigma_{\hat{Y}^k,(-i)}^2(\boldsymbol{X}_i)} \tag{4.5}$$

where $\sigma_{\hat{Y}^k,(-i)}^2(\boldsymbol{X}_i)$ is the variance at the point $\boldsymbol{X}_i$ of the Kriging predictor built with all the DOE excepting for the couple $(\boldsymbol{X}_i, \boldsymbol{Y}_i)$.

For each *k-th* output, the meta-model $\mathcal{MM}^k$ is trained $N_{iter} = 100$ times and the one with the lowest Leave-One-Out (LOO) error will be the $\mathcal{MM}^k$ chosen to mimic the behaviour of the *k-th* output. The LOO error is evaluated with Eq.(4.6):

$$LOO = \frac{1}{N_{krig}} \sum_{i=1}^{N_{krig}} \frac{\left(\mathcal{MM}^k(\boldsymbol{X}_i) - \mu_{\hat{Y},(-i)}(\boldsymbol{X}_i)\right)^2}{\sigma^2} \tag{4.6}$$

Step 2) Once the metamodel is trained, new $N_{MCS} = 100000$ (input) scenarios (different from the N_{krig} ones) are generated by resorting to standard Monte Carlo Sampling (MCS).

Once the $\overline{\boldsymbol{X}}_{MCS} = \{\boldsymbol{X}_1, \boldsymbol{X}_2, \ldots, \boldsymbol{X}_{N_{MCS}}\}$ inputs are defined, their corresponding predictions will be $\hat{\boldsymbol{Y}}^k_{MCS}(\overline{\boldsymbol{X}}_{MCS}) = \mathcal{MM}^k(\overline{\boldsymbol{X}}_{MCS}) = \{\mathcal{MM}^k(\boldsymbol{X}_1), \ldots, \mathcal{MM}^k(\boldsymbol{X}_{N_{MCS}})\}$, to which the mean Kriging values $\boldsymbol{\mu}_{\hat{Y}^k}(\overline{\boldsymbol{X}}_{MCS}) = \{\mu_{\hat{Y}^k}(\boldsymbol{X}_1), \ldots, \mu_{\hat{Y}^k}(\boldsymbol{X}_{N_{MCS}})\}$ and the Kriging variances $\boldsymbol{\sigma}_{\hat{Y}^k}^2(\overline{\boldsymbol{X}}_{MCS}) = \{\sigma_{\hat{Y}^k}(\boldsymbol{X}_1), \ldots, \sigma_{\hat{Y}^k}(\boldsymbol{X}_{N_{MCS}})\}$ are associated. Notice that these evaluations (i.e., approximations of the code outputs) are obtained by the metamodel, so at reduced computational cost.

Step 3) The N_{MCS} scenarios are analyzed to find the ones that lie "in proximity" of the system failure region , which is identified by the threshold in Eq.(4.7) (Schöbi et al., 2017):

$$\mu_{\hat{Y}^k}(\boldsymbol{X}) = \mathcal{Y}_{thr}^{(k)} \tag{4.7}$$

where $\mu_{\hat{Y}^k}(\boldsymbol{X})$ is the mean value of Kriging predictor $\mathcal{MM}^k(\boldsymbol{X})$ for input $\boldsymbol{X}$ (whose Kriging variance is $\sigma_{\hat{Y}^k}^2(\boldsymbol{X})$). The area that lies "close" to the system failure region is indicated as $S_{\mathbb{M}}$ and is defined as follows by means of a confidence interval.

The upper boundary of the confidence interval of the failure line is

$$\mu_{\hat{Y}^k}(\boldsymbol{X}) - \varepsilon \cdot \sigma_{\hat{Y}^k}(\boldsymbol{X}) = \mathcal{Y}_{thr}^k \tag{4.8}$$

and the lower bound is

$$\mu_{\hat{Y}^k}(\boldsymbol{X}) + \varepsilon \cdot \sigma_{\hat{Y}^k}(\boldsymbol{X}) = \mathcal{Y}_{thr}^k \tag{4.9}$$

where ε is the confidence level set to 1.96 (according to the properties of the Normal distribution): actually, if $\varepsilon = 1.96$, there is a probability of 97.5% that $\mathcal{Y}^k \in [\mu_{\hat{Y}^k}(\boldsymbol{X}) - \varepsilon \cdot \sigma_{\hat{Y}^k}(\boldsymbol{X}), \mu_{\hat{Y}^k}(\boldsymbol{X}) + \varepsilon \cdot \sigma_{\hat{Y}^k}(\boldsymbol{X})]$ with $\mathcal{Y}^k$ being the *k-th* output evaluated with the real code for a $\boldsymbol{X}$ input (Schöbi et al., 2017).

Considering the ensemble of all the inputs $\bar{\boldsymbol{X}}_{MCS}$, the ones that belong to $S_{\mathbb{M}}^{(k)}$ are expressed in Eq.(4.10):

$$S_{\mathbb{M}}^{(k)} \equiv \left\{ \boldsymbol{X} : \left(\boldsymbol{X} \notin S_{f+}^{(k)} \right) \cap \left(\boldsymbol{X} \in S_{f-}^{(k)} \right) \right\} \tag{4.10}$$

with

$$S_{f+}^{(k)} \equiv \left\{ \boldsymbol{X} \in \bar{\boldsymbol{X}}_{MCS} : \mu_{\hat{Y}^k}(\boldsymbol{X}) - \varepsilon \cdot \sigma_{\hat{Y}^k}(\boldsymbol{X}) \geq \mathcal{Y}_{thr}^k \right\} \tag{4.11}$$

and

$$S_{f-}^{(k)} \equiv \left\{ \boldsymbol{X} \in \bar{\boldsymbol{X}}_{MCS} : \mu_{\hat{Y}^k}(\boldsymbol{X}) + \varepsilon \cdot \sigma_{\hat{Y}^k}(\boldsymbol{X}) \geq \mathcal{Y}_{thr}^k \right\}. \tag{4.12}$$

The sets defined in (4.11) and (4.12) contain the inputs $\bar{\boldsymbol{X}}_{MCS}$ with a mean Kriging value (i.e., output) exceeding the upper and lower boundaries of the confidence interval of the failure line, respectively.

Once $S_{\mathbb{M}}^{(k)}$ is defined, a set of $N^* = 12$ (value between M and $2M$) input configurations belonging to $S_{\mathbb{M}}^{(k)}$ are identified and selected to be added to the current DOE (these new configurations will *update* and *enrich* the current DOE with "interesting" scenarios that will likely lead the system to failure). To this aim, the Learning function $\mathcal{U}^k(\boldsymbol{X})$ shown in Eq.(4.13) is used:

$$\mathcal{U}^k(\boldsymbol{X}) = \frac{\left| \mu_{\hat{Y}^k}(\boldsymbol{X}) - \mathcal{Y}_{thr}^k \right|}{\sigma_{\hat{Y}^k}(\boldsymbol{X})} \tag{4.13}$$

The main idea is the following: the lower is the value of the Learning function $\mathcal{U}^k(\boldsymbol{X})$, the more "interesting" is the system configuration $\boldsymbol{X}$ to add to the current DOE. Actually, a low value of the Learning function means that: (i) the system configuration $\boldsymbol{X}$ is close to the failure region (i.e., the system response $\mu_{\hat{Y}^k}(\boldsymbol{X})$ is close to the failure threshold $\mathcal{Y}_{thr}^k$); and/or (ii) the uncertainty $\sigma_{\hat{Y}^k}(\boldsymbol{X})$ associated to the Kriging prediction $\mu_{\hat{Y}^k}(\boldsymbol{X})$ is high (this is typically due to the scarcity of training examples around $\boldsymbol{X}$, which prevents the metamodel from producing precise estimates: in this view, adding new training examples in that area would improve the precision of the metamodel). In addition to this main driving criterion given by the Learning function (4.13), we would like the $N^* = 12$ additional configurations to be "evenly distributed" in the confidence region $S_{\mathbb{M}}^{(k)}$ around the failure line.

Step 4) The resulting $N^* = 12$ input configurations $\bar{\boldsymbol{X}}^*$ are simulated by the original 4C code, finding the new corresponding outputs $\bar{\boldsymbol{\mathcal{Y}}}^*$.

Step 5) The new (input-output) training examples $(\bar{\boldsymbol{X}}^*, \bar{\boldsymbol{\mathcal{Y}}}^*)$ are added in the current DOE.

After Step 5, Step 1 and 2 are repeated with a larger and richer DOE and, if the $\mathcal{MM}^k$ meta-model is still not accurate enough, the AK-MCS continues to find new scenarios to include in the DOE repeating steps 3, 4 and 5; otherwise, the algorithm is stopped.

4.1.1 Application of the AK-MCS to one of the safety-critical variables

For the sake of illustration, the results of the AK-MCS algorithm described above are shown only for the output $(I/I_{CR})_{max}(k = 3)$. Indeed, from the AK-MCS iterations it turns out that $(I/I_{CR})_{max}(k = 3)$ is the most safety-critical variable, whereas $p_{CSM,in,max}$ $(k = 1)$ and $T_{HS,max}$ $(k = 2)$ are far from the corresponding failure threshold.

In Figure 4.2, mean values of $(I/I_{CR})_{max}$ for the N_{MCS} scenarios and their corresponding value of the learning function are shown for four iterations of the AK-MCS algorithm.
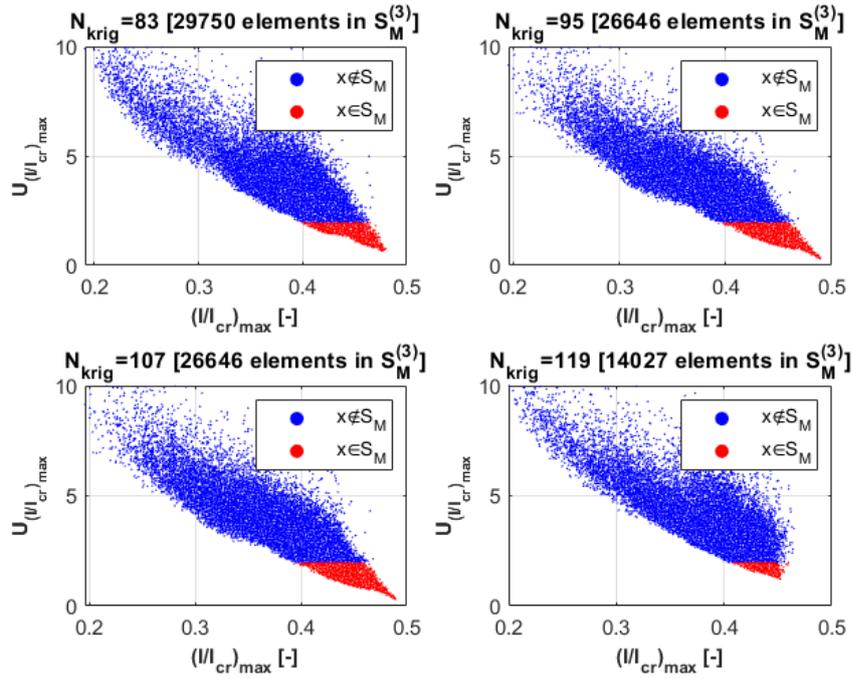
Figure 4.2 AK-MCS iterations

A progressive decrease in the number of configurations contained in $S_{\mathbb{M}}^{(3)}$ is evident at each step of the AK-MCS (they were halved after 4 iterations of the adaptive algorithm). In practice, this means that the area of the $S_{\mathbb{M}}^{(3)}$ region is reduced, i.e., that the precision (resp., uncertainty) of the Kriging metamodel in the characterization of the failure domain is increased (resp., decreased). On its turn, this demonstrates an improvement in the representativity of the abnormal (failure) scenarios in the dataset (in other words, a better coverage of the failure domain by the training dataset).

To provide few physical considerations on the results obtained, the characteristic component failures of the scenarios belonging to the $S_{\mathbb{M}}^{(3)}$ region are reported in Figure 4.3 (the frequencies of component failures in the Kriging-based simulated scenarios is plotted versus time). This information is of paramount importance, since it suggests the combinations of component failures that most likely lead the system to failure (or near-failure) conditions.
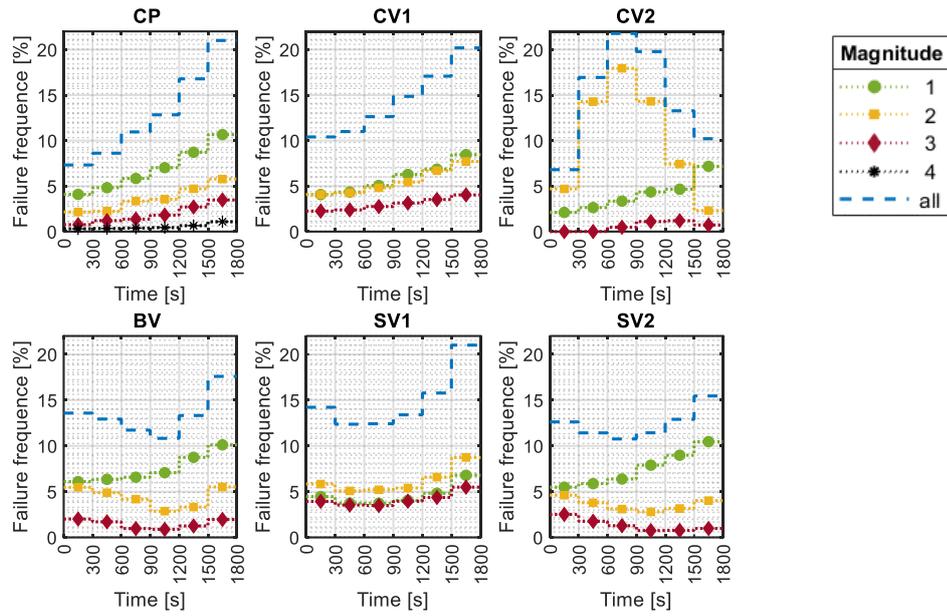
Figure 4.3 Characteristic Failures in $S_{\mathbb{M}}^{(3)}$

CV2 fails in 89% of the simulated transients, remaining partially open in 61% of the cases ($m = 2$): this failure does not involve a LOFA detection by the C1 controller alone, but it leads to a lower pressure at the CP upstream for the increasing pressure drop between the inlet and the outlet of the valve. CV1 and BV fail mostly with magnitudes $m = 2$ and $m = 1$, indicating that they remain stuck at their nominal position or partially open, while the CP provide at least more than 50% of the nominal flow in 85% of the scenarios (failures with low magnitude): in case of LOFA due to a cryoline obstruction (i.e., a CV closure), the complete closure of at least one CV and the complete opening of the BV are necessary to prevent the inventory decrease of helium at the suction of the pump and an additional pressure drop there. In addition, the QT communicates with the SMCCC for at least one SV failed with $m > 1$ in 71% of the cases, contributing for a further pressure decrease at the CP upstream.

If pressure reach a value below 0.23 MPa inside the SMCCC, the He is no more Supercritical and bi-phase occurs, but the 4C code is not able to operate in this condition and in real case the CP is not able to operate with such low pressure, so most of the $S_{\mathbb{M}}^{(3)}$ region might remain unexplored.

4.2 Proper Orthogonal Decomposition-based Kriging metamodels

In this section, an algorithm (still based on Kriging metamodels) is proposed to simulate a large number of new (time-varying) outputs $y_j^k(t)$ at a reduced computational cost, i.e., without resorting to the 4C code. These "new" (approximate) transients will be employed to enrich the database in the LOFA precursor identification algorithm of Chapter 3, with the aim of enhancing its performance.

The starting point of this analysis is represented by $N_{krig} = 119$ training scenarios (simulated by the 4C), available from the previous step of the analysis (i.e., from the AK-MCS iterations of Section 4.1). As mentioned before, the important feature of these exemplary training scenarios is that they provide a good coverage of the failure region of our interest. Each *i-th* scenarios is decomposed resorting to POD with truncation at the H_k element like in Eq.(4.14) (Marrel et al., 2014):

$$y_i^k(t) = \sum_{h=1}^{H_k} a_{ih}^k \cdot \varphi_h^k(t) \qquad (4.14)$$

Where $\varphi_h^k(t)$ (depending only on time t) is the orthogonal basis function of the *k-th* variable for the *h-th* base valid for all the N_{krig} scenarios, and a_{ih}^k (depending only on the input configuration $\mathcal{X}_i$) is its coefficient for the *i-th* scenario.

Each orthogonal function $\varphi_h^k(t)$ is characterized by the property shown in Eq.(4.15):

$$\int_{t=0s}^{t=t_{miss}} \varphi_{h_1}^k(t) \cdot \varphi_{h_2}^k(t) \cdot dt = \delta_{h_1 h_2} = \begin{cases} 0 & \text{if } h_1 = h_2 \\ 1 & \text{if } h_1 \neq h_2 \end{cases} \qquad (4.15)$$

Thanks for this property, each a_{ih}^k coefficient can be easily estimated with Eq.(4.16):

$$a_{ih}^k = \int_{t=0s}^{t=t_{miss}} y_i^k(t) \cdot \varphi_h^k(t) \cdot dt \qquad i = 1, \dots, N_{krig}; \ h = 1, \dots, H_k \qquad (4.16)$$

In order to employ this strategy for the simulation of new scenarios, the following procedure is performed for each *k-th* output variable.

Step 1: The $\bar{\bar{Y}}^k_{krig}[N_{krig}, L]$ matrix is updated with new scenarios computed in Section 4.1, containing the y^k_{il} value of the *k-th* variable of the *i-th* training scenario at the *l-th* time point at *i-th* row and *l-th* column.

Step 2: Single Value Decomposition (SVD) (Wall et al., 2003) is adopted to decompose $\bar{\bar{Y}}^k_{krig}$ like in Eq.(4.17):

$$\bar{\bar{Y}}^k_{krig}[N_{krig}, L] = \bar{\bar{\Psi}}^k[N_{krig}, N_{krig}] \cdot \bar{\bar{\Lambda}}^k[N_{krig}, L] \cdot \bar{\bar{\Phi}}^k[L, L] \tag{4.17}$$

Where $\bar{\bar{\Psi}}^k$ and $\bar{\bar{\Phi}}^k$ are matrixes that contains in their column left-singular vectors and right-singular vectors, respectively, and $\bar{\bar{\Lambda}}^k$ is a diagonal matrix containing the nonnegative Λ^k_h singular values in decreasing order.

Step 3: Λ^k_h ($h = 1, \dots, N_{krig}$) are employed to identify the best number H_k of basis to use with Eq.(4.18):

$$\Gamma^k_h = \frac{\sum_{j=1}^{h} \Lambda^k_j}{\sum_{h=1}^{N_{krig}} \Lambda^k_h} \tag{4.18}$$

Γ^k_h indicates the percentage of the variability of the real N_{krig} transients that can be "explained" by the POD decomposition truncated at *h-th* basis. In this work, H_k is the number of (ordered) basis for which Γ^k_h reaches a value of 0.99 (i.e., for which the POD decomposition is able to explain the 99% of the variability of the real transients). The $\bar{\bar{\Phi}}^k[L, H_k]$ matrix is then truncated at the H_k-*th* column and its generic element at *l-th* row and *h-th* column is φ^k_{lh}, corresponding to the value of the orthogonal basis $\varphi^k_h(t)$ of the *h-th* base at *l-th* time.

Step 4: Each a^k_{ih} coefficient is contained in the *i-th* row and the *h-th* column of the matrix $\bar{\bar{A}}^k[N_{krig}, H_k]$, calculated as in Eq.(4.19):

$$\bar{\bar{A}}^k = \bar{\bar{Y}}^k \cdot \bar{\bar{\Phi}}^{k^T} \tag{4.19}$$

with $\bar{\bar{\Phi}}^{k^T}[H_k, L]$ the transposal of $\bar{\bar{\Phi}}^k$. This equation corresponds to the Eq.(4.16), but in discretized form.

Step 5: For each *h-th* base a Kriging metamodel $\mathcal{MM}_h^k$ is developed, where the training set (DOE) includes all the inputs $\overline{\mathbf{X}} = \{\mathbf{X}_1, \mathbf{X}_2, \dots, \mathbf{X}_{N_{krig}}\}$ and the corresponding coefficients $\mathbf{a}_h^k = \{a_{1h}^k, a_{2h}^k, \dots, a_{N_{krig}h}^k\}$ as outputs: each metamodel $\mathcal{MM}_h^k$ will be the one with the lowest LOO error between $N_{iter} = 100$ attempts of training. In this way, for a new input $\mathbf{X}$ we can predict each coefficient of the POD decomposition $\hat{a}_h^k(\mathbf{X}) = \mathcal{MM}_h^k(\mathbf{X})$ (for each coefficient we have the mean Kriging value $\mu_{\hat{a}_h^k}(\mathbf{X})$ and the Kriging variance $\sigma_{\hat{a}_h^k}(\mathbf{X})$).

Step 6: Each time-varying output $y_j^k(t)$ of the $N_{MCS} = 100000$ scenarios (generated resorting to MCS to be simulated with metamodels) is approximated at *l-th* time step as in Eq.(4.20):

$$\tilde{y}_{jl}^k = \sum_{h=1}^{H_k} \mu_{\hat{a}_h^k}(\mathbf{X}_j) \cdot \varphi_{lh}^k, \quad j = 1, \dots, N_{MCS}; l = 1, \dots, L \qquad (4.20)$$

Where $\tilde{y}_{jl}^k$ is the approximated value of y_{jl}^k, resulting from the metamodel-based POD decomposition

In this way, by resorting to multiple Kriging metamodels instead of the 4C code, the computational time for simulating a single new scenario is reduced from an average of two days to about 1.1s per simulation.

4.2.1 LOFA occurrence time estimation

The same procedure described in the previous Section is also adopted to approximate $G_{max}(t)$, that will be employed in the estimation of $t_{LOFA,C1,j}$ (i.e., of the time when a LOFA is detected by C1) for a new *j-th* scenario. The quantity $G_{max}(t)$ is defined in Eq.(4.21):

$$G_{max}(t) = \max\left(G_{CSM,in}(t), G_{CSM,out}(t)\right) \qquad (4.21)$$

Where $G_{CSM,in}(t)$ is the inlet flow to the CSM and $G_{CSM,out}(t)$ the outlet flow.

In the original 4C code, these two variables are controlled by component C1: when $G_{CSM,in}(t) < 0.032 \, kg/s$ and $G_{CSM,out}(t) < 0.032 \, kg/s$ for more than the validation time ($\tau_{val} = 1s$), a LOFA takes place and is detected by controller C1

(see Section 2.3.1 for details). Instead, for a generic *j-th* scenario among the N_{MCS} simulated, $G_{max,j}(t)$ is approximated at each *l-th* time step by computing $\tilde{G}_{max,lj}$ with POD-based Kriging metamodels and, then, $\tilde{t}_{LOFA,C1,j}$ (i.e., the approximation of $t_{LOFA,C1,j}$) is identified and stored, when $\tilde{G}_{max,lj} < 0.032 \ kg/s$ for more than $\tau_{val} = 1s$ (thus, mimicking the operation of the controller C1).

To this aim, new basis functions $\varphi_{G,lh}$ ($l = 1, ..., L; h = 1, ..., H_G$) and their coefficients g_{ih} ($i = 1, ..., N_{krig}$) are determined. Then, each metamodel MM_h^G is trained with $\boldsymbol{g}_h = \{g_{1h}, g_{2h}, ..., g_{N_{krig}h}\}$ coefficients as outputs to predict $\hat{g}_h(\boldsymbol{X}) = MM_h^G(\boldsymbol{X})$ in correspondence of a new input $\boldsymbol{X}$ (the mean Kriging value is $\mu_{\hat{g}_h}(\boldsymbol{X})$ and its Kriging variance is $\sigma_{\hat{g}_h}(\boldsymbol{X})$). Mean Kriging values will be employed to estimate $\tilde{G}_{max,lj}$ such as in Eq.(4.22):

$$\tilde{G}_{max,lj} = \sum_{h=1}^{H_G} \mu_{\hat{g}_h}(\boldsymbol{X}_j) \cdot \varphi_{G,lh} , \quad j = 1, ..., N_{MCS}; l = 1, ..., L \qquad (4.22)$$

4.2.2 Scenarios discarded

For some scenarios, the estimated coefficients of the POD bases may have large Kriging variance, due to the limited-size of the training set, containing only 119 transients (this value is extremely small, if we consider that the dimensionality of the input space is 12). The transients characterized by "large uncertainty" have been discarded in order not to invalidate the information contained in each map built for LOFA precursors identification.

For this reason, for each *j-th* scenario ($j = 1, ..., N_{MCS}$) the absolute error $\sigma_{abs}^k(\boldsymbol{X}_j)$ of all the H_k basis coefficients is determined as in Eq.(4.23):

$$\sigma_{abs}^k(\boldsymbol{X}_j) = \frac{\sum_{h=1}^{H_k} \sigma_{\hat{a}_h^k}(\boldsymbol{X}_j) \cdot \Lambda_h^k}{\sum_{h=1}^{H_G} \Lambda_h^k} \qquad (4.23)$$

In this way, each *h-th* Kriging variance is weighted according to its associated singular values Λ_h^k, containing the information of how the $\varphi_h^k(t)$ basis signal is important in output estimation.

Similarly, a_{max}^k and a_{min}^k are calculated in Eq.(4.24) and Eq. (4.25), respectively, to determine the order of magnitude of σ_{abs}^k, employing $\boldsymbol{a}_h^k$ coefficients of training scenarios of each *h-th* base:

$$a_{max}^k = \frac{\sum_{h=1}^{H_G} \max(\boldsymbol{a}_h^k) \cdot \Lambda_h^k}{\sum_{h=1}^{H_G} \Lambda_h^k} \tag{4.24}$$

$$a_{min}^k = \frac{\sum_{h=1}^{H_G} \min(\boldsymbol{a}_h^k) \cdot \Lambda_h^k}{\sum_{h=1}^{H_G} \Lambda_h^k} \tag{4.25}$$

Finally, a general information of the relative error $\sigma_{rel}^k(\boldsymbol{X}_j)$ for the *j-th* scenario approximated is evaluated in Eq.(4.26):

$$\sigma_{rel}^k(\boldsymbol{X}_j) = \sigma_{abs}^k(\boldsymbol{X}_j)/(a_{max}^k - a_{min}^k) \tag{4.26}$$

If $\sigma_{rel}^k(\boldsymbol{X}_j)$ is above 10%, $\boldsymbol{X}_j$ will be discarded.

At the end of this step, $N_{POD} = 694$ scenarios of the $N_{MCS} = 100000$ (simulated with metamodels) satisfying the condition of $\sigma_{rel}^k < 10\%$ are retained and added to the database of the LOFA precursor identification algorithm already *available* (constituted by $N_{krig} = 119$ scenarios simulated by the real 4C code).

4.3 Amendments to the LOFA precursors identification algorithm

Now the dataset is composed by $N_{data} = N_{krig} + N_{POD} = 813$ scenarios, including those simulated with 4C in Section 4.1 and the ones approximated with POD in Section 4.2 to those described in Section 3.2.

For each *i-th* element of the dataset ($i = 1,2, \dots, N_{data}$), different variables are available:

- Magnitudes and timings of failures in $\boldsymbol{X}_i$ input;
- trend of each *k-th* critical variable $y_i^k(t)$ ($k = 1, \dots, N_k$);
- The LOFA detection time $t_{LOFA,C1,i}$ by the C1 controller.

These data are collected to build new maps in Section 4.3.1 and, then, LOFA precursors identification algorithm is modified in Section 4.3.2 to employ these new maps.

4.3.1 New dataset description

The $N_{data} - N_{train}$ scenarios must be associated to one of the $C = 9$ clusters to produce a new LOFA occurrence map and new failure maps. To this aim, the OSSC of Section 3.3 is applied to each i-th scenario to obtain each $M_{L,ci}$ membership to the c-th cluster at the L-th time step using its N_k critical variables. Each i-th scenario belongs to the c-th cluster if $M_{L,ci} > M_{lim} = 0.7$ like in (Bellaera et al., 2018).

The trends of the critical variables $p_{CSM,in}$, T_{hs} and I/I_{cr} for the N_{data} scenarios, grouped in cluster, are sketched in Figure 4.4, Figure 4.5 and Figure 4.6 in dotted lines: these lines are compared to the prototypical one, drawn with continuous line, of their reference cluster.
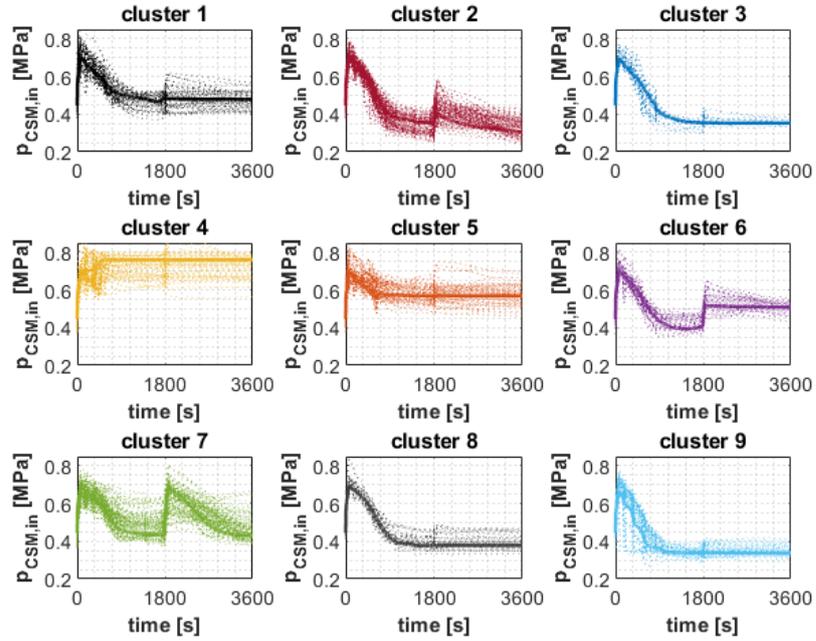
Figure 4.4 Prototypical behaviour of $p_{CSM,in}$ for each cluster with N_{data}

56
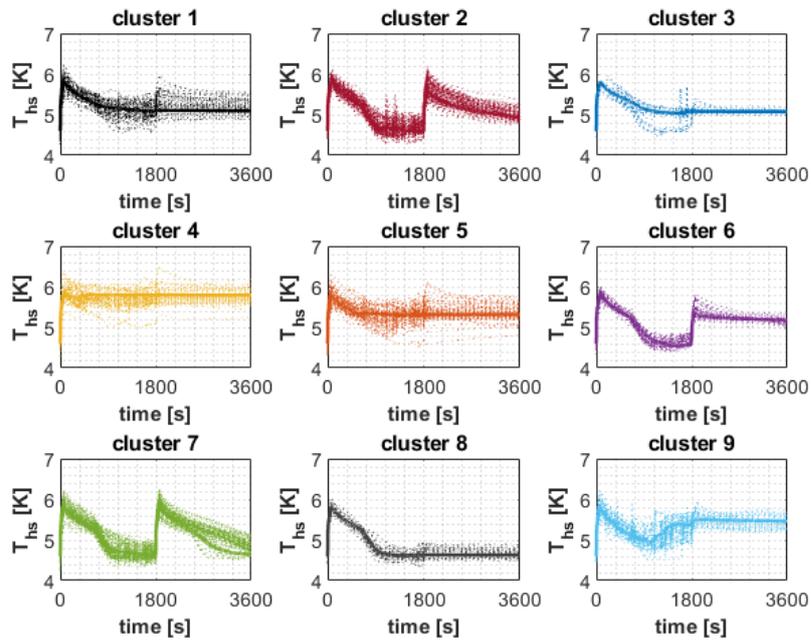
Figure 4.5 Prototypical behaviour of T_{hs} for each cluster with N_{data}
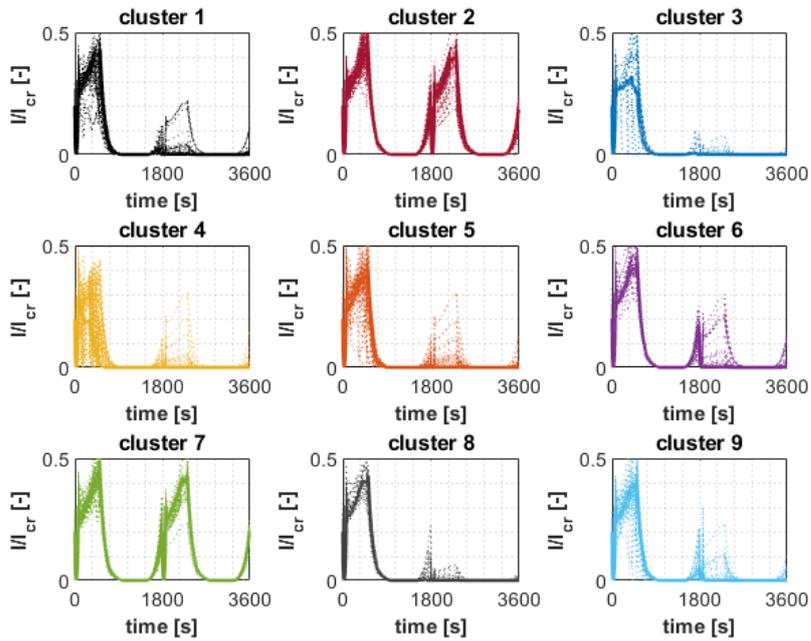
Figure 4.6 Prototypical behaviour of I/I_{cr} for each cluster with N_{data}

It can be noted that each cluster is enriched with respect to Figure 3.1, Figure 3.2 and Figure 3.3.

In order to produce the LOFA occurrence map, the LOFA probability $P_{LOFA,l}(c)$ at *l-th* time for each *c-th* cluster is determined as in Eq.(4.27), by counting the number of occurrences of this event at each *o-th* interval of 300s and dividing it by the number of transients $N_{data,c}$ in that cluster:

$$P_{LOFA,l}(c) = \frac{\sum_{i=1}^{N_{data,c}} \Theta(t_{LOFA,C1,i} \in [t_o, t_{o+1}])}{N_{data,c}} \tag{4.27}$$

$$\text{where} \quad \Theta(x) = \begin{cases} 0 & \text{if } x \text{ false} \\ 1 & \text{if } x \text{ true} \end{cases} \tag{4.28}$$

$[t_o, t_{o+1}]$ is the *o-th* interval, where the *l-th* time belongs, and $\Theta(x)$ is the Heaviside function used to count the phenomena. With respect to the algorithm of Chapter 3, in this case the calculation of the probability $P_{LOFA,l}(c)$ of having a LOFA at time l in a transient of cluster c can be computed exploiting the "richer" statistical information available thanks to the numerous metamodel-based simulations.

Results of this procedure are shown in Figure 4.7
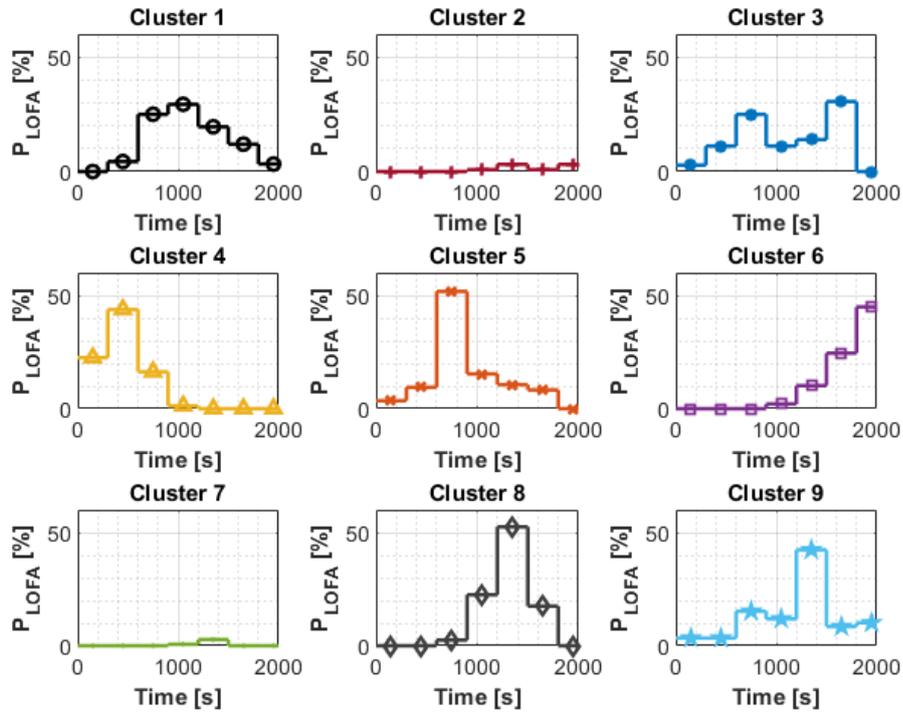
Figure 4.7 Probability distribution of LOFA occurrence time for each cluster

Like for the old dataset (see Figure 3.4), LOFA is not characteristic of Cluster 2 and 7 and it is more frequent during the B phase [130s,516s] in Cluster 4, during the R phase [516s,975s] in Cluster 5, between the R phase and the D phase [975s,1490s] in Cluster 1, at the end of the D phase in Cluster 8 and in the M phase [1490s,1800s] and after the first pulse in Cluster 8. The LOFA event is distributed along the entire time horizon in Cluster 3 and 9, but there are two peaks in R and M phase, respectively, for the former and a peak at D phase for the latter, similarly to Figure 3.4(left).

The failure map is constructed by calculating the probability of failure of each *e-th* component in a defined *c-th* cluster by counting the times that the *e-th* component fails ($m_e \neq 0$) at τ_e time in intervals of 300s and dividing it by $N_{data,c}$, as in Eq.(4.29):

$$P_{FAIL,l}(e|c) = \frac{\sum_{i=1}^{N_{data,c}} \Theta(\tau_{e,i} \in [t_o, t_{o+1}] \wedge m_{e,i} \neq 0)}{N_{data,c}} \tag{4.29}$$

Applying the equation above to all the components and for all the clusters, Figure 4.8 is obtained. The Figure shows the probability that a component fails in a particular time interval, *given* that the transient under analysis belongs to a specified cluster.
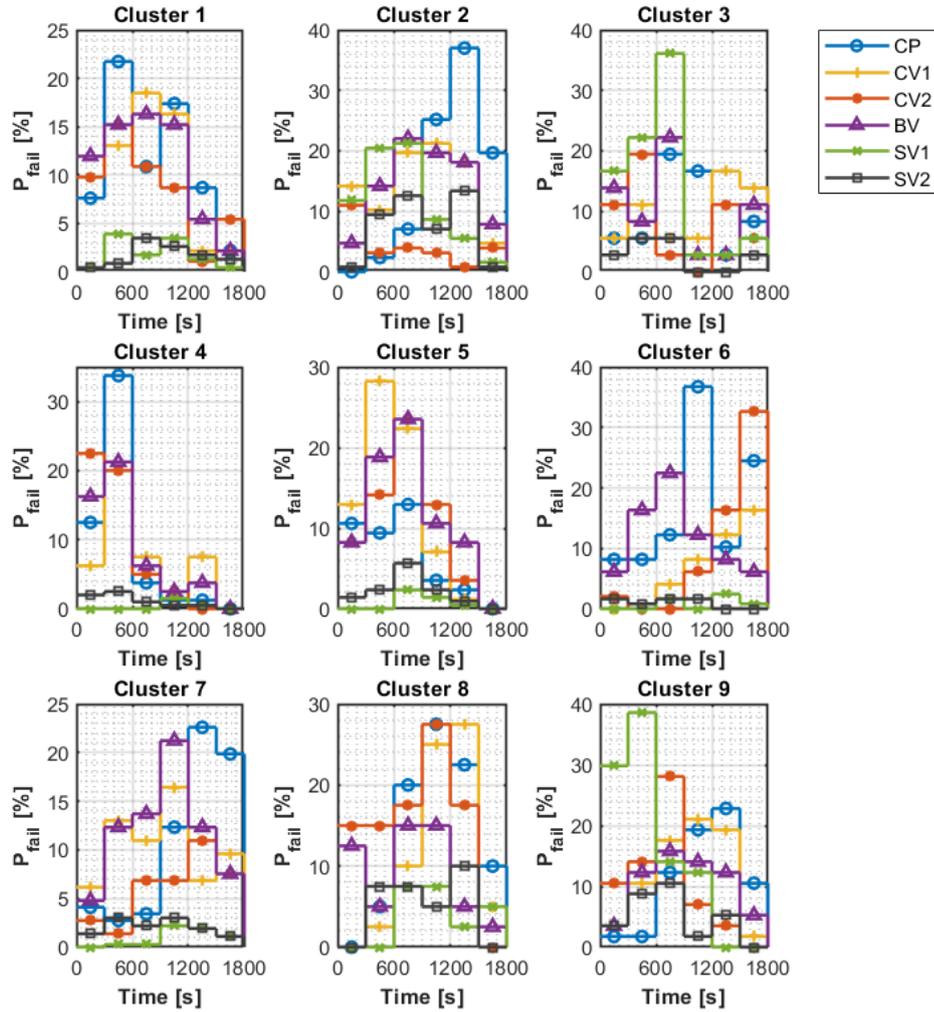
Figure 4.8 Probability Failure occurrence for each cluster and component

As before, the higher level of detail with respect to the algorithm of Section 3 (e.g., the possibility to distinguish the different CVs and the different SVs) was possible thanks to the higher number of transients available in each cluster. Comparing this map with that of Figure 3.5, there are several similarities: SV1 and SV2 fail mostly in Cluster 2, 3, 8 and 9; failures of the CP, the CVs and the BV are present in all clusters, but their $P_{FAIL,l}(e|c)$ is distributed differently. On the other hand, the BV failure is present in Cluster 3 and Cluster 7 is also characterized by failures of the CVs and the BV with low magnitude, differently from Figure 3.5, where they do not occur.

Generally, each $P_{LOFA,l}(c)$ and $P_{FAIL,l}(e|c)$ "extend" the old maps providing important additional information, such as the distributions of LOFA times and components failures, differently from the information contained in $\bar{\bar{\mathcal{L}}}$ and $\bar{\bar{\mathcal{F}}}$ matrix, described in Section 3.2. Moreover, the OSSC procedure in Section 3.3, in particular the 9th step, must be properly modified to employ $P_{LOFA,l}(c)$ and $P_{FAIL,l}(e|c)$ instead of the $\bar{\bar{\mathcal{L}}}$ and $\bar{\bar{\mathcal{F}}}$ matrix.

4.3.2 Settings of the new LOFA precursors identification algorithm

The 9th step of OSSC procedure of Section 3 is the one that analyses at each *l-th* time step the $M_{rel,l,cj}$ and $V_{rel,l,cj}$ values, corresponding to each *c-th* cluster, reached by the *j-th* scenario, and it is here modified as follows.

In step 9a, $V_{rel,l,cj}$ $[c = 1, \dots, C]$ is compared to $V_{lim,LOFA,l}$ with a different pseudo code, described in Figure 4.9. In extreme synthesis, if at least two values of $V_{rel,l,cj}$ overcome the threshold $V_{lim,LOFA,l}$ at time l, $P_{LOFA,l,j}$ assumes a value different from zero and, if it exceed $P_{LOFA,lim}$, the algorithm identifies the LOFA precursors.

At *l-th* time
    Calculate $V_{1st} = \max\limits_{c}(V_{rel,l,cj})$;
    Calculate $c_{1st} = \arg\left(\max\limits_{c}(V_{rel,l,cj})\right)$;
    Calculate $V_{2nd} = \max\limits_{c \neq c_{1st}}(V_{rel,l,cj})$;
    Calculate $c_{2nd} = \arg\left(\max\limits_{c \neq c_{1st}}(V_{rel,l,cj})\right)$;
    If $(V_{1st} > V_{lim,LOFA,l}$ & $V_{2nd} > V_{lim,LOFA,l})$
        Calculate $P_{LOFA,l,j}$ with Eq.(4.30)
    Else
        $P_{LOFA,l,j} = 0$;
    End
    If $P_{LOFA,l,j} > P_{LOFA,lim}$
        LOFA precursor is identified;
    Else
        LOFA precursor does not exist;
    End

Figure 4.9 New Pseudo code for $V_{rel,l,cj}$ analysis

$P_{LOFA,l,j}$ is calculated employing each $P_{LOFA,l}(c)$ as in Eq.(4.30):

$$P_{LOFA,l,j} = \frac{P_{LOFA,l}(c_{1st,l}) + P_{LOFA,l}(c_{2nd,l})}{\sum_{c}^{C=9} P_{LOFA,l}(c)} \tag{4.30}$$

$V_{lim,LOFA,l}$ and $P_{LOFA,lim}$ are values determined from training data employing the $N_{krig} = 119$ scenarios and not all the $N_{data} = 813$ ones. Indeed, the remaining $N_{POD} = 694$ scenarios are not accurate near LOFA occurrence, because their critical variables are approximation of the real trends derived from the real code.

$V_{lim,LOFA,l}$, displaced in Figure 4.10, was updated with N_{krig} scenarios instead of N_{train} ones, following the pseudo-code of Figure 3.12.
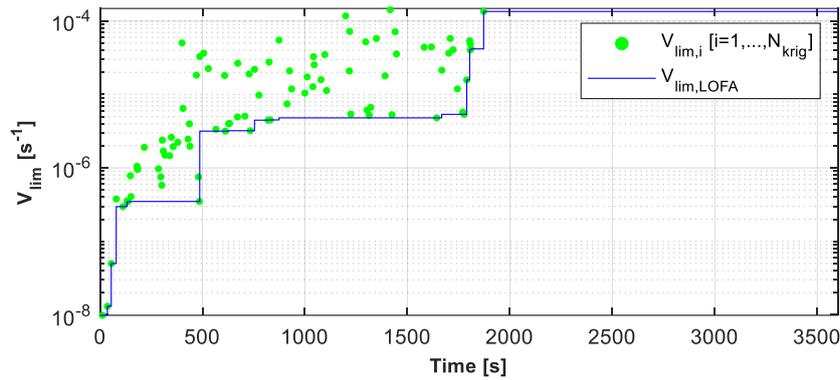
Figure 4.10 New $V_{lim,LOFA,l}$ trend in logarithmic scale (blue line) and $V_{lim,i}$ point used to evaluate it (green points)

$P_{LOFA,lim}$ was set in order to reduce the number of false positives in LOFA detection as sketched in Figure 4.11: points in red depict the maximum values reached by $P_{LOFA,l}$ from 0s to $t_{LOFA,C1}$ in scenarios where a LOFA occurs, whereas points in green represents the maximum values reached by $P_{LOFA,l}$ during the entire time length in scenarios where a LOFA does not occurs. Imposing $P_{LOFA,lim} = 19\%$, 10 to 25 scenarios with no LOFA will be below $P_{LOFA,lim}$, reducing consequently the number of possible false positives in LOFA identification.
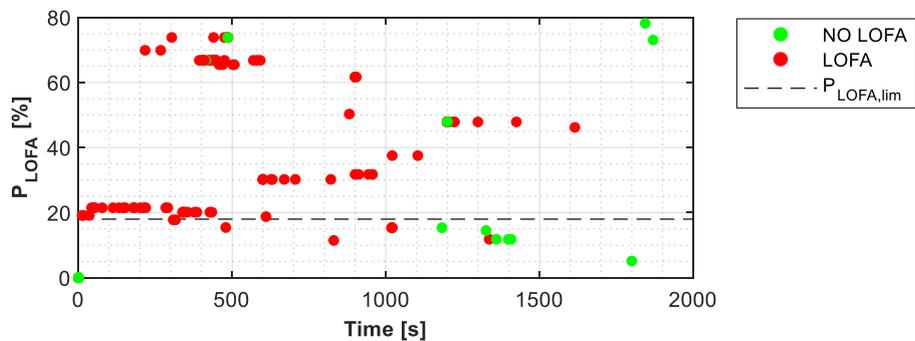
Figure 4.11 Maximum $P_{LOFA,l,i}$ for scenarios with LOFA (red) and with NO LOFA (green) and representation of $P_{LOFA,lim}$

In step 9b, the new pseudo code shown in Figure 4.12, is followed. At each l-th time, $f_{Cl,l,j}(c)$ and, then, $P_{Cl,l}(c)$ are calculated with Eq.(4.33) and Eq.(4.32), respectively, for each c-th cluster: the former assume a value equal to $P_{LOFA,l}(c)$ [see Eq.(4.27)] only if the corresponding membership $M_{rel,l,cj}$ overcomes the limit value $M_{lim,FAIL.l}$ and the latter indicate how much the c-th cluster is responsible of the failure. Afterword, $P_{FAIL,l,j}(e)$ is determined with Eq.(4.31) for each e-th component: its terms are composed by the values assumed by $P_{FAIL,l}(e|c)$ (estimated with Eq.(4.29)), that indicates the probability of failure of the e-th component respect to the c-th cluster at l-th time, times $P_{Cl,l}(c)$ with the information of the c-th cluster responsible at l-th time for the j-th scenario. If $P_{FAIL,l,j}(e)$ overcomes $P_{FAIL,lim}(e)$, the e-th component is considered failed.

$$P_{FAIL,l,j}(e) = \sum_{c}^{C=9} P_{FAIL,l}(e|c) \cdot P_{Cl,l,j}(c) \qquad (4.31)$$

$$\text{where} \quad P_{Cl,l}(c) = \frac{f_{Cl,l,j}(c)}{\sum_{c}^{C=9} f_{Cl,l,j}(c)} \qquad (4.32)$$

$$\text{and} \quad f_{Cl,l,j}(c) = \begin{cases} P_{LOFA,l}(c) & \text{if } M_{rel,l,cj} > M_{lim,FAIL.l} \\ 0 & \text{if } M_{rel,l,cj} \leq M_{lim,FAIL.l} \end{cases} \qquad (4.33)$$

At l-th time
  For c-th cluster
    Calculate $f_{Cl,l,j}(c)$ with Eq. (4.33)
    Calculate $P_{Cl,l}(c)$ with Eq.(4.32)
  End
  For each e-th component
    Calculate $P_{FAIL,l,j}(e)$ with Eq.(4.31)
    If $P_{FAIL,l,j}(e) > P_{FAIL,lim}(e)$
      e-th component is failed
    End
  End

Figure 4.12 New Pseudo code for $M_{rel,l,cj}$ analysis

$M_{lim,FAIL.l}$ trend and each $P_{FAIL,lim}(e)$ are determined from $N_{krig} = 119$ scenarios with same rules explained in Section 3.3. The S coefficient found to calculate $M_{lim,FAIL,l}$ as in Eq.(3.8) is increased to $S = 9.81 \times 10^{-8} \ s^{-1}$.

Each $P_{FAIL,lim}(e)$ was set in order to reduce the number of false positives in LOFA precursors identification as sketched in Figure 4.13. In each *e-th* graph, where the *e-th* component fails (red points) and where it works in normal condition (green points), the maximum value reached by $P_{FAIL,l,i}(e)$ between "*0s*" and "$t_{LOFA,C1,i}$ +*30s*" (30s is the time of the rump down of the current after a LOFA after which the belonging cluster of *i-th* scenario become clear) for every *i-th* training scenarios ($i = 1, ..., N_{krig}$) are reported with the suggested value for $P_{FAIL,lim}(e)$: imposing 8%, 10%, 3%, 5%, 25% and 8% for $P_{FAIL,lim}(CP)$, $P_{FAIL,lim}(CV1)$, $P_{FAIL,lim}(CV2)$, $P_{FAIL,lim}(BV)$, $P_{FAIL,lim}(SV1)$, $P_{FAIL,lim}(SV2)$, respectively, we decrease the number of green points (potential false positives) above the $P_{FAIL,lim}(e)$, but limiting red points below it (potential false negatives).
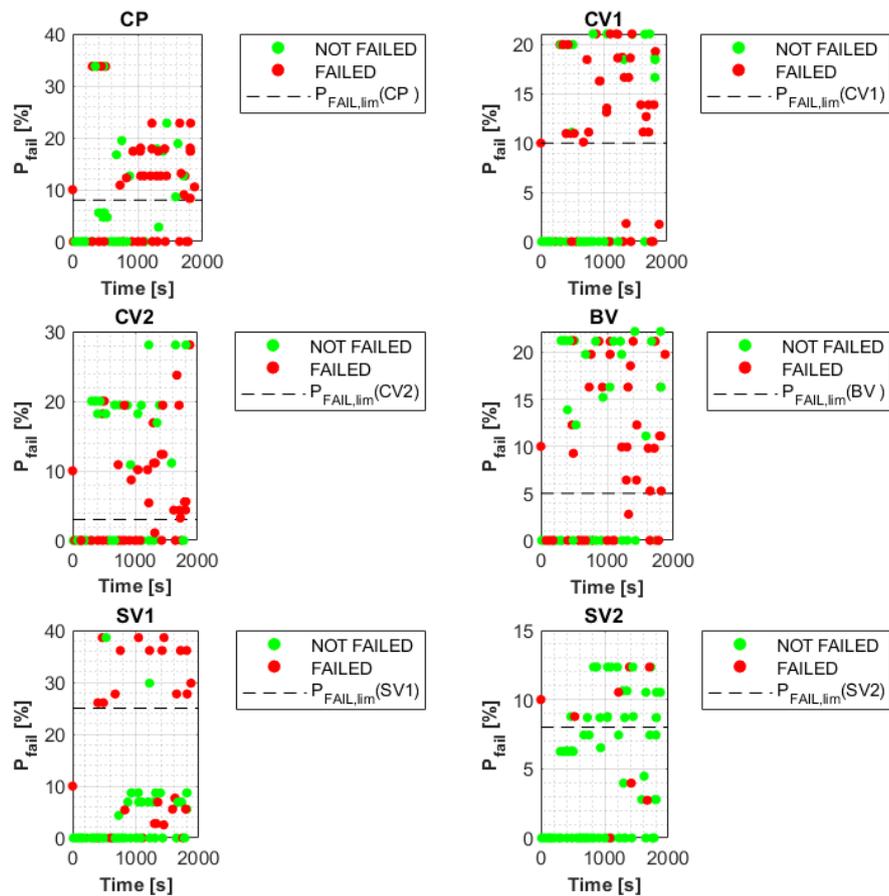
Figure 4.13 Maximum $P_{FAIL,l,i}(e)$ for scenarios where the e-th component is "failed" (red point) and where it work at normal condition (green point) and representation of each $P_{FAIL,lim}(e)$ (dashed line)

4.4 Results

The modified LOFA precursors identification is tested with the same $N_{test} = 38$ scenarios of Section 3.4, different from the $N_{data} = 813$ scenarios adopted in Section 4.3.1 of the new dataset.

As an example, the scenario "partial closure of BV at 0s, CP speed at 75% at 1s, complete closure of CV2 at 71s and complete closure of CV1 at 72s", whose values of $M_{rel,l,cj}$ and $V_{rel,l,cj}$ $(c = 1, ..., C)$ are drawn in Figure 4.14, is considered: this scenario is clearly of Cluster 4, because the rise of $M_{rel,l,4j}$ and $V_{rel,l,4j}$ show an affinity to this cluster.
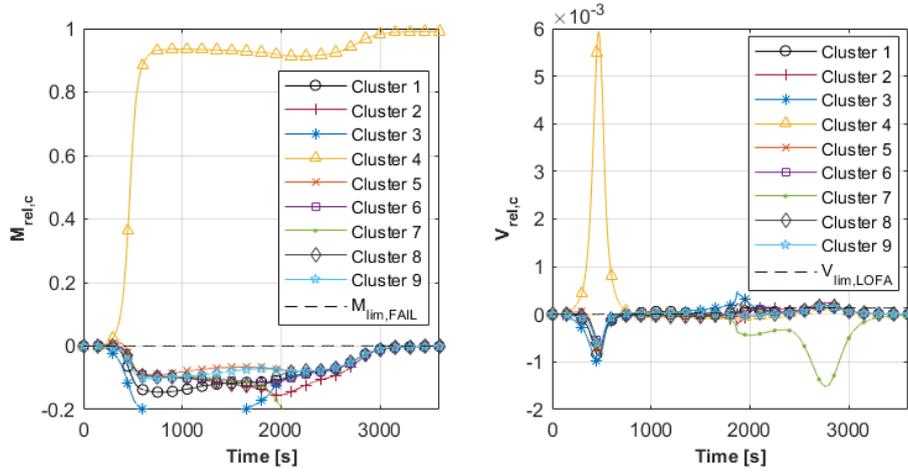
Figure 4.14 $M_{rel,l,cj}$ trends (left) and $V_{rel,l,cj}$ trends (right) for scenario "partial closure of BV at 0s, CP speed at 75% at 1s, complete closure of CV2 at 71s and complete closure of CV1 at 72s"

$M_{rel,l,cj}$ and $V_{rel,l,cj}$ are analysed like shown in Figure 4.15: each $V_{rel,l,cj}$ is treated every *l-th* time to calculate $P_{LOFA,l,j}$ (continuous blue line in Figure 4.15(above)), that is compared with $P_{LOFA,lim}$ (dashed line); each $M_{rel,l,cj}$ is employed to determine each $P_{FAIL,l,j}(e)$ (marked continuous lines in Figure 4.15(six plots below)), that is compared with its $P_{FAIL,lim}(e)$ (dashed line).
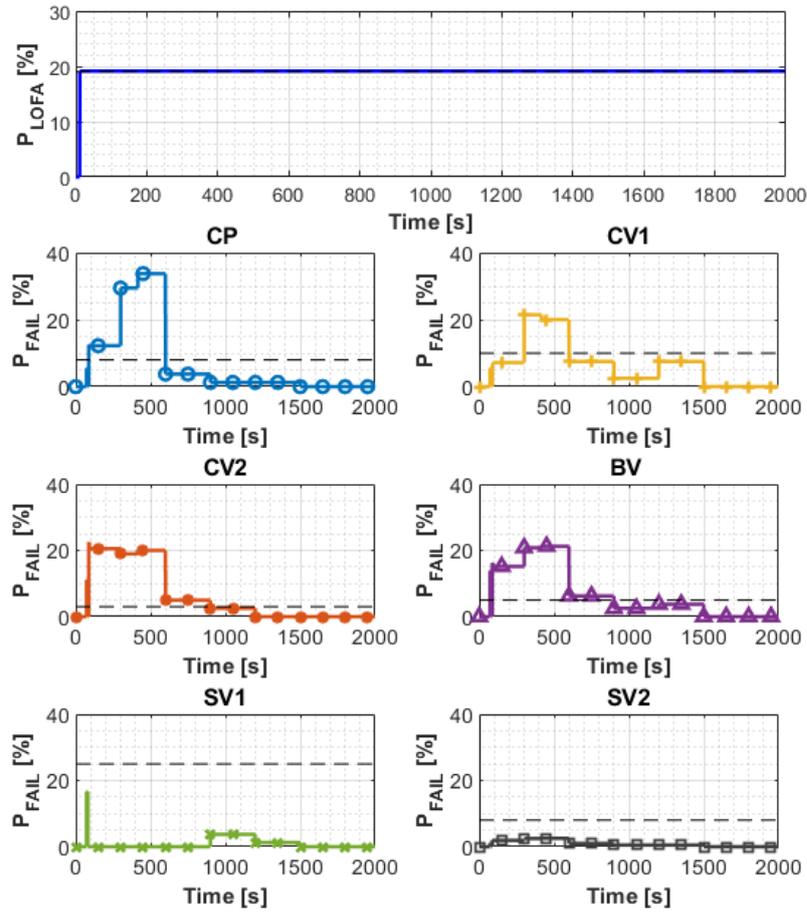
Figure 4.15 $P_{LOFA,l,j}$ (above) and $P_{FAIL,l,j}(e)$ (six plots below) values for scenario "complete closure of CV1 at 623s" compared with their limits

At 11.2s, $P_{LOFA,l,j}$ overcomes $P_{LOFA,lim}$ with a consequent LOFA identification. At 72.6s, $P_{FAIL,l,j}(CV2)$ and $P_{FAIL,l,j}(BV)$ reaches their limits, so the CV2 and the BV are considered as precursors. At 87.2s, also the CP is identified as precursors, because $P_{FAIL,l,j}(CP)$ overcome $P_{FAIL,lim}(CP)$. Finally, $P_{FAIL,l,j}(CV1)$ reaches $P_{FAIL,lim}(CV1)$ at 300s and its failure is in turn identified. Instead, the SV1 and the SV2 are considered "safe", because their failure probability remains below the limit. In summary, LOFA is detected 61.9s earlier than $t_{LOFA,C1,j} = 73.11s$ whereas the CV2, the BV, the CP and the CV1 LOFA precursors are identified 1.6s, 72.6s, 86.2s and 218s later than the real misfunctioning, respectively.

In Table 4.1, the results of the extensive analysis performed with the modified LOFA precursors identification on the $N_{test} = 38$ scenarios are listed.

Table 4.1 New Results on $N_{test} = 38$ scenarios

Scenarios with LOFA	**32**
LOFA predicted in advance	24
LOFA not predicted in advance	8
Scenarios with NO LOFA	**6**
Correct identification NO LOFA	4
False positive LOFA	2

Differently from Table 3.1, LOFA that are identified late are increased from 6 to 8: none of these have a LOFA during the B phase, so the CSM is not endangered. On the other hand, the correct identifications of scenarios with no LOFA increase from 2 to 4, reducing the overall false positives. Also in these case, LOFA is predicted in advance in several scenarios where the LOFA actually occurs; in addition, most of the scenarios, where LOFA does not occurs, are identified as "safe".

In Table 4.2, results of precursors identification for the 32 scenarios with LOFA, employing the modified algorithm, are reported as done for Table 3.2.

Table 4.2 New Results of the precursor identification approach for $N_{test} = 38$ scenarios

	Correct precursor identification	False negative	Correct identification of normal operation	False positive
CP	21	2	2	7
CV1	16	0	2	14
CV2	13	2	9	8
BV	14	2	3	13
SV1	1	1	25	5
SV2	2	2	20	8

It can be seen that the modified version of LOFA precursor identification continues to conservatively overestimate the number of failed components, but false positives are *consistently* reduced with respect to Table 3.2 with a *very slight* decrease in the precursors identified correctly.

5 Conclusion

The objective of this thesis was to propose an approach to promptly identify the precursors of a Loss-Of-Flow Accident (LOFA) in a simplified cryogenic cooling circuit (SMCCC), which has the task of keeping one ITER Central Solenoid (CS) module cooled. In case of a LOFA, this cooling capability is obviously compromised, so that pressure and temperature inside the CS may surge rapidly, possibly causing serious damages to the system (for example, the superconducting properties of the magnet may be lost).

To this aim, an On-line Supervised Spectral Clustering (OSSC) method embedding the Fuzzy C-Means (FCM) algorithm has been proposed as a *novel*, *original* strategy to identify LOFA precursors (i.e., combinations of component failures leading to a LOFA) from signals of a developing (accident) scenario in a simulated case study. The deterministic 4C code has been used to simulate the SMCCC behaviour, when coupled with one of the six ITER Central Solenoid Modules (CSMs), and to develop signals of the abnormal and accident scenarios.

A *limited-sized* set of $N_{train} = 83$ "exemplary" scenarios is used to "train" the proposed LOFA precursor identification algorithm. These scenarios have been clustered into the $C = 9$ groups, characterized by similar time behaviour of the system safety-critical variables (i.e., the monitored signals), similar components failures (i.e., LOFA precursors) and times of LOFA occurrence. This information has been employed to build a sort of "map" for LOFA precursor identification. The algorithm (together with the corresponding maps) has been then "tested" on additional (*new*, *unknown*) $N_{test} = 38$ scenarios to verify its robustness. It has been shown that the elaborated method recognises timely 82% of the LOFA precursors and identifies 87% of the components failed. On the other hand, it (erroneously) detects LOFA precursors in 67% of the scenarios with no LOFA and identifies as precursors 79% of components that are not actually failed. In other words, on one side, this *conservatively increases* the *safety* of the SMCCC (by overestimating the number of failed components); on the other side, it *reduces* its *availability* (due, e.g., to unnecessary inspection procedures).

In the light of these results, the quality of the "maps" employed in the LOFA precursors identification algorithm has been improved by *intelligently* increasing the number of *training scenarios* (with the main objective of reducing such overestimation). In particular, innovative, advanced computational methods based on *fast-running* surrogate regression models (namely, Kriging metamodels) have been developed to increase the number of training scenarios available, but at a reduced computational cost (i.e., by circumventing the huge computational burden of the 4C code). In a first step, the Adaptive Kriging – Monte Carlo Sampling (AK-MCS) has been built to *progressively enrich* the (training) dataset in proximity of the region of the system state space that is of our interest (i.e., the "failure" region containing those components configurations that likely leads the system to a LOFA). This approach has allowed reducing the number of calls to the original, long-running 4C code by *preferentially* guiding/pushing the exploration towards the abnormal (LOFA) scenarios of our interest, while avoiding a waste of time in the simulation of ("useless") safe scenarios. By so doing, the training dataset has been extended to $N_{krig} = 119$ transients (characterized by a satisfactory coverage of the failure region). Then, a Proper Orthogonal Decomposition (POD)-based Kriging metamodel has been developed and trained (by means of the N_{krig} scenarios thereby obtained) to simulate quickly ($N_{data} = 813$) *time-varying* signals (i.e., to reproduce the transient behaviour of the safety-critical variables of our interest). In other words, the POD-based kriging metamodel has been used to *fully* "mimic" the behaviour of the 4C code, but with a sharp drop in the computation cost, from an average of two days to ~1.1s per simulation (on an Intel Core i3-7100 3.90 GHz 3MB Cache). Finally, this new (significantly enlarged) set of scenarios has been employed in a modified version of the LOFA precursors identification algorithm, which has been "re-tested" on the $N_{test} = 38$ scenarios and compared to the previous version. The results have shown a decrease from 67% to 33% in the (erroneous) LOFA identifications and a drop from 79% to 56% in the (erroneous) precursor identification: in other words, the number of "false positives" has been reduced in a *consistent* way. On the other hand, the rate of LOFA timely identifications has *slightly* diminished from 82% to 75% and the rate of correct

precursor identifications has slightly reduced from 87% to 78%, producing a slight increase in the "false negatives". Overall, the percentage decrease of "false positives" is much more consistent than the increase of "false negatives": in other words, the safety of the system analysed is still conservatively guaranteed, but its unavailability (due, e.g., to unnecessary inspection procedures) is strongly reduced.

Therefore, the implementation of advanced computational methods based on Kriging metamodels enhance the LOFA precursors identification algorithm, overcoming the limitations given by the huge computational cost associated to the 4C code. In future, additional extension of the database may further improve the proposed algorithm.

From the point of view of the physical analysis of the system and of the LOFA precursors identification, the following results have been obtained. Any single component failure, such us the rotational speed of the CP at 0%, the complete closure of a CVs or the complete opening of the BV, or combinations of at least 3 failures, among the rotational speed of the CP at 75%, the partial closure of a CVs and the partial opening of the BV, cause a LOFA few seconds after the occurred event for the consequent drop of the maximum mass flow rate G_{max} in the CSM until 3600s. There are also sequences of failures that lead to a LOFA at the beginning of the second pulse of current, such us the fall of the CP speed at 50% or 25% preceded by the partial opening of the BV or followed by the partial closure of the CV2 or combined with the complete opening of SV1: in these cases, G_{max} is less than 10% only for a short period, but more than the validation time ($\tau_{val} = 1s$), so the controller C1 detects a LOFA. In addition, there are failures that are not LOFA precursors: the effect of the blocking of a CVs or of the BV at their nominal position is felt by the SMCCC after the LOFA occurrence and not before; the stuck of a SVs has no consequent effect, because the controller C2 has never acted on the SVs in any scenario simulated (i.e., $p_{lim} = 1.8$MPa has never been reached).

Finally, the OSSC method embedding the FCM strategy may be tailored to the analysis of more complex plants, containing a larger number of components and considering more severe operating conditions. Indeed, its deployment may boost the *reliability*, the *availability* and the *maintainability* of the plant, representing the

basis for undertaking the proper *prevention* and *mitigation* strategies in the analysis of plants with a large volume of monitored signals.

APPENDIX A - Spectral Clustering embedding the Fuzzy C-Means

Spectral Clustering (SC) let N objects to be classified in C clusters through the similarity measure w between them (Bellaera et al., 2019; Von Luxburg, 2007). Each similarity is calculated using $N_k = 3$ trajectories, that are $p_{CSM,in}(k = 1)$, $T_{hs}(k = 2)$ and $I/I_{cr}(k = 3)$, of L duration and collected in the similarity matrix $\overline{\overline{W}}[N, N]$ from which the Normalized Laplacian matrix $\overline{\overline{L}}_{sym}$ is computed. Features needed to classify the N object are extracted from $\overline{\overline{L}}_{sym}$ and fed to the Fuzzy C-Means (FCM) code. This algorithm follows different steps (Baraldi et al., 2013):

Step 1: The matrix $\overline{\overline{Y}}^k[N, L]$ is built for each k-th variable considered, collecting at each row all the N transients associated to that variable for the L time length and its generic element is $y_{il}^k(i = 1,2, ..., N; l = 1,2, ..., L)$ referring to the i-th scenario at the l-th time.

Step 2: Each y_{il}^k $(i = 1,2, ..., N; l = 1,2, ..., L)$ is normalized determining $y_{n,il}^k$ as in Eq.(A.1):

$$y_{n,il}^k = 0.2 + 0.6 \cdot \frac{y_{il}^k - min(\overline{\overline{Y}}^k)}{max(\overline{\overline{Y}}^k) - min(\overline{\overline{Y}}^k)}, \qquad k = 1, ..., N_k \qquad (A.1)$$

Step 3: The Euclidean pointwise distance δ_{ij} between an i-th object and a j-th one $(j = 1,2, ..., N)$ is determined as in Eq.(A.2).:

$$\delta_{ij} = \sum_{k=1}^{Z} \sum_{l=1}^{L} \left| y_{n,il}^k - y_{n,jl}^k \right| \qquad (A.2)$$

Step 4: The generic element w_{ij} of the similarity matrix $\overline{\overline{W}}[N, N]$ is obtained from δ_{ij} as follows in Eq.(A.3):

$$w_{ij} = e^{-\left(-\frac{\ln(\alpha)}{\beta} \delta_{ij}^2\right)} = e^{-F \cdot \delta_{ij}^2} \qquad (A.3)$$

Higher "$-\ln(\alpha)/\beta$" is, closer are the N objects and more enhanced the similarity between them (Baraldi et al., 2013) $[F = -\ln(\alpha)/\beta$ is set to $1.7 \cdot 10^{-9}]$. w_{ij} can assume a value between 0 and 1: if it is close to 1, the *i-th* and the *j-th* objects considered are very similar; instead, if it is near to 0, the two objects are very different. Consequently, each element of the matrix $\overline{\overline{W}}$ in the diagonal is equal to 1, because $\delta_{ii} = 0$. This matrix is also symmetrical, because $\delta_{ij} = \delta_{ji}$.

Step 5: Each element $d_i (i = 1, ..., N)$ of the Degree matrix $\overline{\overline{D}}[N, N]$, which is a diagonal matrix, is determined with Eq.(A.4):

$$d_i = \sum_{j=i}^{N} w_{ij} \tag{A.4}$$

Now, it is possible to calculate the Laplacian matrix $\overline{\overline{L}}[N, N]$ by subtracting the Similarity matrix to the Degree matrix: $\overline{\overline{L}} = \overline{\overline{D}} - \overline{\overline{W}}$.

Step 6: The Normalized Laplacian matrix $\overline{\overline{L}}_{sym}[N, N]$ is computed normalizing $\overline{\overline{L}}$ as in Eq.(A.5):

$$\overline{\overline{L}}_{sym} = \overline{\overline{D}}^{-1/2} \overline{\overline{L}} \overline{\overline{D}}^{-1/2} = \overline{\overline{I}} - \overline{\overline{D}}^{-1/2} \overline{\overline{W}} \overline{\overline{D}}^{-1/2} \tag{A.5}$$

Step 7: The C smallest eigenvalues $\lambda_1, \lambda_2, ..., \lambda_C$ and their associated eigenvectors $\vec{u}_1, \vec{u}_2, ..., \vec{u}_C$ of the matrix $\overline{\overline{L}}_{sym}$ are extracted. All the eigenvalues are between 0 and 1 with 0 included and the ones stored are very smaller compared to λ_{C+1}.

Step 8: The matrix $\overline{\overline{U}}[N, C]$ is made associating to each *c-th* column the $\vec{u}_c[N, 1]$ eigenvector obtained by the previous phase. Afterward, this matrix is normalized calculating the matrix $\overline{\overline{T}}[N, C]$, whose generic element t_{ic} is determined as follow in Eq.(A.6):

$$t_{ic} = \frac{u_{ic}}{\sqrt{\sum_{c=1}^{C} u_{ic}^2}}, \quad i = 1, 2, ..., N, \quad c = 1, 2, ..., C \tag{A.6}$$

The eigenspace coordinates of the object *i-th* are contained in each row *i-th* of the matrix $\overline{\overline{T}}$, so $\overline{T}_i = [t_{i1}, t_{i2}, ..., t_{iC}]$ is the vector that contains these coordinates.

Step 9: The matrix $\bar{\bar{T}}$, which contains the features extracted of the N objects, is fed to the FCM code to cluster them in C groups.

At the end of this phase, two matrices are generated (Bezdec, 1981)

- A matrix $\bar{\bar{\mathcal{A}}}[C, C]$ containing in each c-th row the eigenspace coordinates of the centre of the c-th cluster, so $\bar{\mathcal{A}}_c = [\mathcal{A}_{c1}, \mathcal{A}_{c2}, \dots, \mathcal{A}_{cC}]$ is the vector that contains these coordinates.

- A matrix $\bar{\bar{\mathcal{M}}}[C, N]$ whose generic element is the M_{ci} membership degree of the i-th object respect to the c-th cluster: the i-th object belongs to the cluster with the highest membership or with the membership above a certain limit ($M_{lim} = 0.7$).

The FCM code follows different steps:

I. Each M_{ci} is initialized with a random value between 0 and 1 and each column of $\bar{\bar{M}}$ is normalized: the rule $\sum_{c=1}^{C} M_{ci} = 1$ must be satisfied.

II. The matrix $\bar{\bar{M}}$ is used to determine the centres of the C clusters as in Eq.(A.7):

$$\bar{\mathcal{A}}_c = \frac{\sum_{i=1}^{N} M_{ci}^{\rho} \bar{T}_i}{\sum_{i=1}^{N} M_{ci}^{\rho}}, \qquad c = 1, 2, \dots, C \tag{A.7}$$

The parameter ρ is the fuzzy partition exponent (Bezdec, 1981) and it is higher than 1: normally, it is set to 2. In this way, memberships with higher values play a stronger weight in the average procedure in Eq.(15).

III. All the memberships are recalculated as in Eq.(A.8):

$$M_{ci} = \frac{1}{\sum_{\varsigma=1}^{C} \left(\frac{\|\bar{T}_i - \bar{\mathcal{A}}_c\|}{\|\bar{T}_i - \bar{\mathcal{A}}_\varsigma\|} \right)^{\frac{2}{\rho-1}}} \tag{A.8}$$

IV. The objective function J_m is determined and reduced at each iteration as in Eq.(A.9):

$$J_m = \sum_{i=1}^{N} \sum_{c=1}^{C} M_{ci}^{\rho} \|\bar{T}_i - \bar{\mathcal{A}}_c\|^2 \tag{A.9}$$

The minimum improvement between each step is usually set equal to 10^{-5}. If this value is not reached, the algorithm is repeated from *ii* to *iv* until J_m is improved.

Step from *ii* to *iv* are iterated more times in order to minimize the objective function J_m. Normally, 100 iterations are set for this optimization.

APPENDIX B - Supervised Spectral Clustering: Projection in eigenspace

In OSSC is essential to reprocess the *j-th* scenario in $\bar{\bar{T}}_{l,j}[1, C]$ eigenspace coordinates at *l-th* time, because each $\bar{\mathcal{A}}_c[1, C]$ center of the *c-th* cluster, employed to determine each membership $M_{l,cj}(l = 1, \dots, L; c = 1, \dots, C)$ of the *j-th* scenario to the *c-th* cluster at *l-th* time as in Eq.(3.5), is found minimizing the objective function J_m of Eq.(A.9) using eigenspace coordinates $\bar{\bar{T}}_i[1, C](i = 1, \dots, N_{train})$ of $N_{train} = 83$ training scenarios. Therefore, a relation between the $\bar{W}_{l,j}[1, N_{train}]$ similarity vector, containing the similarity between the *j-th* scenario and each *i-th* training scenario, and $\bar{U}_{l,j}[1, C]$, from which $\bar{\bar{T}}_{l,j}[1, C]$ is obtained with Eq.(3.4), must be found, because we cannot proceed like in Appendix A building a Laplacian matrix from $\bar{W}_{l,j}$ in order to discover its eigenvectors and proceed with the analysis.

Anyway, it could be complex finding a this relation between $\bar{W}_{l,j}$ to $\bar{U}_{l,j}$, so it is better to study a law between $\bar{\bar{W}}[N_{train}, N_{train}]$ and $\bar{\bar{U}}[N_{train}, C]$ and adapt it for a single row: in this way the link between $\bar{W}_i$ and $\bar{U}_i$, which are the *i-th* row of $\bar{\bar{W}}$ and $\bar{\bar{U}}$ respectively, is achieved and it could be used for a new scenario.

We start from the relation between a $\lambda_c(c = 1, \dots, C)$ eigenvalue and its associated $\vec{u}_c[N_{train}, 1]$ eigenvector of the normalized Laplacian matrix $\bar{\bar{L}}_{sym}$, which is a squared matrix, expressed in Eq.(B.1):

$$\bar{\bar{L}}_{sym}\vec{u}_c = \lambda_c\vec{u}_c \tag{B.1}$$

This last matrix could be rewritten using Eq.(A.5):

$$\left(\bar{\bar{I}} - \bar{\bar{D}}^{-1/2}\bar{\bar{W}}\,\bar{\bar{D}}^{-1/2}\right)\vec{u}_c = \lambda_c\vec{u}_c \tag{B.2}$$

$\bar{\bar{D}}[N_{train}, N_{train}]$ is a diagonal matrix and each term of the diagonal is calculated from $\bar{\bar{W}}$ using Eq.(A.4), while $\bar{\bar{I}}[N_{train}, N_{train}]$ is an identity matrix.

With some calculation from Eq.(B.2), we find:

$$\vec{u}_c - \bar{\bar{D}}^{-1/2}\bar{\bar{W}}\,\bar{\bar{D}}^{-1/2}\vec{u}_c = \lambda_c\vec{u}_c \tag{B.3}$$

$$(1 - \lambda_c)\vec{u}_c = \overline{\overline{D}}^{-1/2}\overline{\overline{W}}\,\overline{\overline{D}}^{-1/2}\vec{u}_c \tag{B.4}$$

Finally, a relation between $\overline{\overline{W}}$ matrix and a $\vec{u}_c$ eigenvector, which is a column of $\overline{\overline{U}}$, is expressed in Eq.(B.5):

$$\vec{u}_c = \frac{1}{1-\lambda_c}\overline{\overline{D}}^{-1/2}\overline{\overline{W}}\,\vec{P}_c \quad c = 1,2,\dots,C \tag{B.5}$$

$$with \quad \vec{P}_c = \overline{\overline{D}}^{-1/2}\vec{u}_c \tag{B.6}$$

Therefore, it is possible to obtain all the $\overline{\overline{U}}$'s columns from Eq.(B.5) knowing $\overline{\overline{W}}$, $\overline{\overline{D}}$, $\vec{P}_c$ and $\lambda_c (c = 1,\dots,C)$.

Eq.(B.5) could be generalized to find a single element u_{ic} of the matrix $\overline{\overline{U}}$, using a single row $\overline{W}_i$ of the similarity matrix $\overline{\overline{W}}$, as in Eq.(B.7):

$$u_{ic} = \frac{d_i^{-1/2}}{1-\lambda_c}\overline{W}_i\,\vec{P}_c \;, \quad c = 1,2,\dots,C \tag{B.7}$$

In this way, the row $\overline{U}_i$ can be found iterating Eq.(B.7) for all the λ_c eigenvalues and its $\vec{P}_c$ vectors, from Eq.(B.6).

Adapting Eq.(B.7) for $\overline{W}_{l,j}$ similarity vector of new *j-th* scenario at *l-th* time, Eq.(B.8) is obtained:

$$u_{l,jc} = \frac{d_{l,j}^{-1/2}}{1-\lambda_c}\overline{W}_{l,j}\,\vec{P}_c \;, \quad c = 1,2,\dots,C \tag{B.8}$$

$$with \quad d_{l,j} = \sum_{i=1}^{N_{train}} w_{l,ji} \tag{B.9}$$

$\overline{U}_{l,j}$ is calculated, repeating Eq.(B.8) for each λ_c and $\vec{P}_c$ from $c = 1$ to $c = C$.

APPENDIX C – Kriging metamodel

Kriging metamodeling is a stochastic interpolation algorithm which let to predict an output $\hat{Y}^k(\boldsymbol{X}) = \mathcal{MM}^k(\boldsymbol{X})$ from an input $\boldsymbol{X} \in \mathcal{D}_{\mathcal{X}} \subset \mathbb{R}^M$ with M, the number of input elements in $\boldsymbol{X}$, and $\mathcal{D}_{\mathcal{X}}$, the domain of $\boldsymbol{X}$ (Lataniotis et al., 2015; Turati et al., 2017). In Kriging metamodel, residuals are correlated by mean of gaussian process like shown in Eq.(C.1):

$$\mathcal{MM}^k(\boldsymbol{X}) = \boldsymbol{\beta_k}^T \boldsymbol{h}(\boldsymbol{X}) + \sigma_k^2 Z(\boldsymbol{X}, \omega_k) = \mathcal{N}(\boldsymbol{\beta_k}^T \boldsymbol{h}(\boldsymbol{X}); \sigma_k^2 Z(\boldsymbol{X}, \omega_k)) \quad \text{(C.1)}$$

The first term of $\mathcal{MM}^k$ is the mean value (i.e., trend) of the linear regression model and it contains the regression coefficients $\boldsymbol{\beta_k} = [\beta_{k1}, \beta_{k2}, \dots, \beta_{kP}]$ and the basis function $\boldsymbol{h} = [\hbar_1, \hbar_2, \dots, \hbar_P]$ where P is the degree of the truncation of $\boldsymbol{h}(\boldsymbol{X})$. The second term is constituted by the variance of the gaussian process σ_k^2, a constant value, and by the zero mean unit variance $Z(\boldsymbol{X}, \omega_k)$ of the gaussian process that depends on the input $\boldsymbol{X}$ and on the probability space ω_k. The value ω_k relies on the correlation function $\mathcal{R}(\boldsymbol{X}, \boldsymbol{X}'; \boldsymbol{\theta}^k)$, depending on the distance between two input samples $\boldsymbol{X}$ and $\boldsymbol{X}'$ and the hyperparameters $\boldsymbol{\theta}^k$.

Each $\mathcal{MM}^k (k = 1, \dots, N_k)$ meta-model is built with the DOE made by the ensemble of the inputs $\overline{\boldsymbol{X}} = \{\boldsymbol{X}_1, \boldsymbol{X}_2, \dots, \boldsymbol{X}_{N_{krig}}\}$ and the ensemble of the outputs $\boldsymbol{y}^k = \{\mathcal{Y}_1^k, \mathcal{Y}_2^k, \dots, \mathcal{Y}_{N_{krig}}^k\}$ both constituted by N_{krig} elements. Consequently to the assumption of the gaussian process, the *k-th* element output prediction $\hat{Y}^k(\boldsymbol{X}) = \mathcal{MM}^k(\boldsymbol{X})$ for a general $\boldsymbol{X}$ input and all the true model responses $\boldsymbol{y}^k$ of the DOE follows the gaussian distribution in Eq.(C.2):

$$\begin{bmatrix} \hat{Y}^k(\boldsymbol{X}) \\ \boldsymbol{y}^k \end{bmatrix} \sim \mathcal{N}_{N_{krig}+1} \left(\begin{bmatrix} \boldsymbol{\beta_k}^T \boldsymbol{h}(\boldsymbol{X}) \\ \mathcal{H}\boldsymbol{\beta}_k \end{bmatrix}; \sigma_k^2 \begin{bmatrix} 1 & \boldsymbol{r}_k^T(\boldsymbol{X}) \\ \boldsymbol{r}_k(\boldsymbol{X}) & \mathcal{R}^k \end{bmatrix} \right) \quad \text{(C.2)}$$

where:

$\mathcal{H}$ is the information matrix, whose generic term is

$$\mathcal{H}_{ip} = \hbar_p(\boldsymbol{X}_i), \quad i = 1, \dots, N_{krig}; \quad p = 1, \dots, P \quad \text{(C.3)}$$

$\mathcal{R}^k$ is the correlation matrix, whose generic term is

$$\mathcal{R}_{ij}^k = \mathcal{R}\big(\boldsymbol{X}_i, \boldsymbol{X}_j; \boldsymbol{\theta}^k\big), \quad i, j = 1, \dots, N_{krig} \tag{C.4}$$

$\boldsymbol{r}_k(\boldsymbol{X})$ is vector of cross-correlations between the configuration $\boldsymbol{X}$ and each one of the DOE and its generic term is

$$r_{ki}(\boldsymbol{X}) = \mathcal{R}(\boldsymbol{X}, \boldsymbol{X}_i; \boldsymbol{\theta}^k), \quad i = 1, \dots, N_{krig} \tag{C.5}$$

Consequently, the mean Kriging value $\mu_{\hat{Y}^k}$ at the $\boldsymbol{X}$ point and its Kriging variance $\sigma_{\hat{Y}^k}^2$ are estimate with Eq.(C.6) and Eq.(C.7), respectively:

$$\mu_{\hat{Y}^k}(\boldsymbol{X}) = \boldsymbol{h}(\boldsymbol{X})\boldsymbol{\beta}_k + \boldsymbol{r}_k^T(\boldsymbol{X})\mathcal{R}^{k^{-1}}(\boldsymbol{y}^k - \boldsymbol{H}\boldsymbol{\beta}_k) \tag{C.6}$$

$$\sigma_{\hat{Y}^k}^2(\boldsymbol{X}) = \sigma_k^2 \left(1 - \boldsymbol{r}_k^T(\boldsymbol{X})\mathcal{R}^{k^{-1}}\boldsymbol{r}_k(\boldsymbol{X}) + \boldsymbol{u}_k^T(\boldsymbol{X})\left(\boldsymbol{H}^T\mathcal{R}^{k^{-1}}\boldsymbol{H}\right)^{-1}\boldsymbol{u}_k(\boldsymbol{X})\right) \tag{C.7}$$

$$\text{with} \quad \boldsymbol{u}_k(\boldsymbol{X}) = \boldsymbol{H}^T\mathcal{R}^{k^{-1}}\boldsymbol{r}_k(\boldsymbol{X}) - \boldsymbol{h}(\boldsymbol{X}) \tag{C.8}$$

$$\text{and} \quad \boldsymbol{\beta}_k = \left(\boldsymbol{H}^T\mathcal{R}^{k^{-1}}\boldsymbol{H}\right)^{-1}\boldsymbol{H}^T\mathcal{R}^{k^{-1}}\boldsymbol{y}^k \tag{C.9}$$

In order to obtain the $\mathcal{MM}^k$ Kriging meta-model, some steps are necessary:

- Choose the trend basis function $\boldsymbol{h}(\boldsymbol{X})$ to adopt for $\mathcal{MM}^k$;
- Choose an opportune correlation function $\mathcal{R}\big(\boldsymbol{X}_i, \boldsymbol{X}_j; \boldsymbol{\theta}^k\big)$;
- Set the hyperparameters $\boldsymbol{\theta}^k$, necessary for the evaluation of the gaussian variance $\sigma_{\hat{Y}^k}^2$ and of the regression coefficients $\boldsymbol{\beta}_k$, or choose a method to find the optimum $\boldsymbol{\theta}^k$.

REFERENCES

(Al-Dahidi et al., 2018) Al-Dahidi, S., Di Maio, F., Baraldi, P., Zio, E., Seraoui, R., 2018, A framework for reconciliating data clusters from a fleet of nuclear power plants turbines for fault diagnosis, Applied Soft Computing, Volume 69, Pages 213-231, ISSN 1568-4946, https://doi.org/10.1016/j.asoc.2018.04.044

(Alzburtas et al., 2015) Alzbutas, R., Voronov, R., 2015. Reliability and safety analysis for systems of fusion device. Fusion Eng. Des. 94, 31–41. https://doi.org/10.1016/j.fusengdes.2015.03.001

(Baraldi et al., 2015a) Baraldi, P., Di Maio, F., Genini, D., Zio, E., 2015, Comparison of Data-Driven Reconstruction Methods For Fault Detection, in IEEE Transactions on Reliability, vol. 64, no. 3, pp. 852-860, https://doi.org/10.1109/TR.2015.243638

(Baraldi et al., 2015b) Baraldi, P., Di Maio, F., Rigamonti, M., Zio, E., Seraoui, R., 2015, Clustering for unsupervised fault diagnosis in nuclear turbine shut-down transients, Mechanical Systems and Signal Processing, Volumes 58–59, Pages 160-178, ISSN 0888-3270, https://doi.org/10.1016/j.ymssp.2014.12.018

(Baraldi et al., 2013) Baraldi, P., Di Maio, F., Zio, E., 2013, Unsupervised Clustering for Fault Diagnosis in Nuclear Power Plant Components, International Journal of Computational Intelligence Systems, 6, 764-777, https://doi.org/10.1080/18756891.2013.804145

(Bellaera et al., 2018) Bellaera, R., 2018, "Computational Methods for the Integrated Deterministic and Probabilistic Safety Assessment of a Simplified Cooling Circuit for a Tokamak Superconducting Magnet." Rel. Nicola Pedroni, Roberto Bonifetto, Laura Savoldi. Politecnico di Torino, Corso di laurea magistrale in Ingegneria Energetica e Nucleare

(Bellaera et al., 2019) Bellaera, R., Bonifetto, R., Di Maio, F., Pedroni, N., Savoldi, L., Zanino, R., Zio, E., "Integrated Deterministic and Probabilistic Safety Assessment of a Superconducting Magnet Cryogenic Cooling Circuit for Nuclear Fusion Applications", submitted for publication on Reliability Engineering and System Safety

(Bezdec, 1981) Bezdec, J.C., 1981, Pattern Recognition with Fuzzy Objective Function Algorithms, Plenum Press, New York

(Bigot, 2018) Bigot, B., 2018, ITER construction and manufacturing progress toward first plasma, Fusion Engineering and Design, ISSN 0920-3796, https://doi.org/10.1016/j.fusengdes.2018.11.052

(Bottura et al., 2009) Bottura, L., Bordini, B., 2009, $J_C(B, T, \varepsilon)$ Parameterization for the ITER Nb_3Sn Production, in IEEE Transactions on Applied Superconductivity, vol. 19, no. 3, pp. 1521-1524, https://doi.org/10.1109/TASC.2009.2018278

(Cadini et al., 2015) Cadini, F., Gioletta, A., Zio, E., 2015, Improved metamodel-based importance sampling for the performance assessment of radioactive waste repositories, Reliability Engineering & System Safety, Volume 134, Pages 188-197, ISSN 0951-8320, https://doi.org/10.1016/j.ress.2014.10.018

(Crisanti et al., 2017) Crisanti, F., Albanese, R., Granucci, G., Martone, R., Sonato, P., 2017, The Divertor Tokamak Test facility proposal: Physical requirements and reference design, Nuclear Materials and Energy, Volume 12, Pages 1330-1335, ISSN 2352-1791, https://doi.org/10.1016/j.nme.2017.05.008

(D'Amico et al., 2016) D'Amico, G., Reccia, L., Portone, A., Jong, C.T.J., Mitchell, N., 2016. ITER TF Magnet System Analyses in Faulted Conditions. IEEE Trans. Appl. Supercond. 26, 3–7. https://doi.org/10.1109/TASC.2016.2517449

(D'Amico et al., 2018) D'Amico, G., Portone, A., Jong, C.T.J., 2018. An Electromagnetic and Structural Finite Element Model of the ITER Toroidal Field Coils. IEEE Trans. Appl. Supercond. 28, 1–5. https://doi.org/10.1109/TASC.2017.2769485

(Di Maio et al., 2016) Di Maio, F., Vagnoli, M., Zio, E., 2016, Transient identification by clustering based on Integrated Deterministic and Probabilistic Safety Analysis outcomes, Annals of Nuclear Energy, Volume 87, Part 2, Pages 217-227, ISSN 0306-4549, https://doi.org/10.1016/j.anucene.2015.09.007

(EC, 2019) European Commission, 2019, Climate strategies & targets. Taken from https://ec.europa.eu/clima/policies/strategies_en

(EC, 2004) European Commission, 2004, Fusion research : an energy option for Europe's future, Directorate General for Research, from https://fusionforenergy.europa.eu/downloads/mediacorner/publications/reports/fusion_research_english.pdf

(Echard et al., 2011) Echard, B., Gayton, N., Lemaire, M., 2011, AK-MCS: An active learning reliability method combining Kriging and Monte Carlo Simulation, Structural Safety, Volume 33, Issue 2, Pages 145-154, ISSN 0167-4730, https://doi.org/10.1016/j.strusafe.2011.01.002

(Everitt et al., 2013) Everitt, D., Reiersen, W., Martovetsky, N., Hussung, R., Litherland, S., Freudenberg, K., Myatt, L., Hatfield, D., Cole, M., Irick, D.K., Reed, R., Lyraud, C., Libeyre, P., Bessette, D., Jong, C., Mitchell, N., Rodriguez-Mateos, F., Dolgetta, N., 2013. ITER Central Solenoid design, in: 2013 IEEE 25th Symposium on Fusion Engineering (SOFE). IEEE, pp. 1–8. https://doi.org/10.1109/SOFE.2013.6635515

(Fisher, 2017) Fisher, E.P.M., 2017. Control valve handbook, fifth edit. ed. FISHER CONTROLS CO

(Freidberg, 2007) Freidberg, J.P., 2007. Plasma Physics and Fusion Energy. Cambridge University Press, Cambridge. https://doi.org/10.1017/CBO9780511755705

(Froio et al., 2016) Froio, A., Bonifetto, R., Carli, S., Quartararo, A., Savoldi, L., R., Zanino, R., 2016, Design and optimization of Artificial Neural Networks for the modelling of superconducting magnets operation in tokamak fusion reactors, Journal of Computational Physics, Volume 321, Pages 476-491, ISSN 0021-9991, https://doi.org/10.1016/j.jcp.2016.05.028

(Garribba et al., 1985) Garribba, S., Guagnini, E., and Mussio, P., Dec. 1985, Multiple-Valued Logic Trees: Meaning and Prime Implicants, in IEEE Transactions on Reliability, vol. R-34, no. 5, pp. 463-472, https://10.1109/TR.1985.5222234

(Hoa et al., 2012) Hoa, C., Bon-Mardion, M., Bonnay, P., Charvin, P., Cheynel, J.N., Lagier, B., Michel, F., Monteiro, L., Poncet, J.M., Roussel, P., Rousset, B., Vallcorba-Carbonell, R., 2012. Investigations of pulsed heat loads on a forced flow supercritical helium loop - Part A: Experimental set up. Cryogenics (Guildf). 52, 340–348. https://doi.org/10.1016/j.cryogenics.2012.02.004

(IAEA, 2002) IAEA, 2002, ITER Technical Basis, ITER EDA Documentation Series No. 24, IAEA, Vienna

(IEA, 2018a) International Energy Agency (IEA), 2018. Key Electricity Trends 2018, https://www.iea.org/newsroom/news/2019/april/key-electricity-trends-2018.html

(IEA, 2018b) International Energy Agency (IEA), 2018. World Energy Outlook 2018, https://www.iea.org/weo2018/

(Ikeda, 2010) Ikeda, K., 2010. ITER on the road to fusion energy. Nucl. Fusion 50. https://doi.org/10.1088/0029-5515/50/1/014002

(IPCC, 2007) IPCC, 2007. Climate Change 2007 Synthesis Report, Intergovernmental Panel on Climate Change, Core Writing Team IPCC, https://doi.org/10.1256/004316502320517344

(ITER, 2006) ITER_D_22HV5L v2.2, 2006 ITER: Design Description Document: DDD 11 Magnet

(ITER, 2014) ITER_D_K7G8GN v2.1, 2014. Central Interlock System Strategy for ITER Magnet Protection: Machine Protection Functions, January 24, 2014

(ITER, 2018) ITER - the way to new energy [Online]. - November 30, 2018. - http://www.iter.org/

(Koizumi, 2013) Koizumi, N., 2013, Progress of ITER Superconducting Magnet Procurement, Physics Procedia, Volume 45, Pages 225-228, ISSN 1875-3892, https://doi.org/10.1016/j.phpro.2013.05.008

(Lataniotis et al., 2015) Lataniotis, C., Marelli, S., Sudret, B., 2015, UQLAB User Manual – Kriging (Gaussian process modelling). https://doi.org/10.13140/RG.2.1.4827.3120

(Marrel et al., 2014) Marrel, A., Pérot, N., Mottet, C., 2014, Development of a surrogate model and sensitivity analysis for spatio-temporal numerical simulators, Stochastic Environmental Research and Risk Assessment, 29, https://doi.org/10.1007/s00477-014-0927-y.

(Martovetsky et al., 2017) Martovetsky, N., Isono, T., Devred, A., Nabara, Y., Zanino, R., Savoldi, L., Bonifetto, R., Bruzzone, P., Breschi, M., Zani, L., 2017, Characterization of the ITER CS conductor and projection to the ITER CS performance, Fus. Eng. Des., vol. 124, https://doi.org/10.1016/j.fusengdes.2017.06.022

(Mitchell et al., 2008) Mitchell, N., Bessette, D., Gallix, R., Jong, C., Knaster, J., Libeyre, P., Sborchia, C., Simon, F. 2008. The ITER magnet system, IEEE Transactions on Applied Superconductivity, vol. 18, no. 2, pp. 435-440, June 2008. https://doi.org/10.1109/TASC.2008.921232

(Mitchell et al., 2012) Mitchell, N., Devred, A., Libeyre, P., Lim, B., Savary, F.,2012, "The ITER Magnets: Design and Construction Status," in IEEE Transactions on Applied Superconductivity, vol. 22, no. 3, pp. 4200809-4200809, June 2012, Art no. 4200809. https://doi.org/10.1109/TASC.2011.2174560

(Nanty et al., 2017) Nanty, S., Helbert, C., Marrel A., Pérot, N., Prieur, C., 2017, Uncertainty quantification for functional dependent random variables, Computational Statistics, Springer, vol. 32(2), pages 559-583, June. https://doi.org/10.1007/s00180-016-0676-0

(OECD, 2012) OECD , 2012, The Role of Nuclear Energy in a Low-carbon Energy Future, Nuclear Development, OECD Publishing, Paris, https://doi.org/10.1787/9789264991897-en

(Savoldi et al., 2000a) Savoldi, L., Zanino, R., 2000. M & M: Multi-conductor Mithrandir code for the simulation of thermal-hydraulic transients in superconducting magnets. Cryogenics (Guildf). 40, 179–189. https://doi.org/10.1016/S0011-2275(00)00027-8

(Savoldi et al., 2000b) Savoldi, L., Zanino, R., 2000. Thermal-hydraulic analysis of Tcs measurement in conductor 1A of the ITER Central Solenoid Model Coil using the M&M code. Cryogenics (Guildf). 40, 593–604. https://doi.org/https://doi.org/10.1016/S0011-2275(01)00017-0

(Savoldi et al., 2010) Savoldi, L., R., Casella, F., Fiori, B., Zanino, R. 2010. The 4C Code for the Cryogenic Circuit Conductor and Coil modelling in ITER, Volume 50, Issue 3, Pages 167-176, ISSN 0011-2275, https://doi.org/10.1016/j.cryogenics.2009.07.008

(Savoldi et al., 2012) Savoldi R., L., Bessette, D., Bonifetto, R., Zanino, R., 2012. Parametric analysis of the ITER TF fast discharge using the 4C code, IEEE Transactions on Applied Superconductivity, vol. 22, no. 3, pp. 4704104-4704104, June 2012, Art no. 4704104, https://doi.org/10.1109/TASC.2012.2188130

(Savoldi et al., 2014) Savoldi, L., Bonifetto, R., Carli, S., Froio, A., Foussat, A., Zanino, R., 2014, Artificial Neural Network (ANN) modelling of the pulsed heat load during ITER CS magnet operation, Cryogenics, Volume 63, Pages 231-240, ISSN 0011-2275, https://doi.org/10.1016/j.cryogenics.2014.03.003

(Savoldi et al., 2018) Savoldi, L., Bonifetto, R., Pedroni, N., Zanino, R. 2018. Analysis of a protected Loss Of Flow Accident (LOFA) in the ITER TF coil cooling circuit. in IEEE Transactions on Applied Superconductivity, vol. 28, no. 3, pp. 1-9, April 2018, Art no. 4202009, https://doi.org/10.1109/TASC.2017.2786688

(Schöbi et al., 2017) Schöbi, R., Sudret, B., Marelli, S., 2017, Rare Event Estimation Using Polynomial-Chaos Kriging, Journal Article, ASCE-ASME Journal of Risk and Uncertainty in Engineering Systems, Part A:

Civil Engineering 2017-06-01 3(2): D4016002, https://doi.org/10.1061/AJRUA6.0000870

(Simpson et al., 2001) Simpson, TW, Peplinski, JD, Koch, PN & Allen, JK 2001, Metamodels for computer-based engineering design: Survey and recommendations, Engineering with Computers, vol. 17, no. 2, pp. 129-150. https://doi.org/10.1007/PL00007198

(Takahashi et al., 2006) Takahashi, Y., Yoshida, K., Nabara, Y., Edaya, M. and Mitchell, N., June 2006, "Simulation of Quench Tests of the Central Solenoid Insert Coil in the ITER Central Solenoid Model Coil," in IEEE Transactions on Applied Superconductivity, vol. 16, no. 2, pp. 783-786. https://doi.org/10.1109/TASC.2006.873254

(Taylor et al., 2017) Taylor, N., Ciattaglia, S., Boyer, H., Coombs, D., Jin, X.Z., Liger, K., Mora, J.C., Mazzini, G., Pinna, T., Urbonavičius, E., 2017. Resolving safety issues for a demonstration fusion power plant. Fusion Eng. Des. 124, 1177–1180. https://doi.org/10.1016/j.fusengdes.2017.02.018

(Taylor et al., 2014) Taylor, N., Cortes, P., 2014. Lessons learnt from ITER safety & licensing for DEMO and future nuclear fusion facilities. Fusion Eng. Des. 89, 1995–2000. https://doi.org/10.1016/j.fusengdes.2013.12.030

(Taylor, 2016) Taylor, N. P., 2016. Safety and licensing of nuclear facilities for fusion. Proc. - Symp. Fusion Eng. 2016–May. https://doi.org/10.1109/SOFE.2015.7482293

(Turati et al., 2017) Turati, P., Pedroni, N., Zio, E., 2017, Simulation-based exploration of high-dimensional system models for identifying unexpected events. pp.317-330. In RELIABILITY ENGINEERING & SYSTEM SAFETY - ISSN:0951-8320 vol. 165 https://doi.org/10.1016/j.ress.2017.04.004

(Turati et al., 2018) Turati, P., Cammi, A., Lorenzi, S., Pedroni, N., Zio, E., 2018, Adaptive simulation for failure identification in the Advanced Lead Fast Reactor European Demonstrator, Progress in Nuclear Energy, vol. 103 , pp. 176-190, ISSN: 0149-1970, https://doi.org/10.1016/j.pnucene.2017.11.013

(Von Luxburg, 2007) Von Luxburg, U., 2007, A tutorial on spectral clustering, Stat. Comput. 17, 395–416. https://doi.org/10.1007/s11222-007-9033-z

(Wall et al., 2003) Wall M.E., Rechsteiner A., Rocha L.M., 2003, Singular Value Decomposition and Principal Component Analysis. In: Berrar D.P., Dubitzky W., Granzow M. (eds) A Practical Approach to Microarray Data Analysis. Springer, Boston, MA https://doi.org/10.1007/0-306-47815-3_5

(Wang et al., 2007) Wang, Gary & Shan, S. ,2007, Review of Metamodeling Techniques in Support of Engineering Design Optimization. Journal of Mechanical Design - J MECH DESIGN. 129. https://doi.org/10.1115/1.2429697

(Wang et al., 2018) Wang, Z., Pedroni, N., Zentner, I., Zio, E., 2018, Seismic fragility analysis with artificial neural networks: Application to nuclear power plant equipment, Engineering Structures, Volume 162, Pages 213-225, ISSN 0141-0296, https://doi.org/10.1016/j.engstruct.2018.02.024

(Wu et al., 2016) Wu, Y., Chen, Z., Hu, L., Jin, M., Li, Y., Jiang, J., Yu, J., Alejaldre, C., Stevens, E., Kim, K., Maisonnier, D., Kalashnikov, A., Tobita, K., Jackson, D., Perrault, D., 2016. Identification of safety gaps for fusion demonstration reactors. Nat. Energy 1, https://doi.org/10.1038/nenergy.2016.154

(Zanino et al., 1995) Zanino, R., De Palo, S., Bottura, L., Savoldi, L., Zanino, R., 1995. A two-fluid code for the thermohydraulic transient analysis of CICC superconducting magnets. J. Fusion Energy 14, 25–40. https://doi.org/10.1007/BF02214031

(Zanino et al., 2010) Zanino, R., Bessette, D., Savoldi, L., R., 2010, Quench analysis of an ITER TF coil, Fusion Engineering and Design, Volume 85, Issue 5, Pages 752-760, ISSN 0920-3796, https://doi.org/10.1016/j.fusengdes.2010.04.056

(Zanino et al., 2011) Zanino, R., Bonifetto, R., Heller, R., Savoldi Richard, L., 2011. Validation of the 4C thermal-hydraulic code against 25 kA safety discharge in the ITER Toroidal Field Model Coil (TFMC). IEEE Trans. Appl. Supercond. 21, 1948–1952. https://doi.org/10.1109/TASC.2010.2089771

(Zanino et al., 2012) Zanino, R., Bonifetto, R., Savoldi Richard, L., Casella, F., 2012. Dynamic modeling of a supercritical helium closed loop with the 4C code, in: AIP Conference Proceedings. pp. 1743–1750. https://doi.org/10.1063/1.4707109

(Zanino et al., 2013) Zanino, R., Bonifetto, R., Casella, F., Savoldi Richard, L., 2013. Validation of the 4C code against data from the HELIOS loop at CEA Grenoble. Cryogenics (Guildf). 53, 25–30. https://doi.org/10.1016/j.cryogenics.2012.04.01072